Dissertation zur Erlangung des Doktorgrades
der Fakultät für Chemie und Pharmazie
der Ludwig-Maximilians-Universität München

Structural studies of the human Ccr4-Not complex

Jana Celine Albrecht

aus

München

2022

Erklärung

Diese Dissertation wurde im Sinne von §7 der Promotionsordnung vom 28. November 2011 von Prof. Dr. Elena Conti betreut.

Eidesstattliche Versicherung

Diese Dissertation wurde eigenständig und ohne unerlaubte Hilfe erarbeitet.

München, 17.05.2022

_____

Jana Albrecht

Dissertation eingereicht am:	19.05.2022
1. Gutachterin/Gutachter:	Prof. Dr. Elena Conti
2. Gutachterin/Gutachter:	Prof. Dr. Karl-Peter Hopfner
Mündliche Prüfung am:	27.06.2022

Contents

List of Figures

List of Tables

Summary

mRNA decay is an important post-transcriptional mechanism to regulate eukaryotic gene expression. Deadenylation of the 3'-terminal poly(A) tail is the first and rate-limiting step in canonical mRNA decay, which is carried out by two multiprotein complexes, the Pan2-Pan3 and Ccr4-Not deadenylases. Pan2-Pan3 acts in a distributive manner preferentially on long poly(A) tails covered with multiple PABPC molecules, whereas the Ccr4-Not complex removes the poly(A) closer to the 3'UTR.

Ccr4-Not is a conserved protein complex consisting of eight constitutive subunits that dock modularly to a large scaffold protein, CNOT1. It comprises two enzymatically active subunits, the 3'exonucleases CNOT6 (yeast Ccr4) and CNOT7 (yeast Caf1). The non-enzymatic modules of the complex act as structural support or provide binding sites for protein-protein interactions with adapter proteins that recruit the complex to target mRNAs. One of those adapter proteins is RNA-binding protein Tristetraprolin (TTP), which recruits Ccr4-Not specifically to mRNAs containing AU-rich elements (AREs).

Although the architecture of Ccr4-Not has been intensively studied, high-resolution structures are only available for individual subcomplexes. This is due to the size and flexibility of the complex. In the presented work, a method for recombinant expression and purification of the full-length human Ccr4-Not complex was established. The aim of this thesis was to solve the structure of the human Ccr4-Not complex. However, flexibility and structural heterogeneity hampered the solution of a high-resolution structure of the complex by cryo-electron microscopy. A 3D reconstruction of the entire complex achieved only medium

resolution. Available atomic models of the individual modules were positioned in the density based on cross-linking mass-spectrometry data to interpret the 3D reconstruction and provide a first indication to the global architecture of the complex.

The heterologously expressed and purified complex was also characterized biochemically *in vitro* in deadenylation experiments. The intact Ccr4-Not complex was more active and selective for the end of the poly(A) tail at the junction with the 3'UTR than a tetrameric core complex, comprising the central part of CNOT1, the two nucleases CNOT6, CNOT7 and CNOT9, lacking the N-terminal and C-terminal modules. In the presence of ARE-binding protein TTP, the deadenylation reaction of an ARE-containing RNA substrate was accelerated.

Chapter 1

Introduction

1.1 mRNA dynamics and degradation

Cells must constantly respond to external stimuli or changing growth conditions, while maintaining homeostasis, conserving energy, and coping with spatial constraints. The regulation of gene expression to increase or decrease gene products (protein or RNA) is therefore vital for the survival of single cells and for multicellular organisms during developmental stages. It encompasses a wide range of mechanisms that can modulate any step from DNA to protein or RNA.

One important mechanism controlling gene expression is messenger RNA (mRNA) turnover. Cytoplasmic mRNA levels are highly dynamic and controlled by rates of mRNA synthesis, processing, transport, and decay. After RNA processing and export to cytoplasm, mRNAs are either translated, stored in P-bodies for later translation or degraded (Shyu *et al.*, 2008). Half-lives of mRNAs vary widely from a few minutes to longer than the cell-specific doubling time, such as 1-2 min to 15 min in *Escherichia coli* (*E. coli*) to 90 min in yeast and up to several weeks in metazoans (Coburn & Mackie, 1998; Herrick *et al.*, 1990; Brower *et al.*, 1981). The decay of mRNAs involves on the one hand, effective quality control mechanisms to degrade aberrant or truncated mRNAs preventing the production of potentially toxic proteins and, on the other hand, the regulation of mRNA half-lives to alter the abundance

of functional proteins (reviewed in Schoenberg & Maquat, 2012). Overexpression of growth factors, inflammatory mediators and proto-oncogenes due to missing post-transcriptional regulation can lead to diseases such as cancer and chronic inflammation (Benjamin & Moroni, 2007; López de Silanes *et al.*, 2007; Sanduja *et al.*, 2012; Schoenberg & Maquat, 2012).

1.1.1 mRNA degradation

Mature eukaryotic mRNAs consist of a coding sequence flanked by 5'- and 3'-untranslated regions (UTRs) and are modified at their 5'-end with a 7-methylguanosine (m^7G) cap structure and at their 3' end with polyadenosine (poly(A)) tails (with the exception of histone mRNAs). Both modifications are added during co-transcriptional processing of the precursor mRNA (pre-mRNA) before transcription is terminated and the mRNA is exported to the cytoplasm. The m^7G cap is attached via a 5'-5' triphosphate linkage through the capping complex, which is recruited by phosphorylation of the C-terminal domain (CTD) of RNA polymerase II (Reddy *et al.*, 1974; Shatkin, 1976). It contributes to mRNA stability, nuclear export, and translation initiation (reviewed in Cowling, 2010). The poly(A) tail is attached to the 3' end of the mRNA by the 3' end processing machinery in the final step of pre-mRNA processing, which is described in more detail in 1.2.1. In eukaryotes, poly(A) tails provide mRNA stability and regulate many aspects of the mRNA life cycle: export, translation, and turnover (Bernstein *et al.*, 1989; Kapp & Lorsch, 2004; Fuke & Ohno, 2008).

General mRNA decay

Deadenylation Shortening of the poly(A) tail is the first and often rate-limiting step of decay for most mRNAs (Decker & Parker, 1993; Garneau *et al.*, 2007; Eisen *et al.*, 2020; Meyer *et al.*, 2004). The classical model of deadenylation is a biphasic process in which two different multiprotein complexes, the poly(A)-specific nuclease (Pan) Pan2-Pan3 and carbon catabolite repression 4 (Ccr4) - negative on TATA-less (Not) complex, sequentially shorten the poly(A) tail (Yamashita *et al.*, 2005). A third nuclease specific to poly(A) tails, Poly(A) specific ribonuclease (PARN), has been discovered (Körner & Wahle, 1997), but it is not widely conserved (absent in yeast and *Drosophila melanogaster* (*D. melanogaster*)) and does not participate in general mRNA turnover but in *Xenopus* oocytes (Copeland & Wormington, 2001; Yamashita *et al.*, 2005).

Pan2-Pan3, a heterotrimeric complex, consisting of the DEDD 3'-exonuclease Pan2 and an asymmetric dimer of Pan3, shortens the 3'-terminal end of the poly(A) tail in a distributive manner (in yeast to 50-70 nucleotides (nt), in mammals to 110 nt) (Boeck *et al.*, 1996; Jonas *et al.*, 2014; Schäfer *et al.*, 2014) stimulated by interaction with the poly(A) binding protein (PABPC) (Boeck *et al.*, 1996; Uchida *et al.*, 2004). Pan2-Pan3 recognizes the oligomerization surfaces of multiple PABPC molecules, which explains its preference for longer poly(A) ribonucleoprotein particles (RNPs). As the poly(A) tail is shortened and consequently PABPC molecules are removed, the affinity for Pan2-Pan3 binding decreases (Schäfer *et al.*, 2019). Then the Ccr4-Not complex adopts and trims the remaining poly(A) tail to ∼10 nt in a processive manner (reviewed in Chen & Shyu, 2011; Passmore & Coller, 2021) (see 1.1). The Ccr4-Not complex will be described in detail in the last section of the introduction (1.3). Deadenylation is to some extent a reversible process, as deadenylated mRNAs can be stored and re-adenylated by mainly non-canonical cytoplasmic poly(A) polymerases such as GLD-2-like enzymes, thereby re-entering the translation pool. This mechanism occurs mainly in early development (Zhang *et al.*, 2010; Richter,

1999; Subtelny *et al.*, 2014; Eckmann *et al.*, 2011).

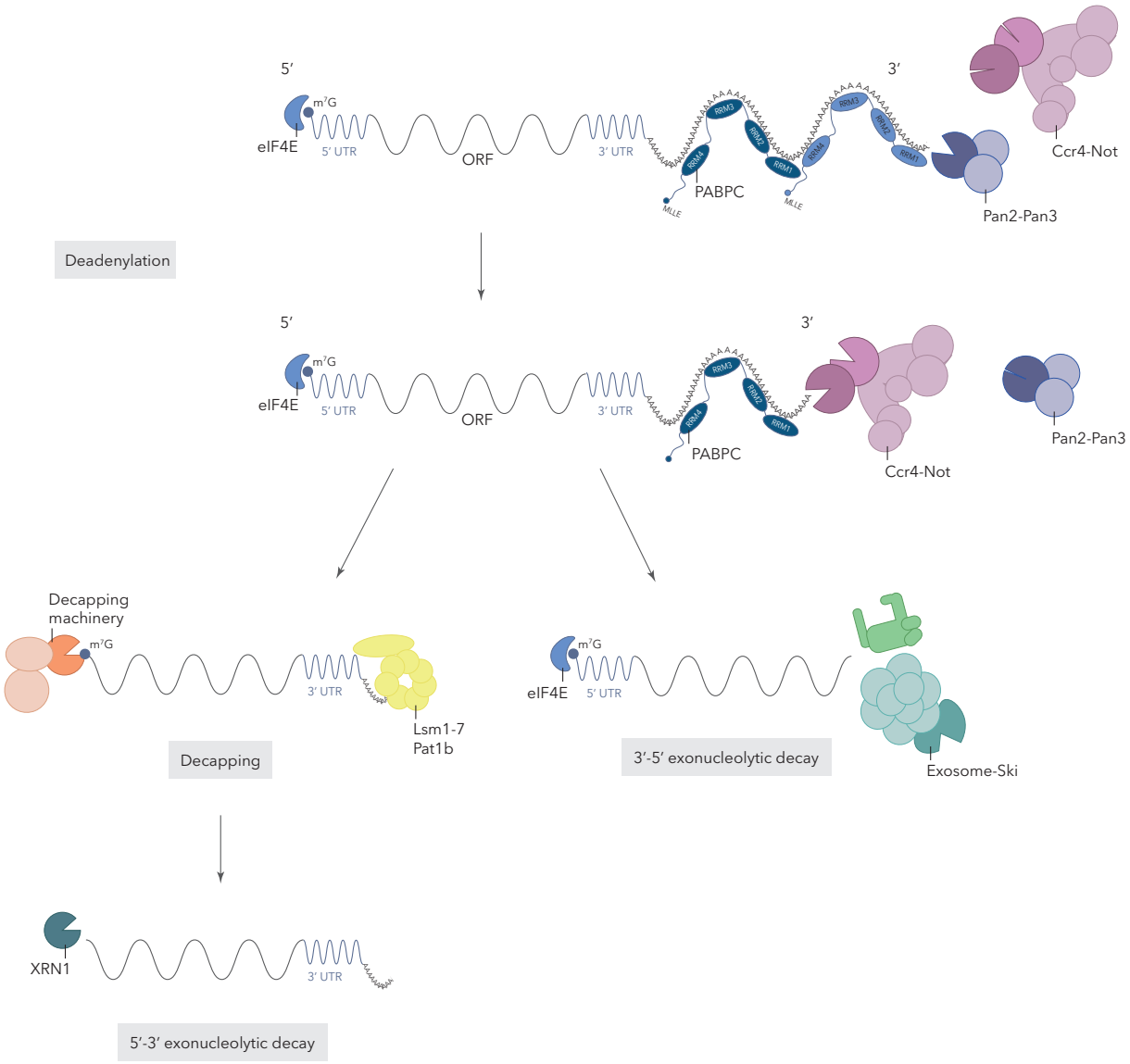

Figure 1.1. Overview of canonical mRNA degradation. During the first step of canonical mRNA degradation, the 3' poly(A) tail is shortened by the deadenylase complex Pan2-Pan3. Subsequently, the tail is further trimmed by the Ccr4-Not deadenylase complex. After deadenylation, the complex is either decapped and then degraded 5' to 3' by exonuclease XRN1 or in 3' to 5' direction by exosome-ski. Dark colors indicate enzymatically active subunits, figure adapted from (Passmore & Coller, 2021).

5' to 3' decay pathway After erosion of the poly(A) tail by deadenylases, the shortened poly(A) tails can be bound by Lsm1-7/Pat1L1 to stimulate decapping (Tharun *et al.*, 2000;

Ozgur *et al.*, 2010). Removal of the 5' m^7G cap structure is irreversible and results in 5' to 3' degradation (reviewed in Parker & Sheth, 2007; Garneau *et al.*, 2007). The strict order of deadenylation prior to decapping protects functional, polyadenylated mRNAs from degradation. While yeast has only one decapping enzyme DCP2, mammals possess multiple decapping enzymes in addition to DCP2, also from the Nudix family, each acting on a subset of transcripts (reviewed in Grudzien-Nogalska & Kiledjian, 2017). The best-studied decapping complex consists of the decapping enzyme DCP2, which is stimulated by DCP1, and interacting factors such as enhancers of decapping (EDCs), the Lsm1-7/PatL1 complex, and RNA-helicase DDX6 (Dhh1) (reviewed in Jonas & Izaurralde, 2015). The different composition of the decapping machinery leads to different mRNA substrate specificities (He *et al.*, 2018). Decapping produces a 5' monophosphorylated mRNA, that is specifically recognized by the 5'-3' exoribonuclease XRN1 (Jones *et al.*, 2012). XRN1 is the major cytoplasmic 5'-3' exonuclease in eukaryotes (reviewed in Geisler & Coller, 2012). It is also responsible for degradation of RNAs generated by endonucleolytic cleavage in RNA surveillance pathways such as Nonsense-meditated decay (NMD), No-go decay (NGD), or siRNA-mediated gene silencing (Kim & Maquat, 2019; Huntzinger *et al.*, 2008; Orban & Izaurralde, 2005). It interacts with many factors of the decapping machinery and also directly with Ccr4-Not, thereby inhibiting its deadenylation activity (Ozgur *et al.*, 2010; Chang *et al.*, 2019).

3' to 5' decay pathway The unprotected 3' end generated by deadenylation is then further degraded 3' to 5' by the exosome, a conserved multiprotein complex (Mitchell *et al.*, 1997). The exosome consists of a 9-subunit, catalytically inactive barrel-like core (Exo9) that associates with co-factors depending on the cellular context. The RNA-substrate is unwounded and fed into the core by helicases, in the cytoplasm the SKI complex with helicase SKI2, in the nucleus the TRAMP complex (TRF-AIR-MTR4) bearing helicase

MTR4 (Houseley & Tollervey, 2009). Two nucleases, DEDD-type exonuclease RRP6 (nuclear) and RNAse R/II-like Rrp44/DIS3 (mostly nuclear) or DIS3L(cytoplasmic), associate with the Exo9-complex to form the catalytically active Exo10, or Exo11, which hydrolyzes the substrate (reviewed in Makino *et al.*, 2013). In addition to mRNA decay, the exosome is involved in RNA surveillance and processing of coding and non-coding RNAs (reviewed in Chlebowski *et al.*, 2013. The 3' to 5' degradation is followed by dissolution of the cap by the scavenger decapping enzyme DcpS (reviewed in Siwaszek *et al.*, 2014).

miRNA mediated decay

MicroRNAs (miRNAs), first discovered in *Caenorhabditis elegans* (*C. elegans*) (Lee *et al.*, 1993), are short (∼22 nt), endogenous, single-stranded, non-coding RNAs participating in post-transcriptional gene silencing, that is conserved in animals and plants but absent in fungi (reviewed in Jonas & Izaurralde, 2015). In most cases, they bind to Argonaute proteins (AGOs) to form miRNA-induced silencing complexes (miRISCs) and interact with miRNA response elements (MREs) in 3'UTRs of mRNAs containing partially or fully complementary sequences to induce translational repression and/or mRNA decay (reviewed in Huntzinger & Izaurralde, 2011). In rare cases of a fully complementary interaction, mRNAs can be cleaved endonucleolytically by some AGO proteins such as AGO2, which contains an RNse H-like PIWI domain. However, in animals, miRNAs are rarely fully complementary, so AGO proteins mediate the regulation of gene expression mainly independently of endonucleolytic cleavage (reviewed in Ameres & Zamore, 2013).

GW182 proteins discovered in *D. melanogaster* RNAi screens, function as downstream effectors of AGOs in RNA silencing (Fabian & Sonenberg, 2012). The GW182 protein in flies has three vertebrate paralogs (TNRC6A, TNRC6B, and TNRC6C), whereas plants have no paralogues of GW182. Therefore, endonucleolytic cleavage by AGOs is predominant in plants.

GW182 proteins bind AGOs with multiple glycine-tryptophan repeats (GW-repeats) within their N-terminal AGO domain and can recruit the deadenylation complexes Pan2-Pan3 (Schirle & MacRae, 2012; Christie *et al.*, 2013) or Ccr4-Not (Chen *et al.*, 2014; Mathys *et al.*, 2014) with W-containing motifs in their C-terminal silencing domain. In addition, GW182 with its PAM2 motif can bind the MLLE domain of PABPC (Braun *et al.*, 2013). After miRNA induced deadenylation, the mRNAs are decapped by DCP2 and cofactors and finally degraded 5' to 3' by exonuclease XRN1.

Aberrant mRNA degradation

Exceptions to the canonical mRNA decay pathway are quality control pathways such as NMD, NGD or non-stop decay (NSD). These co-translational quality control mechanisms ensure that transcripts with premature stop codons (PTCs), transcripts with non-optimal codons leading to ribosome stalling, or transcripts without stop codons are rapidly removed. In the case of NMD, one of the best characterized pathways, depending on the presence of an exon junction complex (EJC), transcripts are either endonucleolytically cleaved by SMG6 or exonucleolytically degraded 5' to 3' by XRN1 and/or 3' to 5' by the exosome or DIS3L2 mediated by SMG5-SMG7, recruiting Ccr4-Not and the decapping machinery (Kurosaki *et al.*, 2019; Wolin & Maquat, 2019). The mechanisms differ from yeast to mammals (reviewed in Siwaszek *et al.*, 2014; Schoenberg & Maquat, 2012.

1.2 Regulation of mRNA turnover by poly(A) tails

1.2.1 Poly(A) tails

Poly(A) tails, with an average length of ∼70 nt in yeast (McLaughlin *et al.*, 1973) and up to 250 nt in mammals (Edmonds *et al.*, 1971), are present at the 3' end of almost

all eukaryotic mRNAs, with the exception of histone mRNAs of metazoans (Dominski & Marzluff, 1999). They were first described in the 1970s (Edmonds *et al.*, 1971; Darnell *et al.*, 1971; Lee *et al.*, 1971) and are coated with poly(A)-binding proteins. The poly(A) tail and poly(A) binding protein together form RNPs. Shorter oligo(A) tails can also be temporarily attached to different types of RNA, as part of a quality control mechanism with destabilizing effects (reviewed in (Eckmann *et al.*, 2011)). In prokaryotes, poly(A) tails are less present and more likely to be involved in degradation, such as in *E. coli* (Dreyfus & Régnier, 2002).

Poly(A) tails are added to the mRNA 3' end in the final step of co-transcriptional mRNA processing by the 3'end processing machinery before transcription is terminated and the mRNA exported to the cytoplasm. The core 3' end processing machinery is a megadalton complex composed of four conserved protein complexes: cleavage and polyadenylation specificity factor (CPSF), cleavage factors I and II (CFI, CFII), the cleavage stimulation factor (CstF), and the canonical poly(A) polymerase (PAP) (reviewed in Xiang *et al.*, 2014).

Processing of the 3' end, initiated by recognition of specific sequence elements in the pre-mRNA, consists of endonucleolytic cleavage followed by polyadenylation of the 5' fragment, and degradation of the downstream fragment. After cleavage, polyadenylation by PAP occurs biphasically: the addition of the first nucleotides occurs slowly until it reaches a length of ∼11 nt that can bind the nuclear poly(A) binding protein PABPN. After binding of PABPN, the polyadenylation growth rate increases significantly (Wahle, 1991; Kühn *et al.*, 2017). Polyadenylation stops when the tail reaches ∼200-250 nt (Sheiness & Darnell, 1973), assuming that PABPN serves as a molecular ruler (Keller *et al.*, 2000). However, the exact mechanism of length control is not yet clear.

The canonical poly(A) signal (PAS) (usually AAUAAA) as well as auxiliary signals such as a downstream GU (or U)-rich region define the position of the poly(A) tail (Wahle

& Rüegsegger, 1999; Shi & Manley, 2015). Alternative polyadenylation sites are present in most human genes and responsible for the expression of isoforms, that differ in their 3'UTR. Which PAS is used depends on the expression and interaction of context-dependent regulators (reviewed in Gruber & Zavolan, 2019).

3' end processing contributes to termination of transcription and nuclear export of the mRNA (Eaton *et al.*, 2020). In the cytoplasm, displacement of PABPN by the poly(A)-binding protein PABPC occurs, but the mechanism is not well understood. The length of poly(A) tails is very dynamic – once added to a defined length, the tail is gradually shortened throughout the mRNA lifetime (Sheiness & Darnell, 1973). Recent evidence suggests that poly(A) tails are already shortened in the nucleus (Alles *et al.*, 2021), which continues after export of the mRNA to the cytoplasm and eventually leads to decapping and degradation. Therefore, the steady-state length of bulk poly(A) is heterogenous (reviewed in Eckmann *et al.*, 2011; Chen & Shyu, 2011). The role of poly(A) tails in regulation of mRNA turnover will be discussed below (1.2.4).

The poly(A) binding protein

To date, two types of poly(A)-binding proteins have been described that are involved in processes surrounding the poly(A) tail: the predominantly nuclear (PABPN), involved in the polyadenylation process (described in more detail above 1.2.1) and the predominantly cytoplasmic (PABPC), involved in translation and mRNA decay. PABPC was first described shortly after the discovery of poly(A) tails: as a protein tightly bound to the 3' end of cytoplasmic eukaryotic mRNAs (Blobel, 1973). Its footprint was detected by nuclease digestion of ^{32}P-labeled Mouse Friend erythroleukemic cell cytoplasm, which showed a periodic pattern of multiples of 27 nucleotides specific to poly(A) (Baer & Kornberg, 1980, 1983).

PABPC is highly conserved among eukaryotes, with one isoform in yeast (Pab1) and sev-

eral isoforms such as PABPC1, inducible PABPC4, embryonic ePABP, and testes-specific tPABP in mammals (reviewed in Smith *et al.*, 2014). The mammalian PABPC1 is probably the most abundant and best-studied. It consists N-terminally of four RNA-recognition motifs (RRMs) linked to a C-terminal mademoiselle domain (MLLE) via a proline- and glutamine-rich linker region. This >100 amino acid long linker region is the least conserved part of the protein.

The RRMs bind poly(A) tails with binding affinities in the low nanomolar range (Pab1: 5 nM (Sachs *et al.*, 1987), PABPC1: 7 nM (Görlach *et al.*, 1994)). Interestingly, the individual RRMs are more similar to the corresponding RRMs in other species than to each other, suggesting different functions. Indeed, RRM1 and RRM2 were shown to have the strongest binding affinity and specificity for poly(A) over poly(U) and poly(G), whereas RRM3 and RRM4 have lower RNA-binding affinity and are less sequence specific (Burd *et al.*, 1991). The minimum length of a poly(A) tail required for PABPC1 binding is ∼12 nt, but the footprint of total PABPC1 is ∼27 nt (Baer & Kornberg, 1983).

The linker region is important for cooperative binding and oligomerization of PABPC in the presence of poly(A) (Simón & Séraphin, 2007; Melo *et al.*, 2003). Oligomerization results in the poly(A) tail adopting a periodic 'zigzag' shape. The oligomerization interfaces are recognized by the Pan2-Pan3 deadenylase, as shown by a cryo-EM structure of a 90A poly(A)-mRNP harboring three Pab1 molecules in complex with yeast Pan2-Pan3 (Schäfer *et al.*, 2019).

The MLLE domain interacts with poly(A)-interacting motif 2 (PAM2), a short sequence motif found in several proteins involved in translation termination and mRNA decay processes, such as eukaryotic release factor 3 (eRF3), Pan3, PABP-interacting protein 2 (Paip2), and GW182 proteins (reviewed in (Xie *et al.*, 2014)).

PAPBC1 was linked to translation, as, RRM2, in addition to RNA binding has been shown to interact with translation initiation factor eIF4G (Kessler & Sachs, 1998; Imataka *et al.*,

1998). The role of PABPC1 is ambivalent, between stabilizing the 3' end by protecting the poly(A) tail from nonspecific degradation (Ford *et al.*, 1997) and, on the other hand, promoting mRNA degradation (Sachs & Davis, 1989) by interaction with Pan2-Pan3 and Ccr4-Not deadenylase complexes (Webster *et al.*, 2018; Uchida *et al.*, 2004).

1.2.2 Genome-wide profiling of poly(A) tails

To obtain information on the genome-wide relationship between poly(A) tail length, translational efficiency and mRNA half-life, the precise length and composition of poly(A) tails and the corresponding mRNA isoforms must be determined. However, the study of poly(A) tails has been be very difficult due to technical shortcomings. Until very recently, common sequencing technologies could not reliably decipher long homopolymeric sequences, or detect modifications at the 3' end. Additionally, mRNAs constitute only a small fraction of cellular RNA, so rRNAs and tRNAs were dominating the cDNA libraries (Chang *et al.*, 2014). Because the number of genes studied was limited, global interpretations could not be made (reviewed in Passmore & Coller, 2021).

Recently, several techniques for genome-wide profiling of poly(A) tails have been presented that overcome some of the above mentioned challenges. Among these are TAIL-seq (Chang *et al.*, 2014; Lim *et al.*, 2016), which allows detection of non-A nucleotides at the 3' end but is limited to a total of 230 nt, whereas poly(A) tail length profiling by sequencing (PAL-seq) (Subtelny *et al.*, 2014) allows accurate estimation of a broad range of poly(A) tail lengths and the respective cleavage and polyadenylation sites. TAIL-seq and PAL-seq provide deep coverage but cannot sequence the entire tail and provide only a short read of the respective mRNA whereas, full-length poly(A) and mRNA sequencing (FLAM-seq) involves sequencing of transcription start site, splice pattern, 3' end, and poly(A) tail for each mRNA by using PacBio Sequel (Legnini *et al.*, 2019).

1.2.3 Poly(A) tails and translational efficiency

Early studies indicated that poly(A) tail length correlates with stability and translation efficiency, leading to the adoption of this as a general concept (reviewed in Eckmann *et al.*, 2011; Weill *et al.*, 2012. However, many of these studies were performed in oocytes and early embryos. Recent genome-wide analyses, using novel sequencing methods (1.2.2), have added a new layer of complexity by demonstrating a nonlinear relationship between poly(A) tail length, translational efficiency and mRNA stability (reviewed in Passmore & Coller, 2021).

Coupling of poly(A) tail length and translational efficiency was found only at developmental stages, confirming earlier results for single genes but not appearing to be the case in many postembryonic cells (Subtelny *et al.*, 2014; Park *et al.*, 2016; Eichhorn *et al.*, 2016). A recent study in *Xenopus* oocytes and postembryonic mammalian cells revealed that a limited amount of PABPC1 (among other criteria) is required for the coupling of poly(A) tail length and rate of translation in oocytes (Xiang & Bartel, 2021). At early developmental stages, there is no de novo transcription and degradation factors are present at low levels, so regulation of gene expression is mediated by poly(A)-tail length of mRNAs, which in this case correlates with translational efficiency (reviewed in Barckmann & Simonelig, 2013). When PABPC1 levels are limited, longer poly(A) tails outcompete short poly(A) tails in PABPC1 binding, because PABPC1 binds poly(A) tails cooperatively. In *Xenopus* oocytes limited amounts of PABPC were associated with translational efficiency but had no effect on mRNA stability. In contrast, in postembryonic mammalian cells, PAPBC1 levels mainly affected the stability of mRNAs with lesser effects on translation (Xiang & Bartel, 2021). The surprisingly small effect of PABPC1 on translation was also observed in a transcriptome-wide analysis in HeLa cells. The depletion of PABPC1 could be compensated by inducible PABPC4. However, when both PABPC1 and PABPC4 were depleted, the effect on translation was negligible, but the mRNA abundance and stability of certain

subsets of mRNAs changed. mRNAs encoding proteins involved in basic cellular processes were decimated, whereas normally short-lived transcripts were unaffected in the absence of PABPC1 (Kajjo *et al.*, 2022).

The contribution of PAPBC1 to translational activation is contradictory in postembryonic cells: on the one hand, it was found to promote translation (Kahvejian *et al.*, 2005; Tarun & Sachs, 1995) but showed little effect in other studies (Mitchell *et al.*, 2010; Xiang & Bartel, 2021; Kajjo *et al.*, 2022). Because the experiments were performed in different contexts (living cells, purified proteins, or cell extracts), comparison of the apparently contradictory results is difficult (Xiang & Bartel, 2021). Thus, PABPC1 and poly(A) tail length appear to play different roles depending on the developmental stage, but also on the cell context and specific transcripts.

Interplay translation and mRNA decay

The relationship between poly(A) tail dynamics, mRNA decay, and translation is non-linear at post-embryonic cell stages and is still the subject of extensive research. mRNA decay and translation are closely linked. Inhibition of translation enhances mRNA decay (Schwartz & Parker, 1999), mRNA quality control pathways such as NMD and NGD are co-translational, and factors of the decapping and deadenylation machineries have been reported to directly interact with ribosomal proteins (Radhakrishnan *et al.*, 2016; Panasenko *et al.*, 2006; Panasenko & Collart, 2012; Dimitrova *et al.*, 2009; Buschauer *et al.*, 2020).

Several aspects such as the available tRNA pool, codon-anticodon pairing efficiency, tRNA-charges, and polypeptide folding, referred to as codon optimality have an additive effect on the elongation kinetics (reviewed in Hanson & Coller, 2018), as has been shown in yeast (Presnyak *et al.*, 2015; Webster *et al.*, 2018; Radhakrishnan & Green, 2016; Yu *et al.*,

2015) *Xenopus* (Bazzini *et al.*, 2016), *D. melanogaster* (Burow *et al.*, 2018) and human (Wu *et al.*, 2019). Codon-usage was examined as an explanation for the high variability in transcript stability as transcripts with non-optimal codons are rapidly degraded (Presnyak *et al.*, 2015; Webster *et al.*, 2018). Degradation of transcripts enriched with non-optimal codons is mediated by exonuclease Caf1/CNOT7 of the Ccr4-Not complex (Webster *et al.*, 2018) and decapping activator Dhh1 (DDX6 in mammals), which preferentially associates with slow-moving ribosomes on transcripts with non-optimal codons (Radhakrishnan *et al.*, 2016). Recently, the yeast Ccr4-Not complex was found to directly interact with the ribosome through the N-terminal domain of Not5, which interacts with ribosomes with vacant A and E sites, in case of sub-optimal codons (Buschauer *et al.*, 2020). The interaction of Not5 and the ubiquitylation of a ribosomal protein through Not4 may provide a mechanism to recruit the degradation machinery to slowly decoding ribosomes (Buschauer *et al.*, 2020).

1.2.4 Poly(A) tails and mRNA stability

Global techniques were also used to investigate genome-wide poly(A) tail lengths. The actual steady-state length of poly(A) tails was reported to be a median of ∼30 nt in yeast and between 50 and 100 nt in human, mouse, and *C. elegans* (Chang *et al.*, 2014; Subtelny *et al.*, 2014; Chang *et al.*, 2018; Morgan *et al.*, 2017; Lima *et al.*, 2017). No clear correlation between tail length and mRNA half-life was demonstrated in most somatic cells (Chang *et al.*, 2014; Subtelny *et al.*, 2014; Eichhorn *et al.*, 2016; Eisen *et al.*, 2020). Instead, a genome-wide analysis in *C. elegans* found short poly(A) tails of ∼30 nt on stable and efficiently translated mRNAs (Lima *et al.*, 2017). A study measuring both mRNA half-life and tail length in steady-state and pulse-chase experiments of the same murine fibroblast cells revealed already broad intra- and intergenic variation in initial poly(A) tail length when entering the cytoplasm (Eisen *et al.*, 2020). In this study, almost all endogenous mRNAs

were degraded via pathways associated with deadenylation; endonucleolytic cleavage or deadenylation-independent decapping played a minor role. Therefore, the individual rate of deadenylation was assumed to determine the half-life of the transcript. Deadenylation accelerated once the tail-length was below 50 nt, which would result in the loss of cooperative binding of two PABPC molecules. mRNAs with poly(A) tails shorter than 25 nt, and thus too short for efficient PABPC binding, were completely degraded (Eisen *et al.*, 2020). However, the half-lives of mRNAs with the same short poly(A) tail length of 20 nt varied between 1000-fold but transcripts that reached the short poly(A) tail state at a high deadenylation rate, were also deadenylated more rapidly (Eisen *et al.*, 2020). As the deadenylation-rate appears to vary greatly between transcripts in a sequence-dependent manner, factors such that affect it are discussed below.

***cis*-regulatory motifs** Sequence motifs within the 5' UTR or coding sequence, but mostly the 3' UTR of mRNAs such as adenylate and uridylate-rich elements (AREs), Pumilio-response elements (PRE), miRNA target sites, are recognized by *trans*-acting RNA-binding proteins (RBPs). This can lead to the formation of specific mRNPs, that can modulate the length and composition of poly(A) tails (Piqué *et al.*, 2008; Chekulaeva *et al.*, 2011). The canonical ARE represents the largest group of *cis* regulatory motifs (Bakheet *et al.*, 2006) with an abundance of 5-8 % over the human transcriptome. It contains multiple overlapping copies of the pentameric sequence AUUUA (Chen & Shyu, 1995). AREs can have destabilizing or stabilizing effects depending on the interacting RBP (reviewed in Schoenberg & Maquat, 2012). Legnini and coworkers found a positive correlation between the length of 3'UTRs, due to the use of alternative polyadenylation sites, and the respective poly(A) tail length (Legnini *et al.*, 2019). The position of cleavage and polyadenylation during mRNA maturation strongly affects which *cis*-acting motifs will be present in the mature mRNA. This consequently influences subsequent mRNA half-lives

and turnover (Weill *et al.*, 2012).

The *trans*-acting factors are regulated by a complex network of post-translational modifications that depend on cell types or signal transduction (reviewed in Schoenberg & Maquat, 2012).

mRNA structure and poly(A) tail composition Deadenylation rates were also shown to be affected by mRNA structure. Differences in mRNA structure can be introduced either by altering the primary sequence or the incorporation of modified nucleotides (Geisberg *et al.*, 2014; Mauger *et al.*, 2019). Poly(U) stretches in the 3'UTR can form stable stem loop structures with the poly(A) tail that were shown to prevent Pab1 binding in yeast and disrupt the imagined helical structure of poly(A) (Geisberg *et al.*, 2014). Secondary structures can also affect the stable binding of the deadenylase complexes and therefore alter degradation-rates (Stowell *et al.*, 2016; Raisch *et al.*, 2019). Also codon composition and translation efficiency (described in more detail in 1.2.3) affect the deadenylation rate. As well as non (A) nucleotides in the poly(A) tail, slowing down deadenylases (Rissland & Norbury, 2009; Lim *et al.*, 2014).

Overall, regulation of mRNA turnover and especially deadenylation and poly(A) tail length control is complex, transcript- and cell-specific. It differs between species as well as developmental stages. Moreover, some of the reported results currently appear contradictory. This could be partly due to further development of the methods, in particular the quite recent introduction of direct sequencing techniques for poly(A) tails (Chang *et al.*, 2014; Subtelny *et al.*, 2014; Legnini *et al.*, 2019).

One of the major cytoplasmic deadenylases, the Ccr4-Not complex, is the subject of this thesis and is described in detail in the following section.

1.3 The Ccr4-Not complex

1.3.1 Composition of the Ccr4-Not complex

The Ccr4-Not complex is conserved throughout eukaryotes and comprises two poly(A) specific deadenylases, Ccr4 (CNOT6 or paralog CNOT6L in mammals) and Ccr4-associated factor 1 (Caf1/CNOT7 or paralog CNOT8 in mammals). In *Saccharomyces cerevisiae* (*S. cerevisiae*) the complex additionally comprises the five Not proteins (Not1, Not2, Not3, Not4, Not5), Caf40 and the species specific Caf130 protein. The human complex includes additionally to the nucleases CNOT1, CNOT2, CNOT3, CNOT9, and species specific CNOT10 and CNOT11 (Chen *et al.*, 2001) (see Table 1.1). E3 ubiquitin ligase CNOT4 (Not4 in yeast) is only a facultative subunit humans and flies.

1.3.2 Discovery of the Ccr4-Not complex

Individual components of the complex were identified in genetic screens in *S. cerevisiae*. Thus were the Not proteins found to negatively regulate the transcription of the *HIS3* gene from the constitutive TATA-less promoter (Collart & Struhl, 1994). Ccr4 was found as an activator of glucose-repressible alcohol dehydrogenase (ADH2) (Denis, 1984; Denis & Malvar, 1990) and its associated factor Caf1 in yeast-two hybrid assays (Draper *et al.*, 1995). The link between the Not proteins and the Ccr4-complex resulted from identification of the Not proteins as co- immunoprecipitates of Caf1 and Ccr4 (Liu *et al.*, 1998). Purification and mass spectrometry analysis of a 1 MDa Ccr4-Not complex from yeast identified two constitutive subunits, Caf40 and Caf130 (Chen *et al.*, 2001). Therefore, initially, the Ccr4-Not complex was associated with nuclear functions in transcription regulation. Later, Ccr4 and Caf1 were reported to be essential for deadenylation in the cytoplasm in yeast (Tucker *et al.*, 2001; Daugeron *et al.*, 2001), leading to an important role for Ccr4-Not in mRNA decay.

Table 1.1. Composition of Ccr4-Not in various species.

Gene name	*S. cerevisiae*	*D. melanogaster*	*H. sapiens*	Function
Not1	Not1	Not1/CDC39	CNOT1	scaffold
Not2	Not2/CDC36	RGA	CNOT2	
Not3	Not3	-	-	
Not4	Not4/MOT2/Sig1	Not4	CNOT4	RING E3
Not5	Not5	Not3	CNOT3	
Caf1	Caf1/POP2	Pop2	CNOT7/CNOT8	nuclease
Ccr4	Ccr4	twin	CNOT6/ CNOT6L	nuclease
Caf40	Caf40	Rcd1	CNOT9/Caf40	protein interactions
Not10	-	Not10	CNOT10	
Not11	-	Not11	CNOT11/C2orf29	
Caf130	CAF130	-	-	

1.3.3 Functional roles of the Ccr4-Not complex

In addition to recruitment to constitutive mRNA decay, the complex is recruited by RBPs to specific mRNA targets to repress translation or promote rapid mRNA degradation. These RBPs include Tristetraprolin (TTP), Pumilio/FBF, GW182, Nanos, Roquin, Bicaudal, YTHDF2, and RNF219, among others (Fabian *et al.*, 2013; Enwerem *et al.*, 2021; Chekulaeva *et al.*, 2011; Fabian *et al.*, 2011; Sgromo *et al.*, 2017; Bhandari *et al.*, 2014; Leppek *et al.*, 2013; Chicoine *et al.*, 2007; Du *et al.*, 2016; Poetz *et al.*, 2021). The interaction of these RBPs with parts of Ccr4-Not complex is often mediated by multiple short linear motifs (SLiMs) (reviwed in Passmore & Coller, 2021). RBPs are often regulated by phosphorylation; for example, binding of TTP to Ccr4-Not is impaired when the CNOT1-interacting motif (CIM) of TTP is phosphorylated (Fabian *et al.*, 2013).

The complex was also shown to contribute to translational repression by recruiting translational repressor DDX6 (Chen *et al.*, 2014; Mathys *et al.*, 2014) (described in more detail in 1.3.4). Subunits of the Ccr4-Not complex were also associated with other cellular processes such as transcription, nuclear export, and protein quality control. However, whether

these interactions occur in the presence of the entire complex and the specific role of the complex in processes other than mRNA degradation remain unclear (reviewed in Collart & Panasenko, 2012).

1.3.4 Architecture of the human Ccr4-Not complex

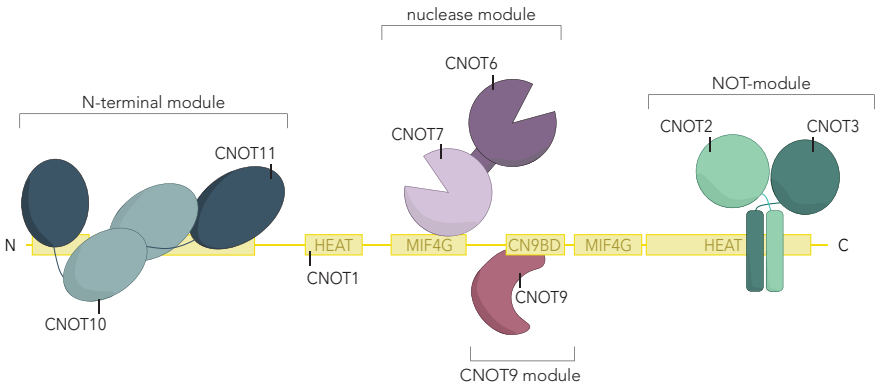

Figure 1.2. Architecture of the human Ccr4-Not complex. Schematic representation of the human Ccr4-Not complex. It is organized modularly around scaffold protein CNOT1 (pale yellow). Rectangles indicate globular domains; lines show extended sequences of CNOT1. The N-terminus of CNOT1 associates with the N-terminal module consisting of CNOT10 (light blue) and CNOT11 (dark blue). The central part of CNOT1 provides binding sites for the nuclease module comprising two nucleases, CNOT6 (deep purple) and CNOT7 (light purple) and the CNOT9-module (dark red). The C-terminus of CNOT1 is bound by the NOT-module, which includes CNOT2 (light green) and CNOT3 (dark green).

The Ccr4-Not complex is modularly organized around the large scaffold protein CNOT1 (Not1 in yeast) (Fig. 1.2). The current model of its organization predicts its modular organization being flexible and dynamic despite its comparatively large size (~700 kDa). Nevertheless, high-resolution structures of all individual modules and consequently large parts of CNOT1/Not1 have been solved by X-ray crystallography.

Structural studies of the global architecture of the Ccr4-Not complex have so far been limited to complexes from yeast species, albeit at medium to low resolution (Ukleja *et al.*, 2016; Nasertorabi *et al.*, 2011).

The domain architecture of scaffold protein CNOT1 is shown in Figure 1.3. It consists

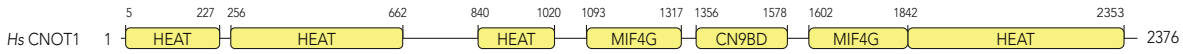

Figure 1.3. Domain organization of *Hs* CNOT1. Schematic representation of the domain architecture of human CNOT1 (pale yellow). Rectangles indicate globular domains; lines show extended sequences of CNOT1. Numbers refer to domain boundaries.

mainly of helical HEAT (Huntingtin, elongation factor 3, protein phosphatase 2A, yeast kinase TOR1) repeats (Andrade & Bork, 1995). The individual modules will be described in more detail in the following sections in the order of their binding to the N- to C-terminus of CNOT1. At its N-terminus, CNOT1 provides binding sites for species-specific proteins: Caf130 in yeast (Chen *et al.*, 2001), and CNOT10 and CNOT11 in human cells. The central part of CNOT1 has a HEAT repeat structure that adopts a MIF4G (middle domain of eukaryotic initiation factor G) fold and recruits the two deadenylases CNOT6 (Ccr4 in yeast) and CNOT7 (Caf1 in yeast) to form the nuclease module of the complex (Bai *et al.*, 1999; Basquin *et al.*, 2012; Petit *et al.*, 2012). The MIF4G domain is followed by the CNOT9 binding domain (CN9BD), which, unlike other regions, is built up by a rod-like three-helix-bundle. The CN9BD binds CNOT9 (Caf40 in yeast). A second MIF4G domain is located upstream of the C-terminal HEAT repeats of CNOT1, that provide binding sites for two tightly bound subunits of the NOT module, CNOT2 and CNOT3 (Not2 and Not5 in yeast) (Bhaskar *et al.*, 2013; Boland *et al.*, 2013).

Interactors of CNOT1

CNOT1 mediates, often together with CNOT9, the recruitment of regulators: the helicase and translational repressor DDX6, the microRNA factor GW182/TNRC6C, and ARE-binding protein (ARE-BP) TTP (Braun *et al.*, 2011; Chekulaeva *et al.*, 2011; Chen *et al.*, 2014; Mathys *et al.*, 2014; Rouya *et al.*, 2014; Fabian *et al.*, 2013; Bulbrook *et al.*, 2018). The interactors DDX6 and TTP are described in more detail in the following sections since they are of importance for the work conducted here.

DDX6 The DEAD-box RNA-helicase DDX6 (Dhh1 in yeast) is an activator of mRNA decapping and decay and involved in translation repression in miRNA-mediated gene silencing among other pathways (Sheth & Parker, 2003; Parker & Sheth, 2007; Chu & Rana, 2006; Chen *et al.*, 2014; Mathys *et al.*, 2014; Rouya *et al.*, 2014). DDX6 is an RNA-dependent ATPase with two tandem RecA domains (RecA1 and RecA2), primarily positioned in a rigid, auto-inhibited 'apo' conformation (Ozgur *et al.*, 2015b). It was shown to interact directly with Ccr4-Not through the central MIF4G domain of CNOT1 (Coller *et al.*, 2001; Hata *et al.*, 1998; Maillet & Collart, 2002; Temme *et al.*, 2010). Upon binding to CNOT1, the RecA domains undergo a major conformational change from apo state to the typical conformation of active DEAD box proteins (Mathys *et al.*, 2014). The activation of DDX6 through interaction with CNOT1 was shown to be essential for its role in miRNA repression, and may represent a physical link between deadenylation and decapping (Chen *et al.*, 2014; Mathys *et al.*, 2014). Superposition of previously solved structures of CNOT1-Caf1 showed that both interactions are possible and not mutually exclusive, incorporating the helicase into the Ccr4-Not complex (Chen *et al.*, 2014).

RNA-binding of DDX6 can be modulated by effectors such as Pat1, EDC3, Lsm14, and 4E-T, through unfavorable or favorable electrostatic interactions (Sharif *et al.*, 2013; Tritschler *et al.*, 2009; Ozgur *et al.*, 2015a).

TTP The RNA-binding protein TTP regulates the half-life of mRNAs containing AREs by recruiting factors that suppress translation and degrade the mRNA. TTP, in addition to containing proline-rich regions and a central tandem CCCH-type central zinc finger domain, that interacts with AREs in the 3'UTR of its target mRNAs (Lai *et al.*, 2000), also contains large intrinsically disordered sections N- and C-terminal to the zinc finger domain (see Fig. 1.4, each of which can promote mRNA decay (Lykke-Andersen & Wagner, 2005). A conserved motif at its C-terminus, the CIM, interacts directly with a HEAT repeat domain in the center of CNOT1, as shown by the crystal structure of a TTP-CNOT1 complex (Fabian *et al.*, 2013). An additional interaction with CNOT9 using the same tryptophan (TRP) binding pockets as GW182, was shown for conserved TRPs in TTP (Bulbrook *et al.*, 2018; Chen *et al.*, 2014; Mathys *et al.*, 2014). The interactions of TTP with CNOT1 and CNOT9 recruit the Ccr4-Not complex and promote deadenylation of target transcripts (Carreno & Lykke-Andersen, 2022). The tetraproline motifs associate with the cap-binding 4EHP-GYF2 complex, involved in translational repression (Fu *et al.*, 2016). Additionally, TTP can associate with decapping factors such as DDX6 and EDC4 (Carreno & Lykke-Andersen, 2022).

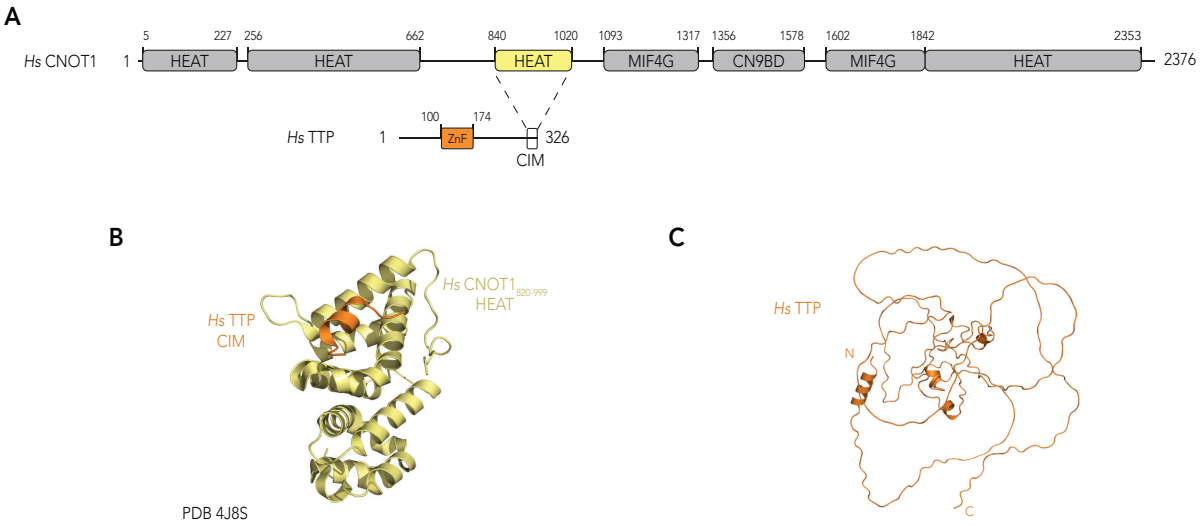

Figure 1.4. Domain organization of TTP and interaction with CNOT1. A, Schematic representation of the domain organization of *Hs* CNOT1 and *Hs* TTP. Segments, absent in the crystal structure in **B** are colored in grey. Folded domains are indicated by rectangles and extended sequences by lines. Numbers refer to domain boundaries. A C-terminal CNOT1-interacting motif (CIM) of TTP interacts with a HEAT repeat in CNOT1. **B**, Cartoon representation of a crystal structure of the C-terminal CIM peptide of *Hs* $TTP_{314\text{-}325}$ (orange) and *Hs* $CNOT1_{820\text{-}999}$(pale yellow)(Fabian *et al.*, 2013). **C**, Predicted 3D structure of *Hs* TTP by AlphaFold 2 (Jumper *et al.*, 2021).

TTP is itself highly regulated, because many of its target mRNAs are involved in short-term inflammatory responses (e.g., TNF-α, cyclooxygenase-2, interleukin (IL)-1α, IL-1β, and lymphomas (Sanduja *et al.*, 2012)). Its stability, binding affinity and subcellular localization are controlled by post-translational modifications (reviewed in Schoenberg & Maquat, 2012).

Phosphorylation of TTP after an inflammatory stimulus leads to stabilization of TTP and promotes binding of 14-3-3 (Sandler *et al.*, 2011; Johnson *et al.*, 2002). The interaction with 14-3-3 provides a mechanism for nuclear export of TTP. Phosphorylation of the CIM has been shown to impair association with the Ccr4-Not complex (Clement *et al.*, 2011; Fabian *et al.*, 2013). This reduces deadenylation and ensures translation of inflammatory proteins until the stimulus disappears and TTP in turn becomes dephosphorylated and active to promote deadenylation and degradation of the specific mRNAs. TTP itself is

subject to proteasome-mediated decay (Brook *et al.*, 2006).

The N-terminal module

The interaction partners of the CNOT1 N-terminus are species-specific. In *Drosophila* and human cells, CNOT10 and CNOT11 were shown to interact with the N-terminal region of CNOT1, with no known homologs in yeast (Mauxion *et al.*, 2013; Bawankar *et al.*, 2013). The crystal structure of the ternary complex adopts a highly unusual tightly interwoven architecture (see fig. 1.5 (unpublished). CNOT11 consists of two globular domains, with the C-terminal domain showing similarity to MIF4G folds, being highly conserved and probably flexibly attached. The N-terminal domain of CNOT11 is less conserved and involved in CNOT1 binding. Both domains are connected via a ∼50 residue long linker. CNOT10, composed of 13 tetratricopetide repeats (TPRs), wraps around the linker domain of CNOT11 and is sandwiched between two domains of the N-terminus of CNOT1, which consist of HEAT repeats. The structural arrangement may explain previous findings that indicated both proteins must be present to form a complex with CNOT1 (Mauxion *et al.*, 2013; Bawankar *et al.*, 2013). The function of the N-terminal module has not been fully elucidated. The conserved C-terminal MIF4G-like domain of CNOT11 serves as protein-protein interaction platform, as shown for GGNBP2, a tumor suppressor also involved in spermatogenesis (unpublished), pointing towards a regulatory role of the module. The N-terminal module, like the other non-enzymatic modules of the Ccr4-Not complex, was shown to modulate the deadenylase activity of the complex. Under EMSA conditions, it bound substrate RNA and compensated for the presence of an RBP that blocked the RNA-binding surface of CNOT9 (Raisch *et al.*, 2019). A study examining genetic interactions associated with viral infection linked the Ccr4-Not complex to innate immunity. Specifically, CNOT10 and CNOT11 were required to suppress interferon stimulated genes

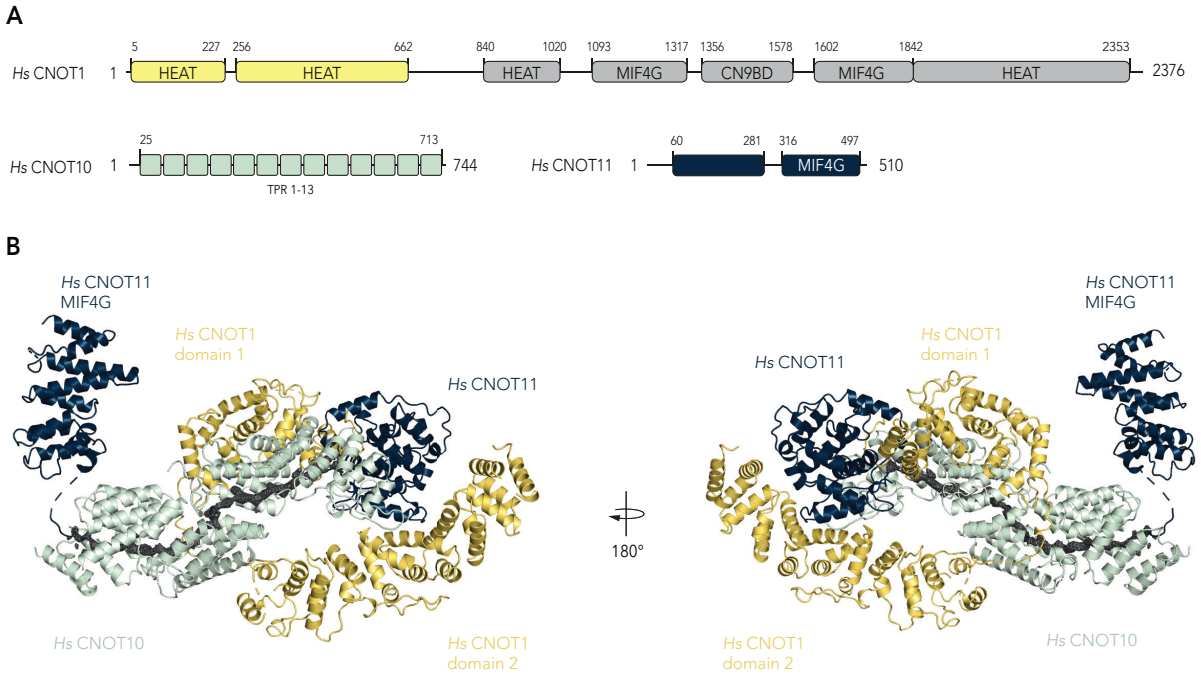

Figure 1.5. The N-terminal module. A, Schematic representation of the domain organization of *Hs* CNOT1, *Hs* CNOT10, and, *Hs* CNOT11. Segments, absent in the crystal structure in **B** are colored in grey. Folded domains are indicated by rectangles and extended sequences by lines. Numbers refer to domain boundaries. **B,** Crystal structure of a ternary CNOT1-N (pale yellow) - CNOT10 (pale green) - CNOT11 (dark blue) complex in cartoon representation, related by a 180°rotation around a vertical axis (unpublished).

in primary CD4+ T cells during HIV infection (Gordon *et al.*, 2020). The authors also found an N-terminally truncated version of CNOT1 that was no longer able to bind the N-terminal module, and speculated the existence of two Ccr4-Not complexes within an individual cell (Gordon *et al.*, 2020).

The nuclease module

Two exonucleases, Ccr4 (CNOT6) and Caf1 (CNOT7), conserved in eukaryotes except protists, form the catalytic core of Ccr4-Not (Bai *et al.*, 1999). The equivalent complex in trypanosomes contains only the exonuclease Caf1 and is therefore called Caf1-Not complex (Erben *et al.*, 2014). The nucleases were first discovered in yeast (Denis, 1984; Sakai

et al., 1992), and are not essential, however *ccr4*△ and *caf1*△ yeast strains show defects in cell growth and mRNA decay (Tucker *et al.*, 2001). Depletion of CNOT7 in HeLa cells using RNAi, leading to loss of both nucleases, results in increased mRNA stability after actinomycin D treatment and accumulation of mRNAs with poly(A) tails ∼150 nt length in bulk poly(A) assays, indicating that the complex acts mainly on ∼150 nt poly(A) tails (Yi *et al.*, 2018). The crystal structures shown in Fig. 1.6 revealed two distinct nucleases with different domain architectures.

CNOT6 is a poly(A) specific, Mg^{2+} dependent 3' exonuclease, belonging to the family of exonuclease-endonuclease-phosphatases (EEP). The crystal structures of CNOT6L and CNOT6 consist of a heart-shaped nuclease domain with two central β-sheets and α-helices forming the lobes of the heart (Wang *et al.*, 2010; Chen *et al.*, 2021). These are flexibly connected to the Leucine rich repeat (LRR) domain, which has a convex, positively charged patch towards the nuclease domain that could contribute to RNA substrate guidance. CNOT6 is thought to recognized the terminal nucleotide with a HWDP-loop folding the terminal nucleotide away from the remainder of the substrate. It is not fully understood whether one or two metal ions are involved in the reaction mechanism (Chen *et al.*, 2021).

CNOT7 belongs to the family of DEDD nucleases, coordinating two-divalent metal ions with its DEDD residues and a structurally flexible histidine supporting the substrate binding. CNOT7 is thought to recognize poly(A) probably via the RNA backbone geometry and stacking of A (Chen *et al.*, 2021), similar to the PAN2 homolog from *S. cerevisiae* (Tang *et al.*, 2019).

The crystal structure of a yeast Not1:Caf1:Ccr4-subcomplex revealed the molecular basis of the interaction of Caf1 with the central MIF4G of CNOT1 and the interaction between Caf1 and Ccr4 (Basquin *et al.*, 2012).

Despite the rather low sequence identity of 36 % for Ccr4 and 41 % for Caf1 between human and *S. cerevisiae* nucleases, the crystal structure of human CNOT6:CNOT7 complex (Chen *et al.*, 2021) looks very similar. Differences concern the orientation of the nuclease domain of Ccr4 relative to Caf1, which is rotated ∼80°, suggesting a flexible attachment to the LRR domain, as well as an N-terminal extension of yeast Ccr4. A positively charged patch on the LRR domain is also missing in the yeast protein. The active site of yeast Caf1, comprises SEDQt instead of the canonical DEDDh, implying lower deadenylation activity, and thus likely plays a more structural role in binding Ccr4 to the complex (Chen *et al.*, 2021).

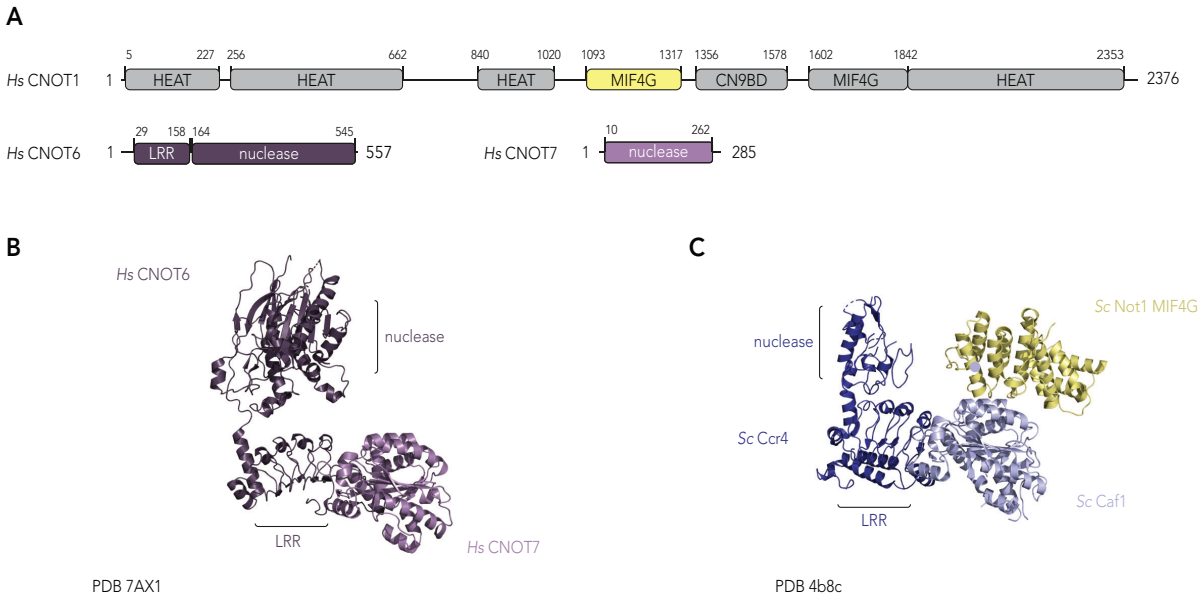

Figure 1.6. The nuclease module. **A,** Schematic representation of domain organization of *Hs* CNOT1, *Hs* CNOT6, and *Hs* CNOT7. Segments, absent in the crystal structure in **B** are colored in grey. Folded domains are indicated by rectangles and extended sequences by lines. Numbers refer to domain boundaries. **B,** Crystal structure of a *Hs* CNOT6 (purple):*Hs* CNOT7(light purple) complex in cartoon representation (Chen *et al.*, 2021). **C,** Crystal structure of a ternary *Sc* Not1 (pale yellow): *Sc* Ccr4 (dark blue) : *Sc* Caf1 (pale blue) complex in cartoon representation (Basquin *et al.*, 2012).

The presence of two nucleases in one complex is an intriguing feature of Ccr4-Not. Catalytically inactive mutants of one or both deadenylases allowed *in vitro* investigation of their individual influence on degradation (Webster *et al.*, 2018; Yi *et al.*, 2018; Raisch

et al., 2019; Chen *et al.*, 2021). Both are strict 3'-exonucleases that recognize up to three nucleotides, which is important to avoid endonucleolytic cleavage and maintain mRNA integrity (Chen *et al.*, 2021). In general, CNOT6 appears to be more selective for poly(A) nucleotides. Since non-(A) nucleotides are incorporated into poly(A) tails as a result of regulatory processes and/or misincorporation in the cell (Legnini *et al.*, 2019; Lim *et al.*, 2018), it is important that they can be removed. However, the reported nucleotide specificity and activity varied, between and also within species, as well as between isolated nucleases or in the context of the whole complex. This is likely due to species-specific adaptations or different experimental setups in the ratio of RNA to enzyme, but could also be the result of differing pH conditions in the *in vitro* deadenylase assays, as the activity of the human CNOT7 appears to be strongly influenced by the surrounding pH, and the concentration of Mg^{2+} and Zn^{2+} (Chen *et al.*, 2021). The presence of Pab1 or PABPC1 has a strong effect on the isolated fission yeast or human nucleases. While Caf1/CNOT7 was inhibited by Pab1/PABPC1, Ccr4/CNOT6 was able to release the poly(A) binding protein and subsequently to degrade the poly(A) tail (Webster *et al.*, 2018; Yi *et al.*, 2018). However, it is unclear whether this behavior is consistent in the context of the entire complex. Caf1 can interact with BTG2, which in turn can bind PABPC1, so it does not rely on Ccr4 to degrade poly(A) tails in the presence of PABPC1 (Stupfler *et al.*, 2016). Caf1 was also shown to be a target of posttranslational modifications such as acetylation and ubiquitylation, that modulate its deadenylase activity (Sharma *et al.*, 2016; Cano *et al.*, 2015).

Interaction partners of the nuclease module B-cell translocation genes (BTG) /TOB) are a group of antiproliferative proteins (in mammals: BTG1, BTG2, BTG3, BTG4, as well as Tob1 and Tob2), involved in the regulation of cell differentiation, development and apoptosis. Accordingly, their expression is decreased in many cancers (Maux-

ion *et al.*, 2008). BTG/TOB proteins possess an N-terminal conserved APRO (antiproliferative) domain that interacts directly with CNOT7/CNOT8 (with the exception of BTG4) (Mauxion *et al.*, 2009; Winkler, 2010). While both Tob proteins also interact with the MLLE domain of PABPC1 via their C-terminal PAM2 motif, the APRO domain of BTG1 and BTG2 was also shown to bind the first RRM of PABPC1 (Stupfler *et al.*, 2016). The interactions of BTG2 with CNOT7 and PABPC1 through the APRO domain are not mutually exclusive and it was shown in *in vitro* deadenylation assays with isolated CNOT7 that the addition of PABPC and BTG2 accelerated the deadenylation reaction. In this context, stimulation of deadenylation correlated with antiproliferative effects (Stupfler *et al.*, 2016).

The CNOT9 module

CNOT9 (Caf40) associates with the Ccr4-Not complex by interacting with the CNOT9 binding domain (CN9BD), a rod-shaped three-helix bundle in the middle of CNOT1 and mediates protein-protein interactions between Ccr4-Not and interactors, as well as RNA binding properties (Garces *et al.*, 2007; Chen *et al.*, 2014; Mathys *et al.*, 2014). CNOT9 adopts six Armadillo (ARM) repeats of three helices each, both in isolation (Garces *et al.*, 2007; Chen *et al.*, 2014; Mathys *et al.*, 2014) and in complex with CNOT1 (Chen *et al.*, 2014; Mathys *et al.*, 2014). Multiple mutations on both sides were required to disrupt binding to CNOT1, indicating a high-affinity interaction (Chen *et al.*, 2014).

Interactors of CNOT9 CNOT9 serves as binding platform for RBPs, promoting selective mRNA degradation. The identified tryptophan binding sites have been shown to interact with tryptophan residues of ARE-binding protein TTP (Bulbrook *et al.*, 2018), and GW182 (TNR6A-C in mammals). Interaction with GW182 contributes together with CNOT1 to recruit Ccr4-Not to miRNA targets (Chekulaeva *et al.*, 2011; Fabian *et al.*,

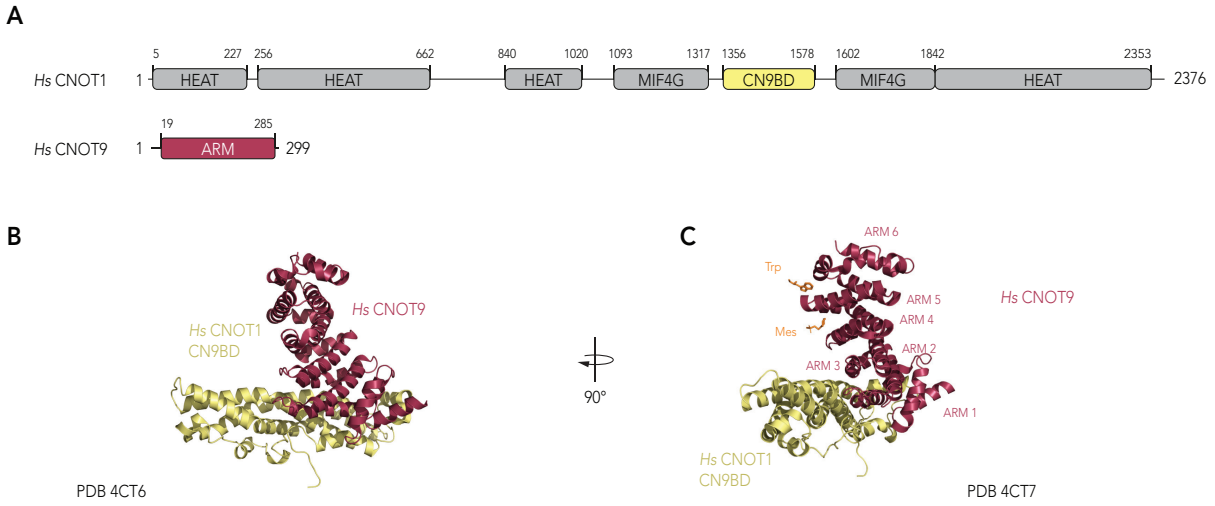

Figure 1.7. The CNOT9 module. A, Schematic representation of the domain organization of *Hs* CNOT1 and *Hs* CNOT9. Segments, absent in the crystal structure in **B,C** are colored in grey. Folded domains are indicated by rectangles and extended sequences by lines. Numbers refer to domain boundaries. **B,** The crystal structure of CNOT1 (pale yellow) in complex with CNOT9 (red) in cartoon representation shows the CN9BD as a three-helix-bundle and CNOT9 built up by six ARM repeats (Mathys *et al.*, 2014) **C,** A crystal structure after soaking free tryptophan in CN9BD-CNOT9 crystals revealed two W-binding pockets between ARM 5 and ARM 6, as well as between ARM 5 and ARM 4, which bound small molecules tryptophan and MES (orange) (Mathys *et al.*, 2014).

2011).

The concave surface of CNOT9 can bind RNA (Garces *et al.*, 2007; Raisch *et al.*, 2019), but also other RBPs such as the E3 ubiquitin ligase CNOT4 (Keskeny *et al.*, 2019), *Dm* Bag-of-marbles (Bam), Roquin (Sgromo *et al.*, 2018, 2017) and RNF219 (Poetz *et al.*, 2021). The interactions are mediated in similar manners via SLiMs. While interactions of *Drosophila* Bam or Roquin (Sgromo *et al.*, 2018, 2017) are mutually exclusive as they bind the same surface on CNOT9, simultaneous binding may be possible for proteins that bind to tryptophan-binding pockets of CNOT9, such as TNRC6 or TTP (Keskeny *et al.*, 2019). Titration with SLiMs of Bam or RNF219 inhibited Ccr4-Not mediated deadenylation *in vitro*, probably because of impaired RNA binding, which represents a possible mechanism for inhibiting deadenylation when a specific RBP binds CNOT9 (Raisch *et al.*, 2019; Poetz *et al.*, 2021).

CNOT4

The RING E3 ubiquitin ligase CNOT4 (Not4 in yeast) is evolutionary conserved but, unlike yeast, in mammals and flies not a constitutive subunit of the complex (Lau *et al.*, 2009; Temme *et al.*, 2010). The N-terminus is highly conserved and contains a RING domain, an RRM, and a C3H1-type zinc finger domain, whereas the C-terminus is predicted as a low-complexity region. CNOT4 from metazoans binds to CNOT9 with its conserved C-terminal Caf40-binding motifs (CBMs), supported by flanking regions (Keskeny *et al.*, 2019). This is in contrast to yeast, where Not4, which lacks CBMs, interacts with the C-terminus of CNOT1 (Bhaskar *et al.*, 2015). Ubiquitin ligase activity depends on the interaction with E2 protein Ubc4/5 in yeast and UbcH5B in humans (Mulder *et al.*, 2007; Albert *et al.*, 2002). CNOT4 has been reported to ubiquitinate various proteins such as the nascent chain complex (Panasenko *et al.*, 2006), the Histone demethylase JHD2 (Mersman *et al.*, 2009), and ribosomal protein Rps7A (Panasenko & Collart, 2012). It also plays a role in co-translational mRNA quality control (Dimitrova *et al.*, 2009) and NMD-coupled protein quality control (Inglis *et al.*, 2021).

The NOT-module

The C-terminal HEAT repeats of Not1/CNOT1 provide binding sites for two cooperatively binding subunits of the Ccr4-Not complex (Not2-Not5 in yeast and CNOT2-CNOT3 in humans). This module formed at the C-terminus if CNOT1 is called the NOT-module. Ternary complexes of yeast Not1:Not2:Not5 and human CNOT1:CNOT2:CNOT3 have been crystallized (Bhaskar *et al.*, 2013; Boland *et al.*, 2013). Both structures reveal similar architecture of the NOT module, where the C-terminus of CNOT1/Not1 is built up by HEAT repeats in a T-shaped architecture, with HEAT motifs 7-10 arranged perpendicular to HEAT motifs 1-6. The C-terminal NOT box domains of CNOT2 (Not2) and

CNOT3 (Not5) resemble Sm folds but lack the canonical fifth β strand, thus forming a heterodimer with their N-terminal extensions. This NOT-box-NOT-box heterodimer anchors to CNOT1/Not1 with extended N-terminal regions (Boland *et al.*, 2013; Bhaskar *et al.*, 2013). Binding is thought to occur in a transition from disorder to order and co-folding (Boland *et al.*, 2013). The formation of a heterodimer is hereby advantageous because of a better complementarity compared to a homodimer. The yeast homologs of CNOT3, Not3 and Not5, are very similar and probably arose by gene duplication (Collart *et al.*, 2013). However, they differ in their NOT boxes, and Not3, has been shown to no longer interact with the NOT box of Not2 in vitro (Bhaskar *et al.*, 2013). Moreover, deletion of Not5 is critical for vegetative growth in yeast, whereas deletion of Not3 has little effect (Oberholzer & Collart, 1998). Therefore, CNOT3 is likely an ortholog of the yeast Not5 protein. In contrast to the human NOT-module, a positive patch on the yeast NOT-module, was reported to bind poly(U) RNA *in vitro* (Bhaskar *et al.*, 2013).

Interactors of the NOT module The NOT module, which lacks catalytic domains, acts as a structural and regulatory support and provides a platform for RBPs that recruit Ccr4-Not to specific mRNA targets. Thus interactions with the NOT module have been reported for *Dm* protein Bicaudal-C, developmental regulator Nanos, Pumilio 1&2, and Roquin, which promotes degradation of CDE containing mRNAs (Leppek *et al.*, 2013; Suzuki *et al.*, 2010; Chicoine *et al.*, 2007; Bhandari *et al.*, 2014; Enwerem *et al.*, 2021). The RNA-binding properties of the yeast NOT module link it to deadenylation-independent degradation pathways that frequently involve poly(U) tracts (Bhaskar *et al.*, 2013; Muhlrad & Parker, 2005). As recently reported, Not5 in yeast can interact with slowly decoding ribosomes that in the case of non-optimal codons exhibit vacant A and E sites and adopt a specific conformation. It was therefore suggested that Ccr4-Not monitors the elongation-rate to promote mRNA decay when needed (Buschauer *et al.*, 2020). Genetic experiments

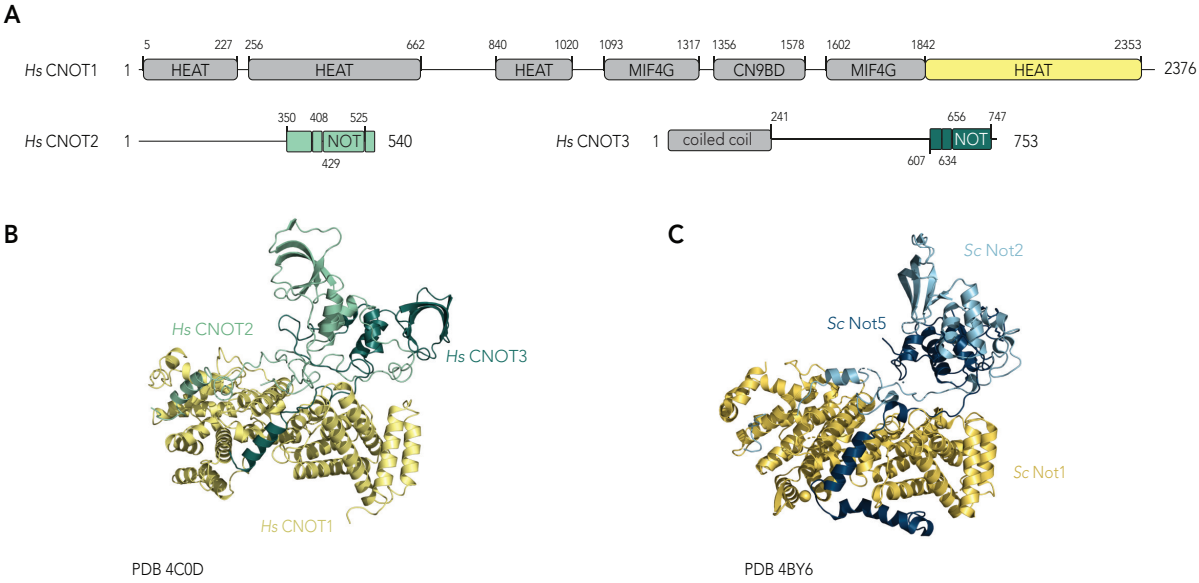

Figure 1.8. Structure of the NOT-module. A, Domain organization of *Hs* CNOT1, $CNOT2_{344\text{-}540}$, and $CNOT3_{607\text{-}753}$. Segments, absent in the crystal structure in **B** are colored in grey. Folded domains are indicated by rectangles and extended sequences by lines. Numbers refer to domain boundaries. **B,** Crystal structure in cartoon representation of human $CNOT1_{1565\text{-}2371}$ (pale yellow) CNOT2 (green) and CNOT3 (dark green) (Boland *et al.*, 2013) and **C,** of yeast Not1 (yellow) Not2 (light blue) and Not5 (dark blue) (Bhaskar *et al.*, 2013).

in yeast connected the NOT module to the transcription machinery (Collart & Panasenko, 2012; Miller & Reese, 2012).

1.4 Aim of this thesis

mRNA decay is an important post-transcriptional mechanism to regulate eukaryotic gene expression. Deadenylation of the 3'-terminal poly(A) tail is the first and rate-limiting step in canonical mRNA decay, which is carried out by two multiprotein complexes, the Pan2-Pan3 and Ccr4-Not deadenylases. Pan2-Pan3 acts in a distributive manner preferentially on long poly(A) tails covered with multiple PABPC molecules, whereas the Ccr4-Not complex removes the poly(A) closer to the 3'UTR. The human Ccr4-Not is a protein complex consisting of eight stably associated subunits that dock to a large scaffold protein CNOT1. It is recruited by RBPs such as TTP to shorten the poly (A) tail of its target mRNAs.
Although the architecture of Ccr4-Not has been intensively studied, high-resolution structures are only available for individual subcomplexes due to the size and flexibility of the complex. The only global structures are of yeast species at low to medium resolution. The aim of this work was to solve the structure of the full-length human Ccr4-Not complex. Therefore, a method for recombinant expression and purification of the complex had to be established first. The resulting protocol was scalable and provided sufficient high-quality material for functional and structural studies. The heterologously expressed and purified complex was characterized biochemically *in vitro* in deadenylation and targeted deadenylation experiments in the presence of one of its binding partners, TTP.
Negative staining and cryo-electron microscopy as well as cross-linking followed by mass-spectrometry (XL-MS) were used to structurally characterize the complex. The resulting 3D-reconstruction of the full complex, achieved however only medium resolution. The results and future perspectives are presented in the following sections.

Chapter 2

Materials

2.0.1 Consumables and chemicals

All common chemicals used in this study were purchased from Sigma-Aldrich, Roth , Merck or Thermo Fisher Scientific unless stated otherwise.

2.0.2 Enzymes

Table 2.1. List of enzymes used in this study.

Enzyme	**Source**
Gibson Assembly Mix	MPIB core facility
HRV 3C Protease	expression and purification in Conti department
SUMO protease	expression and purification in Conti department
Restriction enzymes	New England Biolabs (NEB)
Phusion Flash High-Fidelity PCR Master Mix	Thermo Scientific
T4 DNA ligase	NEB
T4 DNA Polymerase (LIC-qualified)	Novagen

2.0.3 DNA and RNA oligonucleotides

DNA oligonucleotides were ordered desalted and lyophilized from Sigma-Aldrich and Eurofins/MWG (Ebersberg). They were dissolved in ddH_2O and stored at -20 °C.

Vectors and plasmids

Table 2.2. List of vectors used in this study.

Vectors	Source/Vendors	Expression Host	Bacterial Resistance
pEC-A-3C-TRX	Conti Lab	*E. coli*	Ampicillin
pEC-A-3C-ZTA	Conti Lab	*E. coli*	Ampicillin
pEC-A-Hi-SUMO	Conti Lab	*E. coli*	Ampicillin
pEC-A-His-GST-3C	Conti Lab	*E. coli*	Ampicillin
pEC-K-3C-TRX	Conti Lab	*E. coli*	Kanamycin
pEC-K-Hi-SUMO	Conti Lab	*E. coli*	Kanamycin
pEC-S-CDF-3C-TRX	Conti Lab	*E. coli*	Streptomycin
pLIB	Jan-Michael Peters	Insect cells	Ampicillin
pBIG1a	Jan-Michael Peters	Insect cells	Ampicillin/Spectinomycin
pBIG1b	Jan-Michael Peters	Insect cells	Ampicillin/Spectinomycin
pBIG2ab	Jan-Michael Peters	insect cells	Ampicillin/Chloramphenicol
pFastBac1	Invitrogen	insect cells	Ampicillin/Gentamicin
pFastBac	Invitrogen	insect cells	Ampicillin/Gentamicin
pFastBac-HTA	Invitrogen	insect cells	Ampicillin/Gentamicin

Table 2.3. List of constructs used in this study.

Construct	Vector	Affinity-Tag N-term	Affinity-Tag C-term	Cleavage-Site	Source	Primers
CNOT1 (813-1596)	pEC-A-His-GST-3C	6xHis-GST	-	3C	Conti-Lab	-
CNOT1 (1-2371)	pBig1A	6xHis-TEV	-	TEV	this study	
CNOT1 (813-1596)	pFastBac1-His-3C	6xHis-3C		3C	this study	60,58
CNOT1 (1-2371)	pFastBacHTA	6xHis-TEV	-	TEV	Conti-Lab	-
CNOT1 (1-2371)	pFastBacHTA	6xHis-TEV	3C-MBP	TEV, 3C	Conti-Lab	-
CNOT1 (1-1596)	pMMS-TRX	6xHis-TRX	-	3C	Conti-Lab	-
CNOT2 (1-540)	pLIB	-	-	-	this study	107,108
CNOT2 (1-540)	pFastBac-His-3C	6xHis-3C	-	3C	this study	85,86
CNOT3 (1-753)	pFastBac-His-3C	6xHis-3C	Ctag	3C	this study	80,83
CNOT3 (1-753)	pFastBac1	-	Ctag	3C	this study	80,79
CNOT6 (1-557)	pEC-S-CDF-3C-TRX	6xHis-TrxA	-	3C	Conti Lab	-
CNOT6 (1-557)	pFastBac-His-3C	6xHis-3C	-	3C	this study	54,55
CNOT6 (1-557) (E240A)	pFastBac-His-3C	6xHis-3C	-	3C	this study	54,55
CNOT6 (1-557)	pLIB		-		this study	101,102
CNOT6 (1-557) (E240A)	pLIB		-	-	this study	101,102
CNOT7 (1-246)	pEC-A-3C-TRX	6xHis-TrxA	-	3C	Conti Lab	-
CNOT7 (1-246)	pFastBac-His-3C	6xHis-3C	-	3C	this study	52,53
CNOT7 (1-246) (D40A, E42A)	pFastBac-His-3C	6xHis-3C	-	3C	this study	52,53
CNOT7-3C-CNOT6	pFastBac-His-3C	6xHis-3C	-	3C	this study	52,56,57
CNOT7(D40A, E42A)-3C-CNOT6 (E240A)	pFastBac-His-3C	6xHis-3C	-	3C	Conti Lab	-
CNOT7 (1-246)	pLIB	-	-	-	this study	103,104
CNOT7 (1-246) (D40A, E42A)	pLIB	-	-	-	this study	103,104
CNOT9 (1-299)	pEC-A-Hi-SUMO	6xHis-SUMO	-	SUMO	Conti Lab	-
CNOT9 (1-299)	pEC-K-Hi-SUMO	6xHis-SUMO	-	SUMO	Conti Lab	-
CNOT9 (1-299)	pFastBac-His-3C	6xHis-3C	-	3C	this study	66,67
CNOT9 (1-299)	pLIB	-	-	-	this study	105,106
CNOT10 (1-714 Δ492-504)	pEC-K-3C-TRX	6xHis-TrxA	-	3C	Conti Lab	-
CNOT10 (1-744)	pFastBac	-	-	-	Conti Lab	-
CNOT11 (61-510)	pEC-A-3C-ZTA	6xHis-Z	-	3C	Conti Lab	-
CNOT11 (1-510)	pFastBac1	9xHis-3C	-	3C	Conti Lab	-
CNOT11 (1-510)	pFastBac1	-	TwinStrep	-	this study	95,96
CNOT11 (1-510)	pFastBac1	Twinstrep-3C	-	3C	Conti Lab	-
CNOT11 (1-510)	pLIB	-	TwinStrep	-	this study	99 + 100
BTG2	pEC-A-3C-TRX	6xHis-TrxA	-	3C	Conti Lab	-
TTP (1-326)	pEC-A-3C-GST	6xHis-GST	StrepII	3C	this study	61,42
TTP (1-326)	pEC-A-3C-GST	6xHis-GST	C-tag	3C	this study	125,42

Table 2.4. List of DNA primers used in this study.

Number	Name	5' to 3' Sequence
42	HisGST.FOR	gcggatcccggtccgATGAAACATCACCATCACCATCACAAC
52	pFB1-CNOT7-fw	CCAGGGGCCCGACTCGATGCCAGCGGCAACTGTAGAT
53	pFB1-CNOT7-rev	cagaccgccaccgactgcttaTCATGACTGCTTGTTGGCTTCC
54	pFB3C-CNOT6-fw	ccaggggcccgactcgatgCCCAAAGAAAAATACGAGCCC
55	pFB3C-CNOT6-rev	cagaccgccaccgactgcttaCTACCTCCTGCCAGGAAGGT
56	Fusion-CNOT6-fw	CTGGAAGTTCTGTTCCAGGGGCCCGACATGCCCAAAGAAAAATACGAGCCCCCTGACCCTCGGAG
57	Fusion-CNOT7-rev	GTCGGGCCCCTGGAACAGAACTTCCAGtgactgcttgttggcttcctcttcatatgcat
58	pFB-CNOT1-813-fw	CCAGGGGCCCGACTCGATGGGACTGAATCAGCCTACATTCCAG
60	pFB-CNOT1-1596-rev	CAGACCGCCACCGACTGCTTATTGCTTCATGGGCTGGGC
61	TTP-StrepII-rev	CAGACCGCCACCGACTGCTTATTTTTCGAACTGCGGGTGGCTCCACTCAGAAACAGAGAT
66	pFB-His-3C-C9-fw	CCAGGGGCCCGACTCGATGCACAGCCTGGCGACGG
67	pFB-CNOT9-rev	CAGACCGCCACCGACTGCTTATCACTGAGGGGGCAGGG
79	pFB-LIC-CNOT3-fw	CCAGGGGCCCGACTCGATGGCGGACAAGCGC
80	pFB1-LIC-CNOT3-Ctag-rev	CAGACCGCCACCGACTGCTTAGGCTTCCGGTTCGCTACCCTGGAGGTC
83	LIC-pFB-CNOT3-fw	ccaggggcccgactcgATGGCGGACAAGCGCAAACTCCAAGGTGAGATTGA
85	pFB1-His-3C-CNOT2-fw	ccaggggcccgactcgatgGTGAGGACTGATGGACATAC
86	pFB1-CNOT2-rev	cagaccgccaccgactgcttaTTAGAAGGCTTGCTGAGCAG
95	pFB-LIC-CNOT11-TwStrep-rev	CAGACCGCCACCGACTGCTTATTTCTCGAACTGCGGGTGGCTCCACGCTGAACCTCCC GATCCACCGCCAGAACCTCCACCTTTTTCGAACTGCGGGTGGCTCCAAGCGCTTTTTGACAT
96	LIc-CNOT11-FW	CCAGGGGCCCGACTCGATGCCCGGCGGAGG
99	CNOT11-Twin-BB-BamHI-5	GGGGGGATCCATGCCCGGCGGAGGGGCGAG
100	CNOT11-Twin-BB-PstI-3	CCCCTGCAGTTATTTCTCGAACTGCGGGTGGCTCCACGCTGAACCTCCC GATCCACCGCCAGAACCTCCACCTTTTTCGAACTGCGGGTGGCTCCAAGCGCTTTTTGACATTTTGGTCTC
101	CNOT6-BB-BamHI-5	GGGGGGATCCATGCCCAAAGAAAAATACGA
102	CNOT6-BB-PstI-3	CCCCCTGCAGTTACTACCTCCTGCCAGGAA
103	CNOT7-BB-BamHI-5	GGGGGGATCCATGCCAGCGGCAACTGTAGA
104	CNOT7-BB-Pst1-3	CCCCCTGCAGTTATCATGACTGCTTGTTGG
105	CNOT9-BB-BamHI-5	GGGGGGATCCATGCACAGCCTGGCGACGGC
106	CNOT9-BB-SacI-3	CCCCGAGCTCTCACTGAGGGGGCAGGGGGACCCCGAGCTCTCACTGAGGGGGCAGGGGGA
107	CNOT2-BB-XbaI-5	GGGTCTAGAATGGTGAGGACTGATGGACA
108	CNOT2-BB-HindIII-3	CCCCAAGCTTTTAGAAGGCTTGCTGAGCAG
125	TTP-Ctag-3-lic	CAGACCGCCACCGACTGCTTAGGCTTCCGGTTCGCTACCCTCAGAAACAGAGATGCGATTGAAGAT

RNA

The RNA substrates used in this study were purchased from Ella Biotech GmbH, reconstituted to 100 µM stocks and stored at -20 °C.

Table 2.5. Sequences of RNAs used in this study.

5' Fluorophore	Sequence (5' - 3')	Name
Atto 647N	CAC AUC CAA CUU CUC UAA AU [A]60	R-60A
Atto 550	CAC AUC CAA CUU CUC UAA AU [A]30	R-30A
Atto 550	CAC AUC CAA CUU CUC UAA AU [A]55 GGG AA	R-55A GGG AA
Atto 647N	CAC AUC CAA CUU CUC UAA AU [A]25 GGG AA	R-25A GGG AA
Atto 550	CAC AUC UUA UUU AUU UAA AU [A]30	ARE-30A
Atto 647N	CAC AUC UUA UUU AUU UAA AU [A]25 GGG AA	ARE-25A GGG AA

2.0.4 Polyacrylamide gels

Table 2.6. Polyacrylamide gels.

Type of gel	Composition	Stocksolution	Final concentration
Stacking gel (5 %)	H_20		
	Tris pH 6.8	1 M	150 mM
	Acrylamide/Bisacrylamide (37.5:1)	30 %	5 %
	Sodium dodecyl sulfacte (SDS)	10 %	0.1 %
	Ammonium persulfate (APS)	10 %	0.1 %
	Tetramethylethylenediamine (TEMED)	100 %	0.1 %
Separating gel (12.5 %)	H_20		
	Tris pH 8.8	1.5 M	375 mM
	Acrylamide/Bisacrylamide (37.5:1)	30 %	12.5 %
	SDS	10 %	0.1 %
	APS	10 %	0.1 %
	TEMED	100 %	0.1 %
Urea - polyacrylamide gel 10 %	Urea 1x Trisborate (TBE)	7 M	7 M
	20 % Acrylamide/Bisacrylamide (19:1)/ 7 M Urea/1xTBE	20 %	10 %
	APS	10 %	0.6 %
	TEMED	100 %	0.1 %

2.0.5 Standard buffers and dyes

Table 2.7. Standard buffers and dyes that have been used throughout this study.

Buffer	**Composition**
PBS	137 mM NaCl
	2.7 mM KCl
	10 mM Na_2HPO_4 pH 7.4
	1.76 mM KH_2PO_4 pH 7.4
TBE (10x)	1 M Tris-HCl
	0.89 M boric acid
	20 mM EDTA pH 8.0
SDS-PAGE running buffer	0.25 M Trizma Base
	1.92 M Glycine
	1 % (v/v) SDS
SDS loading buffer (2x)	100 mM Tris pH 6.8
	4 % (v/v) SDS
	0.2 % (v/v) bromphenol blue
	20 % (v/v) glycerol
	10 % β-mercaptoethanol
RNA-loading dye 100 % OFE	0.1 % Orange G
	10 mM EDTA pH 8.0
	98 % Formamide

2.0.6 Cell culture

E. coli strains

Table 2.8. List of *E. coli* strains used in this study, together with their supplier and genotype.

Strain	Genotype	Use	Supplier
BL21(DE3) Gold	F⁻ompT hsdS(r_B^-, m_B^-) dcm^+ Tet^r gal endA Hte	Protein expression	Agilent
BL21(DE3) pLysS	F⁻ompT $hsdS_B$ (r_B^-, m_B^-) gal dcm (DE3) pLysS(Cam^R)	Protein expression	Invitrogen
BL21(DE3) Star pRARE	F⁻ ompT $hsdS_B$ (r_B^-, m_B^-) gal dcm rne131 (DE3)	Protein expression	Stratagene
DH10EMBacY	F⁻ mcrA Δ(mrr-hsdRMS-mcrBC) ϕ(lacZ) ΔM15ΔlacX74 recA1 endA1 araD139 Δ(ara, leu)7697 galU galK λ^- rpsL nupG /BacloxP/ pBADZ-His6Cre/pMON7124	Bacmid preparation	Invitrogen
Omnimax 2 $T1^R$	F' [$proAB^+$ $lacI^q$ lacZΔM15 Tn10(Tetr) Δ(ccdAB)] mcrA Δ(mrr-hsdRMS-mcrBC) Φ80lacZΔM15 Δ(lacZYA-argF) U169 endA1 recA1 supE44 thi-1 gyrA96(Nal^r) relA1 tonA panD	Cloning	Invitrogen
Rosetta	F⁻ ompT hsdSB(rB^- mB^-) gal dcm (DE3) pRARE	Protein expression	Merck
XL1-Blue	recA1 endA1 gyrA96 thi-1 hsdR17 supE44 relA1 lac [F' proAB $lacI^qZ$ΔM15 Tn10(Tet^r)]	Cloning	Agilent

Bacterial cell culture media

The media used for liquid cultures or plates were home-made by staff of the Conti department.

Table 2.9. Media for bacterial cultures.

Medium	Composition
Lysogenic broth (LB) (Bertani, 1951; Miller, 1972)	1 % (w/v) Bacto Tryptone, 1 % (w/v) NaCl, 0.5 % Yeast Extract, pH 7.2
Terrific Broth (TB) (Sambrook & Russell, 2001)	1.2 % (w/v) Bacto Tryptone, 2.4 % (w/v) Yeast Extract, 0.4 % (v/v) glycerol
10X Phosphate Stock for TB	0.17 M KH_2PO_4, 0.72 M $K_2HPO_4 \cdot 3H_2O$
Super optimal broth with catabolite repression (SOC)	2 % (w/v) Bacto Tryptone, 0.5 % (w/v) Yeast Extract, 10 mM NaCl, 1 mM $MgCl_2$, 2.5 mM KCl, 10 mM $MgSO_4$, 0.4 % glucose, pH 7.2

Antibiotics and additives

Table 2.10. Antibiotics and additives to cell culture media used in this study.

Substance	Stock concentration	Final concentration
Ampicillin (in water)	100 mg/mL	100 µg/mL
Chloramphenicol (in ethanol)	34 mg/mL	34 µg/mL
Gentamicin (in water)	7 mg/mL	7 µg/mL
Kanamycin (in water)	50 mg/mL	50 µg/mL
Streptomycin (in water)	50 mg/mL	50 µg/mL
Tetracycline (in water)	10 mg/mL	10 µg/mL
IPTG	1 M	0.1 - 1 mM
X-Gal (in DMSO)	40 mg/mL	100 µg/mL

Insect cell lines

The insect cell stocks were maintained in RTU Sf900 II SFM medium (Gibco, Thermo Fisher Scientific) while large scale expressions were cultured in Sf900 II SFM powder medium.

Table 2.11. List of insect cell lines used in this study.

Strain	Species	Use	Supplier
IPLB-Sf21	*Spodoptera frugiperda*	Virus expression	Thermo Fisher Scientific
BTI-TN-5B1-4 High Five	*Trichoplusia ni*	Protein expression	Invitrogen

2.0.7 Chromatography

Chromatographic methods were carried out using ÄKTAprime plus, ÄKTApurifier or ÄktaMicro chromatography systems (GE Healthcare). All columns used for protein purifications were purchased from GE Healthcare.

2.0.8 Equipment

Table 2.12. List of equipment.

Equipment	**Producer**
NanoDrop (ND-1000) spectrophotometer	PeqLab, Erlangen, Germany
Typhoon^{TM} FL7000 Phoshoimager	GE Healthcare, München
Vitrobot Mark iV	FEI (ThermoFisher Scientific)
CM200-FEG electron microscope	Philips
Titan Krios	FEI (ThermoFisher Scientific)
Talos Arctica	FEI (ThermoFisher Scientific)
Glacios	FEI (ThermoFisher Scientific)
Titan Halo	FEI (ThermoFisher Scientific)
K2 Summit	Gatan, Pleasanton, USA
Falcon 2	FEI (ThermoFisher Scientific)
K3	Gatan, Pleasanton, USA
Falcon 3	FEI (ThermoFisher Scientific)
Mass photometer Two^{MP}	Refeyn, Oxford
GloQube^{TM}plus glow discharge system	Quorum
NanoPhotometer NP80	Implen

2.0.9 Software

Table 2.13. List of software/web servers. The following software was used to process and analyze data.

Software	Supplier/Developer
AlphaFold 2	Jumper *et al.*, 2021
ApE	M. Wayne Davis
cryoSPARC	Punjani *et al.*, 2017
EMAN2	Tang *et al.*, 2007
EPU	FEI (ThermoFisher Scientific)
Fiji/ImageJ	Schindelin *et al.*, 2012
Gautomatch	Zhang software - MRC Laboratory of Molecular Biology
Gctf	Zhang software - MRC Laboratory of Molecular Biology
MotionCor2	Zheng *et al.*, 2017
Expasy ProtParam	https://web.expasy.org/protparam/
PyMOL	Schrödinger, LLC, 2015
RELION	Zivanov *et al.*, 2020
SerialEM	Mastronarde, 2003
UCSF Chimera	Pettersen *et al.*, 2004
UNICORN	GE Healthcare (Cytiva)
UNIPROT	https://www.uniprot.org/
XlinkAnalyzer	Kosinski *et al.*, 2015

Chapter 3

Methods

3.1 DNA methods

Cloning strategies

DNA plasmid constructs for expression in *E. coli* and insect cells were generated using several cloning strategies and vector systems such as conventional restriction cloning, Ligation-independent cloning (LIC) (Aslanidis & De Jong, 1990), and Gibson assembly (Gibson *et al.*, 2009). All steps were carried out at room temperature (RT), unless otherwise indicated. Oligos, DNA constructs and intermediate DNA products were stored at -20 °C.

Polymerase Chain Reactions

Genes or gene fragments were amplified by polymerase chain reaction (PCR) from template plasmids or cDNA, from the MPIB core facility cDNA library. Reactions were performed according to standard protocols using Phusion High-Fidelity PCR Master Mix with HF buffer (Thermo Scientific^{TM}) containing polymerase, polymerase buffer, and dNTPs. The annealing temperature was adjusted according to the melting temperature (T_m) of the respective primer pair ranging between 55 and 65 °C and the extension time was adjusted for the respective construct length with 1 min/kb.

Table 3.1. Standard PCR program.

Cycling step	Temperature	Duration	Cycles
Initial Denaturation	98 °C	30 s	1
Denaturation	98 °C	20 s	
Annealing	T_m °C	30 s	25
Extension	72 °C	1 min/kb	
Final extension	72 °C	5 min	1
Cooling	4 °C	hold	

Table 3.2. Standard PCR reaction.

Component	Amount for 50 µL reaction	Final concentration
Phusion Master Mix	25 µL	1x
Template DNA	x µL	5-15 ng
Forward primer	2.5 µL	0.5 µM
Reverse primer	2.5 µL	0.5 µM
DMSO (optional)	2.5 µL	5 %
H_2O	add to 50 µL	

Agarose gel electrophoresis

PCR products and restriction digests were analyzed by agarose gel electrophoresis. PCR products were mixed with 6x orange loading dye (Thermo Scientific) and then separated on 0.75-1 % (w/v) agarose gels prepared in 0.5 x TBE, containing 2.5 µL/ 50 mL of SYBR™ Safe (Invitrogen). As size fiducial 0.5 µg of 1 kB GeneRuler (Thermo Fisher Scientific) was used. DNA fragments were visualized using a SAFE IMAGER (Invitrogen).

Gel extraction

After agarose gel electrophoresis, the separated DNA bands were excised from the gel and purified using the Wizard SV Gel and PCR Clean-up system (Promega) according the manufacturer's instructions.

Transformation

Heat-shock transformation Chemically competent cells (Omnimax or DH10EM BacY) were thawed on ice. For transformation, 50 µL cells were gently mixed with 1-3 µL of purified vector or cloning reaction and incubated on ice for 10-20 min. The mixture was heat shocked at 42 °C for 45 s and then cooled down on ice for 2 min before adding 300 µL of antibiotic-free SOC medium.

Electroporation 1-2 µL of purified vector or cloning reaction were carefully mixed with 50 µL of electro competent XL1 Blue cells (Cloning) or cells of the respective bacterial expression strain (protein expression) and transferred to chilled electroporation cuvettes. After electroporation with a pulse at 2.5 kV in setting Ec2 of the Bio-Rad Micropulser^{TM}, 300 µL SOC were added, mixed gently, and then transferred to an 1.5 mL Eppendorf tube. For recovery, cells were placed on a shaker for 1 h at 37 °C. After recovery, cells were plated on LB agar plates supplemented with the respective antibiotic and incubated at 37 °C over night (O/N). The next day, individual colonies were picked and used to inoculate mini cultures of 2-5 mL LB medium containing the appropriate antibiotics, which were grown for 8-15 h at 37 °C and 220 rpm. After harvesting bacterial cells by centrifugation for 10 min at 4 °C and 4000 rpm, plasmid DNA was prepared by using the QIAprep Spin Miniprep Kit (Qiagen).

Restriction cloning

Restriction enzyme digestion Before ligation, PCR products and vectors were digested in a 30 µL double digestion reaction, which included 3 µL of an appropriate 10x buffer (e.g. 10x CutSmart(NEB)) and 1 µL of each restriction enzyme, and 2 µg of plasmid DNA or 25 µL of PCR product, made up to 30 µL with water for 1-1.5 h at 37 °C. The digested products were then purified by agarose gel electrophoresis and gel extraction.

Ligation Ligation reactions were performed in 10 µL reactions containing 1 µL T4 DNA ligase (NEB), 2 µL of T4 DNA ligase buffer 5x (NEB), 20 ng of digested and purified vector DNA, and 100 ng of digested and purified insert DNA (1:5 ratio), made up with water to 10 µL and incubated for 30 min to 1 h at RT. 2 µL of the ligation reaction was transformed in competent cells as described above.

LIC cloning

The amplified PCR product was cloned into LIC vectors generated in the Conti department.

Vector processing To linearize the vector, 2 µg were digested with 20 u of ZraI in a 100 µL reaction volume and then purified by agarose gel electrophoresis and gel extraction. The linearized vector was then processed in the following reaction:

Table 3.3. LIC vector processing reaction.

Component	**Amount for 30 µL reaction**	
Linearized vector	450 ng	
T4 DNA polymerase buffer (10x)	3 µL	
dTTP (25 mM)	3 µL	
DTT (100 mM)	1.5 µ	
T4 DNA Polymerase (LIC qualified)	0.6 µL	
H_2O	to 30 µL	incubation for 30 min at RT

After incubation, the enzymes were inactivated by incubation for 20 min at 75 °C.

Insert processing The gel purified PCR product was incubated in the following reaction mix:

Table 3.4. LIC insert processing reaction.

Component	**Amount for 20 µL reaction**	
PCR product	600 ng	
T4 DNA polymerase buffer (10x)	2 µL	
dATP (25 mM)	2 µL	
DTT (100 mM)	1 µ	
T4 DNA Polymerase (LIC qualified)	0.4 µL	
H_2O	to 20 µL	incubation for 30 min at RT

After the reaction, enzymes were inactivated by incubation for 20 min at 75 °C.

Annealing reaction The processed insert (2 µL) and vector (1 µL) were mixed and incubated for 10 min at RT. The reaction was stopped by adding 1 µL of EDTA (25 mM) and further incubation for 10 min. In the last step, 2 µL were transformed into competent *E. coli* cells.

Gibson assembly

To generate a vector containing all constructs for co-expression in insect cells, the biGBac system (Weissmann *et al.*, 2016) was used. Plasmids were generously provided by the group of Jan-Michael Peters, I.M.P., Vienna.

Vector linearization Vectors were linearized prior to Gibson assembly. Each pBIG1 vector was digested in a 50 µL reaction (3.5) at RT O/N. The next day, 2 µL SwaI was added, and after 2 h incubation, the enzyme was inactivated by incubation at 65 °C for 2 h, and the linearized vector was purified using a PCR clean-up kit.

Table 3.5. pBIG1 a-e linearization.

Component	Amount for 50 µL reaction
pBIG1 A-E (∼300 ng/ µL)	30 µL
10x NEB buffer 3.1	5 µL
SwaI (NEB)	1 µL
H_2O	14 µL

The pBIG2 vectors (2ab, 2abc, 2abcd, 2abcde) were linearized with PmeI in a similar reaction (3.6). After incubation O/N at RT, 2 µL PmeI was added and incubated for 2 h. The linearized vectors were then purified using a PCR clean-up kit.

Table 3.6. pBIG2 linearization.

Component	Amount for 50 µL reaction
pBIG2 (~300 ng/ µL)	30 µL
10x CutSmart buffer (NEB)	5 µL
PmeI (NEB)	1 µL
H_2O	14 µL

Cloning of constructs into pLIB In the first step, the constructs were cloned into pLIB vectors by restriction cloning as described above. If the constructs were already cloned in pFastBac vectors, this step could be omitted. The following procedures are taken from Weissmann & Peters, 2018 with minor modifications.

Cloning of pLIB constructs into pBIG1 In the second step, gene expression cassettes (GEC) of up to five pLIB/pFastBac vectors per pBIG1 vector were amplified by PCR with primers containing specific linker sequences for pLIB or pFastBac vectors (designed by Christian Benda, Conti department). The PCR products were purified by agarose gel electrophoresis or PCR clean up. For Gibson assembly, the linearized vector was mixed with the PCR amplified GECs as shown in Table 3.7, then mixed with Gibson assembly master mix and incubated for 1 h at 50 °C in a thermocycler with a preheated lid. After mixing, 2 µL were transformed in a chemically competent *E. coli* strain such as Omnimax as described above and recovered in LB medium at 37 °C for 1 h. Cells were then plated on LB-spectinomycin plates and incubated at 37 °C O/N. The next day, colonies were picked and used to inoculate 5 mL LB-spectinomycin cultures. Plasmid DNA was isolated using a Miniprep kit (Qiagen) and clones were analyzed by restriction digest as described in 3.8, incubated for 2 h at RT, and then analyzed by agarose gel electrophoresis. Positive clones were sent for sequencing with cassette specific primers designed by Yair Gat, Conti department.

Table 3.7. Gibson assembly reaction.

Component	**Amount for 10 µL reaction**
Linearized pBIG1 vector	∼10 fmol
PCR amplified GEC1	20-50 fmol
PCR amplified GEC2	...
H_2O	add up to 10 µL
Gibson Master Mix (2x)	10 µL

Table 3.8. Analysis of 1st Gibson assembly.

Component	**Amount for 10 µL reaction**
SwaI digest	
DNA clone #1	1.2 µL (∼100-500 ng/µL)
NEB buffer 3.1 (10x)	1 µL
SwaI (10 U/ µL)	0.5 µL
H_2O	7.3 µL
PmeI digest	
DNA clone #1	1.2 µL (∼100-500 ng/µL)
NEB CutSmart buffer (10x)	1 µL
PmeI (10 U/ µL)	0.2 µL
H_2O	7.6 µL

Assembly of pBIG2 from pBIG1 To assemble the constructs from pBIG1a and pBIG1b into one pBIG2ab vector, the poly gene cassettes were first released by PmeI digestion for 90 min at 37 °C, followed by a Gibson assembly reaction for 1 h at 50 °in a thermocycler with preheated lid as described in 3.9.

Table 3.9. Gibson assembly into pBIG2ab.

Component	**Amount for 10 µL reaction**	
PmeI digest		
Linearized pBIG2ab vector	33 ng/ µL (∼10 fmol)	
pBIG1a	∼ 50 fmol	
pBIG1b	∼50 fmol	
10x NEB CutSmart buffer	1 µL	
PmeI (10 U/ µL)	1 µL	
H_2O	add to 10 µL	90 min at 37 °C
Gibson assembly		
Gibson assembly master mix	10 µL	60 min at 50 °C

After mixing, 2 µL were transformed in a chemically competent *E. coli* strain such as Omnimax and recovered in SOC medium at 37 °C for 1 h. Cells were then plated on LB-chloramphenicol plates and incubated at 37 °C O/N. The next day, colonies were picked and used to inoculate 5 mL LB-chloramphenicol cultures. After ∼16 h at 37 °C, plasmid DNA was isolated using a Miniprep kit and clones were analyzed by restriction digest as described in 3.10 followed by analysis on 0.8 % agarose gels. Positive clones were sent for sequencing with gene specific primers.

Table 3.10. Analysis of 2nd Gibson assembly.

Component	**Amount for 10 µL reaction**	
SwaI digest		
2ab clone #1	2.5 µL (∼100-500 ng/µL)	
NEB buffer 3.1 (10x)	1 µL	
SwaI (10 U/ µL)	1 µL	
H_2O	5.5 µL	2 h at RT
PacI digest		
2ab clone #1	0.8 µL	
NEB CutSmart buffer (10x)	1 µL	
PacI (10 U/ µL)	0.5 µL	
H_2O	7.7 µL	2 h at 37 °C

Large-scale protein expression in bacterial cell culture

After cloning, plasmid DNA was transformed in electro-competent *E. coli* strains as transcribed above and plated on LB-agar plates supplemented with chloramphenicol and the respective plasmid selection antibiotic. After incubation at O/N at 37 °C, colonies were used to inoculate a pre-culture of 100 mL of LB medium supplemented with the respective antibiotics. The pre-culture was grown for ∼18 h at 37 °C and 220 rpm and used to inoculate 6 L of TB media grown in Tunair flasks with 1 L/flask or 250 mL/flasks in Erlenmeyer flasks at 37 °C and 190-220 rpm. Cultures were grown to OD_{600}1-1.5, before cooling to 18 °C. Protein expression was induced by the addition of 0.1-0.4 mM IPTG and cells were grown O/N.

3.2 Insect cell methods

Generation of recombinant Baculoviruses

For recombinant expression of proteins in insect cells, a recombinant baculovirus was generated by Tn7 transposition of gene cassettes of vectors pLIB, pBIG1, pBIG2 or pFastBac into the genome of EmBacY baculovirus. Chemically competent DH10EmBacY cells were mixed with 1-2 µL of the respective DNA and incubated on ice for 45 min before heat shock for 45 s at 42 °C. After 2 min cooling on ice, 300 µL of SOC medium was added and the cells were shaken at 37 °C for 1-6 h for recovery. The recovered cells were plated on LB-agar plates for blue-white selection (3.11) and incubated at 37 °C for 24-36 h. White colonies were picked and to be certain, streaked again on a blue-white selection plate, and in parallel used to inoculate a 2 mL culture with LB-medium supplemented with kanamycin (50 µg/mL) and gentamicin (7 µg/mL). After incubation at 37 °C for 16 h bacmid DNA was isolated.

Table 3.11. Blue-white selection LB-agar plates.

Component	Final concentration
Kanamycin	50 µg/mL
Gentamycin	7 µg/mL
Tetracycline	10 µg/mL
X-Gal	100 µg/mL
IPTG	40 µg/mL

Bacmid DNA isolation

Bacmid DNA was isolated by alkaline lysis using buffers from the QIAprep Spin Miniprep kit (Qiagen). After harvesting the cells by centrifugation, the cell pellet was resuspended in 250 µL P1 resuspension buffer (50 mM Tris at pH 8.0, 10 mM EDTA, 100 µg/mL

RNase A) and transferred into a microcentrifuge tube. After addition of 250 µL of P2 lysis buffer (200 mM NaOH, 1 % SDS), the tube was inverted several times to mix the solutions properly. To neutralize the mixture, 350 µL of N3 buffer (3 M KOAc at pH 5.5) was added, mixed by inverting the tube and the precipitate was pelleted by centrifugation at 16.100x g for 10 min. The supernatant was transferred into a fresh 2 mL tube and 800 µL of isopropanol was added, thoroughly mixed and placed on ice for 10 min to precipitate the DNA. The precipitated DNA was pelleted by centrifugation at 16.100x g for 15 min. The supernatant was carefully removed without disturbing the DNA pellet, 750 µL of 70 % ethanol added, the pellet was washed by inverting the tube. To prevent any contaminations, further steps were carried out in a sterile environment. After centrifugation at 16.100x g for 5 min, as much supernatant was removed as possible, and the pellet was air-dried in a sterile environment for 5 min. The DNA pellet was then dissolved in 40 µL of sterilized water by tapping the bottom of the centrifuge tube.

Insect cell culture

Sf21 and HighFive (Hi5) cells were constantly maintained in liquid culture. Cell stocks were cultured in ready-to use Sf900 II SFM medium (Thermo Fisher Scientific) in 300 mL culture volumes in 3 L Fernbach plastic flasks in a climate-controlled room at 26 °C and 85 rpm. Cells were grown at densities of 0.5 - 6 $\cdot$ 10^6 cells/mL with viability over 95 % and diameters ranging from 16-17 µm (Sf21) to 18-19 µm (Hi5) and split every 2-3 days as needed. Culture density, viability, and diameter were monitored using a Vi-cell XR cell viability analyzer (Beckman Coulter). Sf21 cells were mainly used for transfection and virus amplification, while Hi5 cells were used for large-scale protein expression. Steps that required open cultures were performed in a sterile environment under a UV-sterilized laminar flow hood.

Transfection and virus production

Sf21 cells were diluted to $0.5 \cdot 10^6$ cells/mL and 2 mL cells/well were pipetted into a 6-well tissue culture plate and allowed to rest for 30 min. In 1.5 mL Eppendorf tubes, 5 µL of FuGENE HD transfection reagent (Promega) was gently mixed with 200 µL medium and 2 µg of the respective Bacmid DNA and incubated for 15 min. The bacmid mixtures were added dropwise to the wells. The plate was then sealed and incubated at 26 °C for 4-5 days. Transfection rate was monitored with a fluorescence microscope. The virus-containing supernatant (P1 virus) was collected in 2 mL Eppendorf tubes and stored at 4 °C, protected from light.

Virus propagation In a 3 L Erlenmeyer flask, 10-50 µL of P1 virus was added to 250 mL of freshly diluted Sf21 cells at $0.5 \cdot 10^6$ cells/mL and incubated at 26 °C at 85 rpm for 3-5 days. Cell density, viability and diameters were monitored. Once the cells doubled and showed increased cell diameters (usually after 3 days), cells were split to $1 \cdot 10^6$ cells/mL and further incubated. Normally, 2 days after proliferation arrest, when viability had decreased to 80-90 % and diameters had increased by 3-5 µm compared with control cells, the supernatant was collected and stored as P2 virus at 4 °C, protected from light.

Expression test pull-downs To test protein expression and solubility of the constructs as well as optimal virus concentration, His and TwinStrep tag pull-downs of small scale (25 mL) expressions were performed. In 100 mL Erlenmeyer flasks, 25 mL Hi5 cells at $1 \cdot 10^6$ cells/mL were infected with respectively 50, 125, or 250 µL (0.2, 0.5, 1 % (v/v)) of P2 virus and incubated for 68-72 h at 26 °C and 85 rpm. After collecting the cells via centrifugation for 10 min at 800x g, the cell pellets were flash-frozen in liquid nitrogen. For cell lysis, the pellets were thawed on ice in 2 mL lysis buffer (50 mM Na-Phosphate at pH 7.5, 250 mM NaCl, 30 mM imidazole and 0.01 % (v/v) Tween-20, 1:300 AEBSF (100 mM), 1:1000 DNase

(1 mg/mL) and 1:10000 Benzonase). The pull-downs were performed with the KingFisher (Thermo Fisher Scientific) pull-down robot. For this, 1 mL of cell-lysate per 30 µL of magnetic bead slurry (His-pull-down: PureProteom Nickel Magnetic beads (Merck), Strep-pull-down: Strep-Tactin(XT) beads (iba lifesciences)) was used. The protocol included three wash steps in 600 and 2x 300 µL wash buffer (50 mM Na-Phosphate at pH 7.5, 250 mM NaCl, 30 mM imidazole and 0.01 % (v/v) Tween-20). The samples were eluted in 75 µL of the respective elution buffer (His-elution buffer: 50 mM Na-Phosphate at pH 7.5, 250 mM NaCl, 300 mM imidazole; Strep-elution buffer: 1x XT elution buffer: 100 mM Tris-Cl at pH 8.0, 150 mM NaCl, 1 mM EDTA, 500 mM biotin). Samples of pellet, lysate and elution fractions were analyzed by SDS-PAGE analysis.

Large scale expression in Hi5 cells Hi5 cells were diluted to $1 \cdot 10^6$ cells/mL with SF900-II medium (prepared from powder) in 500-1000 mL per 3 L flask. Cells were infected with 1 % (v/v) of P2 virus and grown for 68-72 h at 26 °C and 85 rpm.

3.3 Protein methods

SDS-PAGE

Protein expression and the individual steps of protein purification were analyzed by SDS-PAGE using homemade polyacrylamide gels. The respective protein samples were mixed with 2x SDS-loading dye, and boiled for 2 min at 95 °C prior to loading on 10-12.5 % polyacrylamide gels together with 2 µL of PageRuler Unstained Broad Range Protein Ladder (Thermo Fisher Scientific). Electrophoresis was carried out in a Mini-Protean Tetra vertical Electrophoresis Cell (Bio-Rad) by applying a voltage of 150-270 V. Cross-linked samples were analyzed on pre-cast gradient NuPAGE^{TM} 4-12 % Bis-Tris Protein gels (Invitrogen) in 1x MOPS buffer (50 mM MOPS, 50 mM Tris Base, 0.1 % SDS, 1 mM EDTA, pH 7.7) in

XCell SureLock Mini-Cell chambers (Invitrogen). Gels were stained by Coomassie staining solution (10 % acetic acid, 20 % EtOH, 100 mL Coomassie), InstantBlue (expedeon) or Der blaue Jonas - Single-Step Coomassie Blue protein gel dye (GRP).

Protein purifications

All protein handling steps were carried out on ice or in the cold room at 4 °C.

Cell lysis

Bacterial cell pellets were resuspended in construct-specific lysis buffer, containing additional 1:1000 DNase1 (1 mg/mL), 1:300 4-(2-aminoethyl)benzenesulfonyl fluoride hydrochloride (AEBSF) (100 mM) and 1-5 mM β–mercaptoethanol (BME), optionally 1 tablet of EDTA-free cOmplete Protease Inhibitor Cocktail (PIC) (Roche). Lysis was performed by sonication (Bandeline Electronics) with an TT13 probe for 10-15 min and an amplitude of 40 %, and a pulse duration of 0.5 s on, 0.5 s off.
Insect cell pellets were flash-frozen in liquid N_2 after harvest, then thawed on ice and resuspended in lysis buffer, containing additional 1:1000 DNase1 (1 mg/mL), 1:300 AEBSF (100 mM) and optionally 1 tablet of PIC. Lysis was performed using a Dounce homogenizer or by resuspension in buffer and incubation on ice. The lysate was cleared in two centrifugation steps. After the first centrifugation for 10 min at 2000x g, 1:10000 Benzonase was added to the supernatant.

Protein purifications from *E. coli* expressions

Purification of CNOT1-N:CNOT9, CNOT9

CNOT1-N (1-1596) was cloned with an N-terminal His-TrxA-tag (6x Histidine-thioredoxin) cleavable with HRV 3C protease (3C protease). Full-length CNOT9 was cloned with an N-

terminal His-SUMO-tag (6x Histidine-Small Ubiquitin-like Modifier) cleavable by SUMO-specific protease SENP2. For the subcomplex CNOT1-N:CNOT9, both were co-expressed recombinantly in *E. coli* BL21 Star pRARE (Stratagene) in TB medium at 18 °C O/N. Cells were resuspended in lysis buffer (50 mM NaH_2PO_4, 350 mM NaCl, 30 mM imidazole, pH 7.4) and lysed by sonication. The lysate was cleared by centrifugation for 60 min at 75.000 g and 4 °C. After filtration, the proteins were isolated by binding to a High-performance (HP) HisTrap immobilized metal affinity chromatography (IMAC) column. The column was washed in three steps: 1st step: 10 column volumes (CV) of wash buffer (50 mM NaH_2PO_4, 350 mM NaCl, 30 mM imidazole, pH 7.4), 2nd step: 15 CV of ATP-containing buffer (50 mM NaH_2PO_4, 350 mM NaCl, 30 mM imidazole, pH 7.4, 10 mM $MgSO_4$, 50 mM KCl, 2 mM ATP) to remove chaperones and last step: 20 CV of the first wash buffer. The proteins were then eluted by a linear gradient of elution buffer (50 mM NaH_2PO_4, 150 mM NaCl, 300 mM imidazole, pH 7.4). The elution fractions were pooled and diluted to reach a salt concentration of 100 mM NaCl and then applied to a Heparin column. After washing with a buffer containing 20 mM Tris-HCl and 100 mM NaCl, the proteins were eluted by a linear gradient to the same buffer containing 1 M NaCl. Both tags were cleaved by adding SUMO-SENP2 and 3C proteases during dialysis against a buffer containing 20 mM Tris-HCl, 250 mM NaCl and 2 mM dithiothreitol (DTT) at pH 7.4. Cleaved tags and proteases were removed in a reverse affinity chromatography step, the flow-through was concentrated and proteins further purified by size-exclusion chromatography (SEC) over a HiLoad 16/600 Superdex 200 column in a buffer containing 20 mM Tris-HCl, 250 mM NaCl and 2 mM DTT at pH 7.4. The eluted complex was concentrated, flash-frozen and stored at -80 °C. For purification of CNOT9 only, it was expressed individually and purified following the same protocol by Marc Baumgärtner, Conti department, MPIB.

Purification of CNOT1-C (813-1596) and CNOT9

CNOT1-C (813-1596) was cloned with an N-terminal His-GST-tag (6xHis-Glutathione-S-Transferase) cleavable with 3C protease. Full-length CNOT9 was cloned with an N-terminal His-SUMO-tag cleavable by SENP2. Both were co-expressed recombinantly in *E. coli* BL21 Star pRARE (Stratagene) in TB medium at 18 °C O/N. Cells were resuspended in lysis buffer (50 mM NaH_2PO_4, 350 mM NaCl, 30 mM imidazole, pH 7.4) and lysed by sonication. The cleared and filtered lysate was applied to a 5 mL HisTrap. After a four-step wash comprising 1st 10 CV of wash buffer (50 mM NaH_2PO_4, 350 mM NaCl, 30 mM imidazole, pH 7.4), 2nd 20 CV of a high salt buffer (50 mM NaH_2PO_4, 1000 mM NaCl, 30 mM imidazole, pH 6.5), 3rd 50 CV of ATP-containing buffer (50 mM NaH_2PO_4, 150 mM NaCl, 30 mM imidazole, pH 7.4, 10 mM $MgSO_4$, 50 mM KCl, 2 mM ATP) to remove chaperones and last 10 CV of wash buffer, both proteins were eluted by a linear gradient of elution buffer (50 mM NaH_2PO_4, 150 mM NaCl, 300 mM imidazole, pH 7.4). The elution fractions were pooled and diluted to reach a salt concentration of 100 mM NaCl and applied to a Heparin column. After washing with a buffer containing 20 mM Tris-HCl at pH 7.4 and 100 mM NaCl, the proteins were eluted by a linear gradient to the same buffer containing 1 M NaCl. Both tags were cleaved by adding 3C and SENP2 proteases O/N on ice. After concentration, the CNOT1-C – CNOT9 heterodimer was further purified by on a HiLoad 16/600 Superdex 200 column in a buffer containing 20 mM Tris-HCl at pH 7.4, 150 mM NaCl, and 2 mM DTT. The eluted complex was concentrated, 20 % glycerol (v/v) added, flash-frozen and stored at -80 °C.

Purification of CNOT10:CNOT11

CNOT10 (1-714 Δ492-504) was cloned with an N-terminal His-TrxA-tag cleavable with 3C protease. CNOT11 (6-510) was cloned with an N-terminal His-Z-tag cleavable by 3C protease. Both were co-expressed recombinantly in *E. coli* BL21 Star pRARE in TB

medium at 18 °C O/N. Cells were resuspended in lysis buffer (50 mM NaH_2PO_4, 350 mM NaCl, 30 mM imidazole, pH 7.4) and lysed by sonication. The cleared lysate was applied to a 5 mL HisTrap column. After a three step wash: 1st step: 20 CV of wash buffer (50 mM NaH_2PO_4, 350 mM NaCl, 30 mM imidazole, pH 7.4), 2nd step: 20 CV of ATP-containing buffer (50 mM NaH_2PO_4, 150 mM NaCl, 30 mM imidazole, pH 7.4, 10 mM $MgSO_4$, 50 mM KCl, 2 mM ATP) to remove chaperones and last again 20 CV of wash buffer, proteins were eluted by a linear gradient of elution buffer (50 mM NaH_2PO_4, 150 mM NaCl, 300 mM imidazole, pH 7.4). The elution fractions were pooled and diluted to reach a salt concentration of 100 mM NaCl and applied to a Heparin column. After washing with a buffer containing 20 mM Tris-HCl and 100 mM NaCl, the proteins were eluted by a linear gradient to the same buffer containing 1 M NaCl. Both tags were cleaved by adding 3C protease O/N on ice. After concentration, the CNOT10:CNOT11 complex was further purified by SEC on a HiLoad 16/600 Superdex 200 column in a buffer containing 20 mM Tris-HCl, 250 mM NaCl, and 2 mM DTT at pH 7.4. The eluted complex was concentrated, 20 % glycerol added, flash-frozen, and stored at -80 °C.

Purification of CNOT6:CNOT7:BTG2

CNOT6 was cloned full-length with an N-terminal His-TrxA-tag cleavable with 3C protease. CNOT7 was cloned full-length with an N-terminal His-SUMO-tag cleavable by SENP2. BTG2 was cloned full-length with an N-terminal His-TrxA-tag cleavable with 3C protease. All three proteins were co-expressed recombinantly in *E. coli* Rosetta in TB medium at 18 °C O/N. The cell pellet was resuspended in lysis buffer (50 mM NaH_2PO_4, 500 mM NaCl, 30 mM imidazole, pH 7.4) and lysed by sonication. The lysate was cleared by centrifugation for 35 min at 75.000 g and 10 °C. After filtration, the cleared lysate was loaded on a 5 mL HisTrap column. After two washing steps: 1st step: 20 CV of wash buffer (50 mM NaH_2PO_4, 500 mM NaCl, 30 mM imidazole, pH 7.4), 2nd step: 20 CV

of wash buffer containing 350 mM NaCl instead of 500 mM, proteins were eluted by a linear gradient of elution buffer (50 mM NaH_2PO_4, 150 mM NaCl, 300 mM imidazole, pH 7.4). All tags were cleaved by adding 3C protease and SENP2 during dialysis against a buffer containing 20 mM Tris-HCl, 150 mM NaCl, 25 mM imidazole, and 2 mM BME at pH 7.4. Cleaved tags and proteases were removed in a reverse affinity chromatography step, and the flow-through subsequently applied to a HiTrapQ column equilibrated in a buffer containing 20 mM Tris-HCl at pH 7.4, 100 mM NaCl, and 2 mM DTT. The trimeric CNOT6:CNOT7:BTG2 complex was eluted by a linear gradient to the same buffer supplemented with 1 M NaCl. The elution fractions were pooled, concentrated, flash-frozen, and stored at -80 °C.

Purification of His-GST-TTP-StrepII

Full-length TTP was cloned with an N-terminal His-GST-tag (cleavable by 3C protease) and a C-terminal StrepII-tag. The protein was expressed in Rosetta in TB medium at 28 °C O/N. The frozen cell pellet was resuspended in lysis buffer (50 mM Tris-HCl pH 7.4, 500 mM NaCl, 1 PIC) and lysed by sonication. The cleared lysate was loaded on a 5 mL StrepTactin column and after four wash steps: 1st step: 20 CV of 50 mM Tris-HCl pH 7.4, 500 mM NaCl, 2nd step: 20 CV of high salt buffer (50 mM Tris-HCl pH 7.4, 1000 mM NaCl), 3rd step: 50 CV of ATP-containing buffer (50 mM Tris-HCl pH 7.4, 150 mM NaCl, 10 mM $MgSO_4$, 50 mM KCl, 2 mM ATP) followed by 20 CV of 50 mM Tris-HCl at pH 7.4 and 150 mM NaCl, the protein was eluted in two elution steps, each with elution buffer (50 mM Tris-HCl pH 7.4, 150 mM NaCl, 2.5 mM Desthiobiotin) and 10 min incubation in between. Depending on the following experiment TTP was either aliquoted, flash-frozen and stored at -80 °C or for further purification the eluted fractions pooled and diluted to reach a salt concentration of 100 mM NaCl and then applied to a Heparin column. After washing with a buffer containing 20 mM Tris-HCl, 100 mM NaCl, pH 7.4, the protein was

eluted by a linear gradient to the same buffer containing 1 M NaCl.

Purification of His-GST-TTP-C-tag

Full-length TTP was cloned with an N-terminal His-GST-tag (cleavable by HRV 3C protease) and a C-terminal C-tag. The protein was expressed in Rosetta in TB medium at 18 °C O/N. The frozen cell pellet was resuspended in lysis buffer (50 mM NaH_2PO_4, 350 mM NaCl, 20 mM imidazole, pH 7.4, 1 tablet of PIC, 1 µL of benzonase) and lysed by sonication. The cleared and filtered lysate was loaded on a 5 mL HisTrap column and after four wash steps (1^{st} step: 20 CV of 50 mM NaH_2PO_4, 350 mM NaCl, 20 mM imidazole, pH 7.4, 2^{nd} step: 20 CV of high salt buffer (50 mM NaH_2PO_4, 1000 mM NaCl, 20 mM imidazole, pH 6.5), 3^{rd} 50 CV of ATP-containing buffer (50 mM NaH_2PO_4, 150 mM NaCl, 20 mM imidazole, pH 7.4, 10 mM $MgSO_4$, 50 mM KCl, 2 mM ATP) followed by 20 CV of 50 mM NaH_2PO_4, 350 mM NaCl, 20 mM imidazole, pH 7.4, the protein was eluted by a linear gradient of elution buffer (50 mM NaH_2PO_4, 150 mM NaCl, 300 mM imidazole, pH 7.4). For further purification the eluted fractions were pooled and diluted to reach a salt concentration of 100 mM NaCl and applied to a Heparin column. After washing with a buffer containing 20 mM Tris-HCl at pH 7.4 and 100 mM NaCl, the protein was eluted by a linear gradient to the same buffer containing 1 M NaCl. The peak was pooled in a 50 mL falcon and for cleavage of the N-terminal His-GST-tag 3C protease was added and incubated for 1 h on ice. For the following C-tag pull down, pre-washed CaptureSelect™ C-tag affinity matrix (Thermo Scientific) was added and incubated for 1 h at 4 °C. The matrix was collected by a centrifugation at 800 g and the supernatant up to 1 mL removed. The suspension was then transferred to a lobind 1.5 mL Eppendorf tube. After four washing steps with 1x Phosphate buffered saline (PBS), TTP was eluted with a buffer containing 1xPBS and 2 mM SEPEA-peptide (MPIB core facility) in two steps with 15 min incubation in between.

Protein purifications from insect cells

Purification of full-length His-TEV-CNOT1, CNOT2, CNOT3

The full-length version of CNOT1-isoform2 was cloned into a pFastBacHTA vector with an N-terminal 6xHis tag, with a Tobacco Etch virus (TEV) cleavage site and as well as a construct with an additional C-terminal MBP tag (3C cleavable). It was co-expressed with the full-length versions of CNOT3 and CNOT2 in Hi5 insect cells. CNOT3 was cloned with an N-terminal 6xHis tag and a C-terminal C-tag into pFastBac1 and CNOT2 was cloned with an N-terminal 6xHis tag. The N-terminal His tags of CNOT2 and CNOT3 were cleavable with 3C protease. The pellet was resuspended in a buffer containing 20 mM HEPES at pH 7.5, 350 mM NaCl, 30 mM imidazole, 5 mM BME, 10 % glycerol (v/v), and 1 PIC tablet and cleared by centrifugation. The cleared lysate was then incubated with TALON Metal Affinity resin (Cytiva) O/N at 4 °C. After washing with 20 mM HEPES at pH 7.5, 350 mM NaCl, 30 mM imidazole, 5 mM BME, the proteins were eluted in the same buffer containing 400 mM of imidazole. The proteins were either directly used for complex reconstitutions or aliquoted, flash-frozen and stored at -80 °C. All purifications of the subcomplex His-TEV-CNOT1/MBP, CNOT2, CNOT3 were carried out by Judith Ebert, Conti department, MPIB.

Purification of CNOT6:CNOT7 expressed as fusion construct

A His-3C-CNOT7-3C-CNOT6 fusion construct was cloned in a pFastBac vector. The N-terminal 6xHis tag and the region between the two proteins were cleavable by 3C protease. The fusion construct was expressed recombinantly in Hi5 insect cells in powder medium at 26 °C for 72 h. The cells were harvested by centrifugation and the pellet frozen in liquid N_2 and stored at -20 °C. The pellet was thawed on ice and resuspended in chilled lysis buffer (25 mM NaH_2PO_4, 250 mM NaCl, 15 mM imidazole, pH 7.4). Nuclei and cell debris were

removed by two subsequent centrifugation steps (10 min at 4000 rpm, 1 h at 75.000 g). After filtration, the cleared lysate was loaded on a 5 mL HisTrap column. After a wash with 20 CV of wash buffer (50 mM NaH_2PO_4, 350 mM NaCl, 30 mM imidazole, pH 7.4), the fusion protein was eluted by a linear gradient of elution buffer (50 mM NaH_2PO_4, 150 mM NaCl, 300 mM imidazole, pH 7.4). The elution fractions were pooled and diluted to reach a salt concentration of 100 mM NaCl and applied to a Heparin column. The flow-through was collected and the N-terminal His-tag as well as the fusion site were cleaved by adding 3C protease O/N on ice. After concentration, the CNOT6:CNOT7 hetero dimer was further purified by on a HiLoad 16/600 Superdex 200 column in a buffer containing 20 mM Tris-HCl at pH 7.4, 250 mM NaCl, and 2 mM DTT. The eluted complex was pooled, 20 % glycerol added, aliquoted, flash-frozen and stored at -80 °C. The purification of active site mutants was carried out in the same way.

Purification of CNOT6:CNOT7 co-expressed

CNOT7 and CNOT6 were cloned as His-3C-CNOT7 and His-3C-CNOT6 constructs in pFastBac1 vectors. The N-terminal 6xHis-tags were cleavable by 3C protease. Both proteins were co-expressed recombinantly in Hi5 insect cells in powder medium at 26 °C for 72 h. The cells were harvested by centrifugation and the pellet frozen in liquid N_2 and stored at -20 °C. The pellet was resuspended in chilled lysis buffer (25 mM NaH_2PO_4, 250 mM NaCl, 15 mM imidazole, pH 7.4) and cells lysed by the Dounce homogenizer. Nuclei and cell debris were removed by two subsequent centrifugation steps (10 min at 4000 rpm, 1 h at 75.000 g). After filtration, the cleared lysate was loaded on a 5 mL HisTrap column. After a wash with 20 CV of wash buffer (50 mM NaH_2PO_4, 350 mM NaCl, 30 mM imidazole, pH 7.4), followed by 20 CV of high salt buffer (50 mM NaH_2PO_4, 1000 mM NaCl, 20 mM imidazole, pH 6.5), the proteins were eluted by a linear gradient of elution buffer (50 mM NaH_2PO_4, 150 mM NaCl, 300 mM imidazole, pH 7.4). The elu-

tion fractions were pooled and diluted to reach a salt concentration of 100 mM NaCl and applied to a Heparin column. The flow-through was collected and after concentration, the CNOT6:CNOT7 hetero dimer was further purified by on a HiLoad 16/600 Superdex 200 column in a buffer containing 20 mM Tris-HCl at pH 7.4, 250 mM NaCl, and 2 mM DTT. The eluted complex was pooled, 20 % glycerol added, aliquoted, flash-frozen and stored at -80 °C. The purification of active site mutations in CNOT6 (E240A) and CNOT7(D40A, E42A) was carried out accordingly.

Purification of full Ccr4-Not co-expressed

For co-expression of all subunits of the Ccr4-Not complex, CNOT1 was cloned with an N-terminal His-TEV-tag (cleavable by TEV protease), CNOT3 with a C-terminal C-tag, CNOT2, and CNOT9 were cloned into a pBIG1A vector. CNOT11 with a C-terminal TwinStrep-tag, CNOT6, CNOT7, and CNOT10 were cloned into the vector pBIG1B. Both cassettes were then combined by Gibson assembly into one pBIG2AB vector. The complex was expressed recombinantly in Hi5 insect cells in powder medium at 26 °C for 72 h. Cells were harvested by centrifugation and the pellet frozen in liquid N_2 and stored at -20 °C. The pellet was resuspended in chilled lysis buffer (50 mM Tris-HCl at pH 7.4, 150 mM NaCl) and cells lysed using a Dounce homogenizer. Nuclei were removed by a 10 min centrifugation step at 4000 rpm. After the addition of 1 µL/50 mL of benzonase to the supernatant, the lysate was further cleared by centrifugation for 1 h at 75.000 g. After filtration, the cleared lysate was loaded on a 5 mL StrepTactin column. After a wash with 10 CV of wash buffer (50 mM Tris-HCl at pH 7.4, 150 mM NaCl), followed by 20 CV of high salt buffer (50 mM Tris-HCl at pH 7.4, 1000 mM NaCl), and 10 CV of the first wash buffer, the complex was eluted in two elution steps, each with elution buffer (50 mM Tris-HCl pH 7.4 or HEPES-NaOH at pH 7.4, 150 mM NaCl, 2.5 mM Desthiobiotin) and 15 min incubation in between. The elution fractions were pooled, 5 % glycerol added, aliquoted,

flash-frozen and stored at -80 °C. The complex was further purified over SEC or by a C-tag pull-down. In the case of SEC, one aliquot was thawed and then applied to a Superose 6 Increase 3.2/300 column in a buffer containing 20 mM HEPES-NaOH pH 7.4, 150 mM NaCl, and 2 mM DTT. The complex was directly used for negative staining and cryo electron microscopy. C-tag pull-downs were performed in 1x PBS or a buffer containing 20 mM HEPES-NaOH at pH 7.4 and 150 mM NaCl. Pre-washed CaptureSelect^{TM} C-tag affinity matrix (Thermo Scientific) was added to a thawed aliquot of Strep-Elution and incubated for 1 h at 4 °C. The matrix was collected by a centrifugation at 800 g and the supernatant up to 1 mL removed. The suspension was then transferred to a lobind 1.5 mL Eppendorf tube. After four washing steps with 1x PBS or 20 mM HEPES-NaOH at pH 7.4 and 150 mM NaCl, the complex was eluted with a buffer containing 1xPBS and 2 mM SEPEA-peptide (MPIB core facility) or 20 mM HEPES-NaOH at pH 7.4, 150 mM NaCl, and 2 mM SEPEA peptide or by high salt in a buffer containing 20 mM HEPES-NaOH at pH 7.4, 1200 mM NaCl in two steps with 15 min incubation in between. The complex was either aliquoted, flash-frozen, and stored at -80 °C or directly used for further experiments. The purification of the Ccr4-Not complex with active site mutations in proteins CNOT6 (E240A) and CNOT7(D40A, E42A) was carried out accordingly.

3.4 Reconstitutions of complexes

Tetrameric Ccr4-Not$_{CORE}$ complex

For reconstitution of the tetrameric Ccr4-Not$_{CORE}$ complex, the previously in *E. coli* and insect cells expressed and purified CNOT1-C:CNOT9, and CNOT6:CNOT7 subcomplexes were mixed in a 1:1.1 molar ratio. In case of cross-linking the mixture was diluted with gel filtration buffer to a concentration of 0.3 mg/mL and bis(sulfosuccinimidyl)suberate (BS^3) was added to a final concentration of 0.7 mM. After 30 min incubation at 26 °C, the

reaction was quenched by the addition of 5 mM ammonium bicarbonate. The sample was concentrated and the excess of subcomplexes was removed by SEC on a Superose 6 Increase 3.2/300 column in a buffer containing 20 mM HEPES-NaOH at pH 7.4, 125 mM NaCl, and 2 mM DTT. The complex was directly used for negative staining and cryo electron microscopy.

Hexameric Ccr4-Not$_{\Delta C}$ complex

For reconstitution of a hexameric Ccr4-Not$_{\Delta C}$ complex with BTG2, the previously in *E. coli* expressed and purified CNOT1-N:CNOT9, CNOT10:CNOT11 and CNOT6:CNOT7:BTG2 subcomplexes were mixed in a 1:1.2:1.2 or 1:1.1:1.1 molar ratio, concentrated and for separation of excess by SEC on a Superose 6 Increase 3.2/300 column in a buffer containing 20 mM Tris-HCl pH 7.4 and 125 mM NaCl or 20 mM HEPES-NaOH pH 7.4, 125 mM NaCl, and 2 mM DTT. The complex was directly used for negative staining and cryo electron microscopy

Full Ccr4-Not complex

For reconstitution of the full Ccr4-Not complex, the previously in *E. coli* and insect cells expressed and purified subcomplexes CNOT1:CNOT2:CNOT3, CNOT10:CNOT11, CNOT6:CNOT7, and CNOT9 were mixed in a 1:1.1:1.1:1.1 molar ratio, concentrated in an Amicon Ultra 0.5 mL centrifugal filter (Merck) with MWCO of 100.00 kDa, and subjected to SEC on a Superose 6 Increase 3.2/300 column in a buffer containing 2x PBS and 0.5 mM DTT.

Reconstitution by gradient ultra-centrifugation

A gradient station/fraction collector (BioComp Instruments) was used to prepare sucrose density gradients and later collect the fractions. For sucrose gradient preparation, two buffer solutions (usually in 1xPBS), a light one containing 10-15 % sucrose (w/v) and a heavy one containing 25-30 % sucrose (w/v), were prepared. In the case of GraFix, 0.03-0.1 % (v/v) glutaraldehyde was added to the heavy solution and quenched with 20 mM Tris-HCl after fractionation. Gradients were prepared by half-filling the SETON centrifugation tube with the light solution and then underlaying it with the heavy solution. Gradient mixing was performed by the gradient station with gradient-specific settings. The Ccr4-Not complex was mixed from purified subcomplexes as described above (3.4), and up to 200 µL of the concentrated complex was added to 12 mL centrifugation tubes (SETON) on the gradient before centrifugation. Density gradient centrifugations were performed using a SW40 rotor (Beckman Coulter) for 16-18 h at 35,000x g at 4 °C. For the Ccr4-Not:TTP complex, all subcomplexes were mixed as described above (3.4), concentrated, and added to 4 mL centrifugation tubes. Centrifugation was performed using a SW60Ti rotor for 18 h at 33,000x g. After centrifugation, gradients were fractionated into 400 µL (or 200 µL) fractions using a fraction collector (Bio-rad) in combination with the gradient station.

Reconstitution of Ccr4-Not:TTP

SEC For reconstitutions of Ccr4-Not:TTP, the previously in *E. coli* and insect cells expressed and purified subcomplexes CNOT1:CNOT2:CNOT3, CNOT10:CNOT11, CNOT9, and CNOT6:CNOT7 were mixed in a 1:2:2:2 molar ratio, incubated with 8 fold excess of purified TTP, concentrated in an Amicon Ultra 0.5 mL centrifugal filter (Merck) with MWCO of 100.00 kDa, and subjected to SEC on a Superose 6 Increase 3.2/300 column or the home-made S6 long column (S6 resin) in a buffer containing 1x PBS and 2 mM DTT.

StrepTactin Pull-down The reconstitution of the full-length Ccr4-Not complex, co-expressed in insect cells, with TTP-C-tag was performed by a StrepTactin pull-down. After C-tag pull-down of both individually as described above in (3.3 and 3.3), Ccr4-Not and TTP were mixed in a 1:2 molar ratio and incubated with prewashed StrepTactin Sepharose (iba lifesciences) at 4 °C for 45 min rotating. After incubation, the beads were washed 4x with a buffer containing 50 mM HEPES pH 7.4 and 150 mM NaCl. The protein complex was eluted by incubation for 15 min with a buffer containing 50 mM HEPES pH 7.4, 150 mM NaCl and 2.5 mM Desthiobiotin.

3.5 Electron microscopy

All electron microscopes used in this thesis were purchased from FEI (now Thermo Fisher Scientific) by the cryo-EM facility at the MPI of biochemistry, Martinsried. Screening datasets were collected either on a Talos Arctica or a Titan Halo electron microscope, both equipped with a Falcon 3 direct electron detector (Thermo Fisher Scientific) using the EPU (Thermo Fisher Scientific) software, operated by the author of this thesis. The final datasets were collected on a Titan Krios microscope equipped with a K2 Summit or K3 direct electron detector (Gatan) as well as a post-column energy filter by Ingmar Schäfer (MPIB, Conti department), Daniel Bollschweiler, Tillman Schäfer, or Mike Strauss (MPIB, cryo-EM facility).

Sample preparation

Negative staining

For negative stain EM, either commercial carbon-coated copper mesh grids N1-C73nCu20-01 (Quantifoil) or copper grids (Athene G203/G204) coated with a home-made layer of carbon foil, were used. Prior staining, the grids were glow-discharged for 30 s at $2.2 \cdot 10^{-1}$ mba

using a GloQube Plus glow discharge system (Quorum). In the first step, 5 µL of a sample at ∼ 75 nM concentration was applied onto the grid and incubated for 1 min before blotting the excess liquid away. Then the grid was washed 3x with 5 µL of water, and after blotting, 5 µL of 2 % uranylacetate were applied 2x and directly blotted away. In the last step, 5 µL uranylacetate were applied and incubated for 45 – 60 s before blotting.

Cryo-EM

For cryo-EM, R1.2/1.3 Cu 200/300 mesh, R2/1 Cu 200/300 mesh, R2/1 Cu 200/300 + 2 nm carbon holy carbon copper grids (Quantifoil) were used. Grids with an additional layer of graphene oxide were freshly prepared after a protocol from Palovcak *et al.*, 2018, by coating of the above mentioned R1.2/1.3 or R2/1 copper grids. Prior sample application, grids were glow-discharged (except after coating with graphene oxide) for 20-40 s at $2.2 \cdot 10^{-1}$ mbar, using a GloQube (Quorum). Grids were plunge-vitrified in a liquid ethane/propane mix using a FEI Vitrobot ™ Mark IV (FEI, Thermo Fisher Scientific). The environment of the chamber was set to 4 °C and 95 % humidity. After application of 3-5 µL of sample, excess liquid was removed with circular filter papers (Whatman ™ or Ted Pella) with differing blot forces and and blot times.

Ccr4-Not$_{CORE}$

Sample preparation The tetrameric Ccr4-Not$_{CORE}$ was reconstituted, cross-linked and subjected to SEC as described in 3.4. The peak fraction was adjusted to an OD_{280} of 0.15, n-octyl-β-D-glucoside (β-OG) was added to a final concentration of 0.04 % (v/v) and applied to a glow-discharged (20 s at $2.2 \cdot 10^{-1}$ mbar, GloQube) R2/1 Cu200 holey carbon grid (Quantifoil). The grids were plunge-vitrified at 4 °C and 95 % humidity with blotforce 4 for 3.5 s.

Data collection and data processing The final cryo-EM dataset was collected on a Titan Krios microscope, operated at 300 kV, equipped with a K2 Summit direct detector (Gatan) and a post-column energy filter (GIF) by Ingmar Schäfer (MPIB, Conti department). In total 5,450 movies were recorded at a nominal magnification of 130,000x, which corresponds to 1.06 Å/pixel on the specimen level, in counting mode with a total exposure of 59 e^- /Å^2 distributed over 60 frames using SerialEM (Mastronarde, 2003). The collected data was processed in RELION 2.1 and RELION 3.1.1 (Zivanov *et al.*, 2020) as well as cryoSPARC 2 (Punjani *et al.*, 2017). To correct for beam-induced motion and radiation damage, the raw movie frames were aligned and dose-weighed using MotionCor2 (Zheng *et al.*, 2017). The contrast transfer function (CTF) parameters were determined using GCTF (Zhang, 2016). Initial particles were automatically selected by Gautomatch (Zhang software - MRC Laboratory of Molecular Biology) of a subset of micrographs and subjected to initial 2D classification in RELION 2.1. Those initial 2D class averages were used as reference for template picking with Gautomatch. A total of 2,215,912 particle candidates were extracted with a box size of 256 pixels. The particles were cleaned by several rounds of reference-free 2D classification with a circular mask of 200 Åin subsets of ∼200000 particles. An initial model was calculated from a subset of cleaned 2D classes and used low-pass filtered to 60 Å as reference for 3D classification. After several rounds of 3D classification, the class with the highest occupancy and overall resolution was selected and subjected to 3D auto-refinement. The final reconstruction from 77,756 particles reached an estimated resolution of 9 Å, after masked 3D auto-refinement and b-factor sharpening with an ad hoc b-factor of -100 in the RELION post-processing routine according to the Fourier shell correlation (FSC) cut-off criterion for independent half maps of 0.143 (Rosenthal & Henderson, 2003). The estimated resolution, however is over refined due to preferred orientation (automatically determined b-factor at -242). To mitigate the strong preferred orientation, 2001 movies were imported into cryoSPARC, motion corrected with Patch motion and the CTF

parameters were estimated with Patch CTF. First, some particles were selected manually to generate templates, which were then used as templates for the template picker. The template picked particles were cleaned by 2D classification, and after careful examination finally used to train the Topaz picker. In total 555,125 particles were selected, extracted and 2D classified in subsets of 150,000 particles. About 380,349 particles were then subjected to *ab initio* reconstruction of five classes with an altered setting for the maximum resolution to 5 Å.

Ccr4-Not$_{\Delta C}$

Sample preparation The hexameric Ccr4-Not$_{\Delta C}$ was reconstituted over SEC as described in 3.4. The peak fraction was adjusted to an OD_{280} of 0.2 mg/mL and 4 µL were applied to a plasma-cleaned (20 s on low, Plasma Cleaner PDC-32G, Harrick Plasma) R1.2/1.3 Cu200 holey carbon grid (Quantifoil). The grid was plunge frozen in a liquid ethane/propane mix by a Vitrobot Mark IV (FEI, Thermo Fisher Scientific) at 4 °C and 100 % humidity with blotforce 4 for 3.5 s.

Data collection and data processing The cryo-EM dataset was collected on a Talos Arctica microscope, operated at 200 kV, equipped with a Falcon 3 direct detector. In total 840 movies were recorded at a nominal magnification of 92,000x, which corresponds to 1.608 Å/pixel on the specimen level with a total exposure of 85 e^- /Å^2 distributed over 40 frames during 4 s exposure. To correct for beam-induced motion and radiation damage, the recorded movies were aligned and dose-weighed using MotionCor2 (Zheng *et al.*, 2017). CTF parameters were determined using GCTF and particles were automatically picked by Gautomatch. Further processing was carried out in RELION-2.1. The initially selected 250,277 particle candidates were extracted with a box size of 200 pixels and cleaned in

several rounds of reference-free 2D classification with circular masks of 220-230 Å. A 3D reconstruction from a negative stain dataset (data not shown) was low-pass filtered to 60 Å and uses as a reference for 3D classification. After two rounds of 3D classification, the class with the most detail and highest occupancy was subjected to 3D auto-refinement. The final reconstruction from 28,206 particles reached an estimated resolution of ∼14 Å, after masked 3D auto-refinement and b-factor sharpening with an ad hoc b-factor of -100 in the RELION post-processing routine according to the FSC cut-off criterion for independent half maps of 0.143 (Rosenthal & Henderson, 2003).

Full Ccr4-Not

Sample preparation The sample was purified as described in 4.13 in a two-step purification, 0.04 % (v/v) of β-OG added and 3.5 µL directly applied to a glow-discharged (30 s at $2.2 \cdot 10^{-1}$ mbar, GloQube Plus, Quorum) R2/1 Cu200 holey carbon grid (Quantifoil) with an additional 2 nm carbon support film and plunge-vitrified at 4 °C and 95 % humidity with blotforce 4 and a blot time of 3.5 s.

Data collection and data processing A cryo-EM dataset was collected on a Titan Krios microscope operating at 300 keV, equipped with a K3 direct electron detector and a post-column energy filter. In total 17,803 movies were recorded at a nominal magnification of 81,000 x, which corresponds to 1.094 Å/pixel on the specimen level with a total exposure of ∼75 e^- /Å^2 distributed over 42 frames. To correct for beam-induced motion and radiation damage, the recorded movies were aligned and dose-weighed using MotionCor2 (Zheng *et al.*, 2017) within FOCUS. The aligned micrographs were imported to cryoSPARC 2. CTF parameters were determined by Patch CTF and a small subset of particles was picked manually. Those initially picked particles were classified in 2D and the resulting 2D class averages after by-eye inspection used for template picking. After further classification in

2D, the particles were used to train the Topaz picker (Bepler *et al.*, 2019). The particles extracted by Topaz extract were subjected to reference-free 2D classification in subsets and the coordinates of the cleaned stacks then exported into RELION 3.1. The particles were extracted in a box size of 96 pixels, 4x binned to a resulting pixel size of 4.376 Å. The particles were then further 2D classified in subsets. After reextraction of the particles with the initial pixel size of 1.094 Å/px and a further round of 2D classification, the resulting 2D class averages showed less detail than the binned 2D class averages.

The binned 2D class averages were used as templates for template-picking in Gautomatch. About 3.9 million initial particle candidates were picked and cleaned up by several rounds of 2D classification in subsets. The remaining $\sim$ 890,000 particles were then subjected to 3D classification. Subsets of class averages were used to build an initial model, which was low-pass filtered to 60 Å and used as a reference for 3D classification. The resulting 3D reconstructions (Fig. 4.14) revealed classes of larger and more compact shape. Both shapes (indicated by the dashed rectangle) were selected and subclassified individually. The classes with the highest occupancy and estimated resolution were selected, pooled and subjected to another 3D classification with a mask. The best two of the resulting 3D reconstructions were selected and the particles reextracted with the original pixel size of 1.94 Å/px. The particles were then subjected to the final 3D classification, which resulted in the four classes shown at the bottom of the processing scheme. The indicated classes were subjected to 3D auto-refinement, however the resulting 3D reconstruction showed strong masking artifacts and less detail than the 3D reconstructions. Therefore, for interpretation, the 3D-density from the final 3D classification, indicated by a dashed rectangle, was used.

Density interpretation

Rigid-body fitting of simulated maps of available atomic models into the 3D reconstructions was carried out in UCSF chimera (Pettersen *et al.*, 2004).

3.6 Cross-linking Mass Spectrometry

After C-tag elution, the full Ccr4-Not complex was diluted to a final protein concentration below 0.3 mg/mL (∼0.5 µM) to avoid over cross-linking. BS^3 was added to a final concentration of 1 mM and incubated for 10 min on ice. The reaction was quenched with 20 mM Tris-HCl at pH 7.4. The Ccr4-Not:TTP complex was reconstituted as described in 3.4. To reconstitute Ccr4-Not:TTP:RNA, Ccr4-Not:TTP (∼ 0.5 µM) was mixed with 0.8 µM biotin-ARE-25 GGGAA RNA and incubated for 10 min on ice. Afterwards, both samples, Ccr4-Not:TTP and Ccr4-Not:TTP:RNA were cross-linked by adding BS^3 to a final concentration of 1 mM and incubation for 10 min on ice. The reactions were quenched with 20 mM Tris-HCl at pH 7.4.

Crosslinked proteins were diluted 1:1 with digestion buffer (8 M Urea, 40 mM CAA, 10 mM TCEP, 50 mM Tris). The mixture was sonicated using a Bioruptor Plus sonication system (Diogenode) for 10x 30 sec at high intensity and subsequently incubated for 20 min at 37 °C. Thereafter, the samples were diluted 1:2 with MS grade water (VWR). Crosslinked proteins were digested overnight at 37 °C by addition of 1 µg of LysC and 2 µg of trypsin (Promega). Afterwards, the mixture was acidified with 10 % trifluoroacetic acid (TFA; Merck) in water to a final concentration of 1 %, followed by desalting of the peptides using Sep-Pak C18 1cc vacuum cartridges (Waters). Desalted peptides were vacuum-dried. Additionally, desalted peptides were offline from the MS fractionated into 8 fractions using a high pH reversed-phased fractionation system (Kulak *et al.*, 2017).

Vacuum-dried peptides were dissolved at a concentration of 400 ng/ µL in buffer A (0.1 % formic acid). Peptides (400 ng) were separated and measured at a flow rate of 250 nL/min using the Thermo Easy-nLC 1200 (Thermo Fisher Scientific) equipped with a 30-cm analytical column (inner diameter: 75 microns; packed in-house with ReproSil-Pur C18-AQ 1.9-micron beads, Dr. Maisch GmbH) coupled to the benchtop Orbitrap Q Exactive

HF (Thermo Fisher Scientific) mass spectrometer (Scheltema *et al.*, 2014). For the LC separation, the following gradient was programmed with increasing addition of buffer B (80 % acetonitrile, 0.1 % formic acid): linear increase from 8 to 30 % over 60 minutes, followed by a linear increase to 60 % over 5 minutes, a linear increase to 95 % over the next 5 minutes, and finally maintenance at 95 % for another 5 minutes. The mass spectrometer was operated in data-dependent mode with survey scans from m/z 300 to 1650 Th (resolution of 60k at m/z = 200 Th), and up to 15 of the most abundant precursors were selected and fragmented using stepped Higher-energy C-trap Dissociation (HCD with a normalized collision energy of value of 19, 27, 35). The MS2 spectra were recorded with dynamic m/z range (resolution of 30k at m/z = 200 Th). AGC target for MS1 and MS2 scans were set to 3 x 10^{6} and 10^{5}, respectively, within a maximum injection time of 100 and 60 ms for the MS1 and MS2 scans, respectively. Charge state 2 was excluded from fragmentation to enrich the fragmentation scans for cross-linked peptide precursors.

The acquired raw data were processed using Proteome Discoverer (version 2.5.0.400) with the XlinkX/PD nodes (Klykov *et al.*, 2018) integrated. To identify the crosslinked peptide pairs, a database search was performed against a FASTA containing the sequences of the proteins under investigation as well as a contaminant database. DSS was set as a crosslinkers. Cysteine carbamidomethylation was set as fixed modification and methionine oxidation and protein N-term acetylation were set as dynamic modifications. Trypsin/P was specified as protease and up to two missed cleavages were allowed. Furthermore, identifications were only accepted with a minimal score of 40 and a minimal delta score of 4. Otherwise, standard settings were applied. Filtering at 1 % false discovery rate (FDR) at peptide level was applied through the XlinkX Validator node with setting simple.

XL-MS data was mapped on available crystal structures of subcomplexes of Ccr4-Not and the predicted structure of TTP from Alphafold 2 (Jumper *et al.*, 2021) using XlinkAnalyzer (Kosinski *et al.*, 2015) within USCF chimera (Pettersen *et al.*, 2004). Therefore, the

numbers of cross-linked residues were edited to account for the N-terminal His-TEV-tag (-25) of CNOT1 and its isoform 2 (+5 residues at position 822). The presented model of Ccr4-Not shows cross-links filtered for cross-link confidence scores of 90 or higher except for CNOT6:CNOT7:CNOT1 MIF4G as the highest identified cross-links had confidence scores of 55.

3.7 Mass photometry

Mass photometric measurements were performed using a One ^{MP} mass photometer (Refeyn). Before measurement, microscope coverslips and gaskets were cleaned by sonication in isopropanol and Milli-Q water and then dried with a clean stream of nitrogen. After mounting a gasket on a coverslip, 18 µL of buffer was applied to a gasket to find the focus. Automatic focusing and data acquisition was performed using AcquireMP (Refeyn). After securing the focus position, 0.5 µL of diluted (1:50) NativeMark ^{TM} (Invitrogen, Thermo Fisher Scientific) was mixed with the buffer, and a 12000-frame movie was acquired for mass calibration. The movie was subsequently processed and analyzed using DiscoverMP (Refeyn). Protein samples were diluted to ∼50-100 nM prior MP measurements. After focusing in buffer, 2 µL of the diluted sample was mixed with 18 µL of buffer, further diluting the sample by a factor of 10. Movies of 6000 frames were collected per sample and directly processed and analyzed.

3.8 RNA methods

Deadenylation assays

The deadenylation activity of Ccr4-Not or Ccr4-Not$_{CORE}$ was analyzed in deadenylation time course experiments in a similar setup as described before (Webster *et al.*, 2017; Stowell

et al., 2016; Raisch *et al.*, 2019). In a total reaction volume of 40 µL, 200 nM of synthetic RNA substrates were mixed with 40 nM of heterologously expressed and purified Ccr4-Not or Ccr4-Not$_{CORE}$ complexes. Reactions were carried out at 37 °C for 60 min in a buffer containing 20 mM PIPES pH 6.8, 20 mM NaCl, 0.2 mM $Mg(OAc)_2$ 10 mM KCl, and 1 mM DTT. The RNA substrates (synthesized by Ella Biotech GmbH) comprised a 20-mer of non-poly(A) nucleotides (with or without a canonical ARE) with poly(A) tails, differing in length and composition, and were labeled with fluorophores at their 5'end (Atto-550 or Atto-647N). For the exact sequences see 2.5. Ccr4-Not WT/DM was prepared as described before in a storage buffer containing 20 mM HEPES/NaOH, pH 7.5, 150 mM NaCl, 2 mM SEPEA). Buffers (reaction buffer and dilution buffer and the respective RNA were mixed and the reaction was started by the addition of the enzyme complexes Ccr4-Not or Ccr4-Not$_{CORE}$. For targeted deadenylation assays in the presence of TTP, buffers, RNA and TTP (250 nM final concentration) were mixed and incubated for 10 min at RT before adding the enzymes. At indicated time points 4 µL aliquots were taken. The reaction was stopped immediately by adding 4 µL stop buffer (50 mM EDTA, 0.1 % (v/v) SDS). To degrade the proteins, 0.25 µL of Proteinase K (NEB) was added and the samples were incubated for 10 min at 37 °C. After the addition of 8 µL of OFE loading dye (0.1 % Orange G, 10 mM EDTA pH 8.0, 98 % Formamide), samples were separated on 10 %-Urea-PAGE.

RNA gels

Polyacrylamide Urea gels were home-made (2.6) and pre-run in 1xTBE for 30 min at 10 W. Samples mixed with 100 % OFE, were boiled for 5 min at 95 °C and applied to the pre-ran Urea-gel. RNAs of indicated length labeled with fluorophores at the 5' ends were used as molecular weight markers. Gels were run at 10 W until the orange marker reached the bottom of the gel. Gels were imaged with Typhoon™ FLA9500 or Amersham™ Typhoon™ in separate detection channels with excitations at 532 nM (Cy3) and 635 nm

(Cy5). The images of both channels were later merged using Fiji (Schindelin *et al.*, 2012).

Chapter 4

Results

4.1 Purification and reconstitution of subcomplexes of human Ccr4-Not

A major hurdle before starting the structural studies was purifying sufficient amounts of the full-length complex in pure and stoichiometric quality. Initially, smaller subcomplexes were reconstituted, as the potential for higher resolution was greater. Structural models could also facilitate the interpretation of a potential medium- to low-resolution reconstruction of the full complex. In this stepwise procedure, different expression strategies and also expression systems were tested. Subunits known to interact with each other were expressed together to increase stability. The final expression and purification strategies for reconstitution of these subcomplexes are presented in the following sections.

4.1.1 Purification and reconstitution of Ccr4-Not$_{CORE}$

The catalytic core of the Ccr4-Not complex, the nuclease module, consists of the two exonucleases CNOT6 and CNOT7, which are integrated into the complex via the interaction of CNOT7 with the MIF4G domain of CNOT1. High-resolution structures of the two yeast nucleases with the MIF4G domain of NOT1 (Basquin *et al.*, 2012), the human nuclease CNOT7 with TOB (Horiuchi *et al.*, 2009), and more recently the human nucleases (Chen *et al.*, 2021) have been solved, but no structure of the two enzymes is available in the context of the surrounding domains of the complex. Therefore, a tetrameric complex, named Ccr4-Not$_{CORE}$, comprising the central part of CNOT1$_{813\text{-}1596}$ (CNOT1-C), CNOT6 and CNOT7, and CNOT9 (see scheme in Fig. 4.1), was reconstituted from separately expressed and purified subcomplexes.

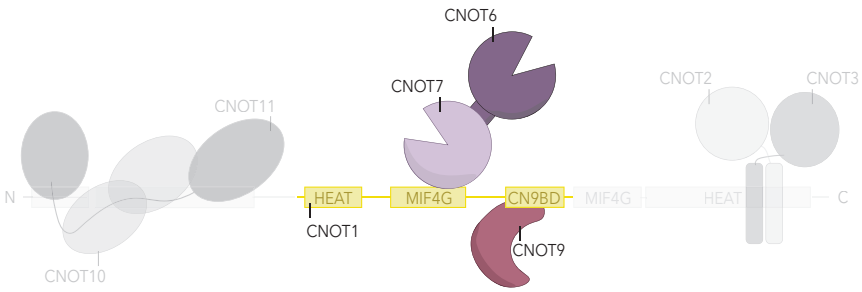

Figure 4.1. Schematic representation of the Ccr4-Not$_{CORE}$ complex. The four subunits of this subcomplex, the central part of CNOT1 (yellow), the nucleases CNOT6 (dark purple) and CNOT7 (light purple), and CNOT9 (dark red) are highlighted. Other parts of the Ccr4-Not complex are colored in light grey.

The CNOT6:CNOT7 subcomplex was expressed as a fusion construct linked by a 3C cleavage site in insect cells. The fusion protein was then captured by metal affinity chromatography, applied to a heparin column, and after proteolytic tag and fusion site cleavage finally purified via SEC, thereby obtaining a pure, stoichiometric complex. The CNOT1-C:CNOT9 heterodimer was co-expressed in *E. coli* BL21 Star pRARE and purified by a similar procedure as the CNOT6:CNOT7 subcomplex. SDS-PAGE analyses of the final

purification steps (Fig. 4.2 A) reveal a stoichiometric CNOT1-C:CNOT9 complex with multiple contamination and degradation bands. The asterisk indicates a recurring protein band at approximately 70 kDa that likely corresponds to a heat shock protein from *E. coli* that was not completely removed despite an additional wash step with a buffer containing magnesium and ATP to stimulate release.

To obtain a large batch of the complex for activity assays, His-3C-CNOT1-C, CNOT9, CNOT6, and CNOT7 were recloned into a pBIG1a vector by Gibson assembly and co-expressed in Hi5 insect cells. A complex containing catalytically inactive nucleases serving as a negative control was cloned in the same manner. Conserved glutamate or aspartate residues in the active sites of the nucleases were mutated to alanine (CNOT6M (E240A) and CNOT7M (D40A,E42A)), as was shown to inhibit deadenylation before (Yi *et al.*, 2018). The complexes were purified in a three-step purification, first captured with the N-terminal His-tag on $CNOT1_{813\text{-}1596}$, followed by a heparin column, and finally purified over SEC. SDS-PAGE-analysis of the gel filtration revealed a sub stoichiometric complex in the main fractions of the peak (Fig. 4.2 C), so only fractions with a stoichiometric ratio of CNOT6 were pooled, aliquoted, and stored at -80 °C. The results of the activity assays are presented in 4.4.2.

To reconstitute the $Ccr4\text{-}Not_{CORE}$ complex, the purified subcomplexes CNOT1-C:CNOT9 and CNOT6:CNOT7 were mixed in a 1:1.1 molar ratio, concentrated and separated from excess of subcomplexes by SEC. To prevent disintegration of the complex during the cryo-EM sample preparation, the complex was covalently cross-linked with 0.7 mM bis-sulfosuccinimidyl-suberate (BS^3) before subjected to SEC. Fig. 4.2 B shows the SEC elution profiles of a native reconstituted (left chromatogram) and a cross-linked (right chromatogram) complex. The native complex elutes in a symmetrical peak at 1.55 mL retention volume, while the cross-linked complex elutes at the same volume, but with a broad shoulder due to a mixture of cross-linked larger assemblies. The analysis of the peak fractions

by gradient SDS-PAGE reveals a stoichiometric native complex with a minor chaperone contamination (asterisk). The main peak fraction of the cross-linked sample shows partial cross-linking with a smear at higher molecular weights but also still remaining bands for the individual subunits.

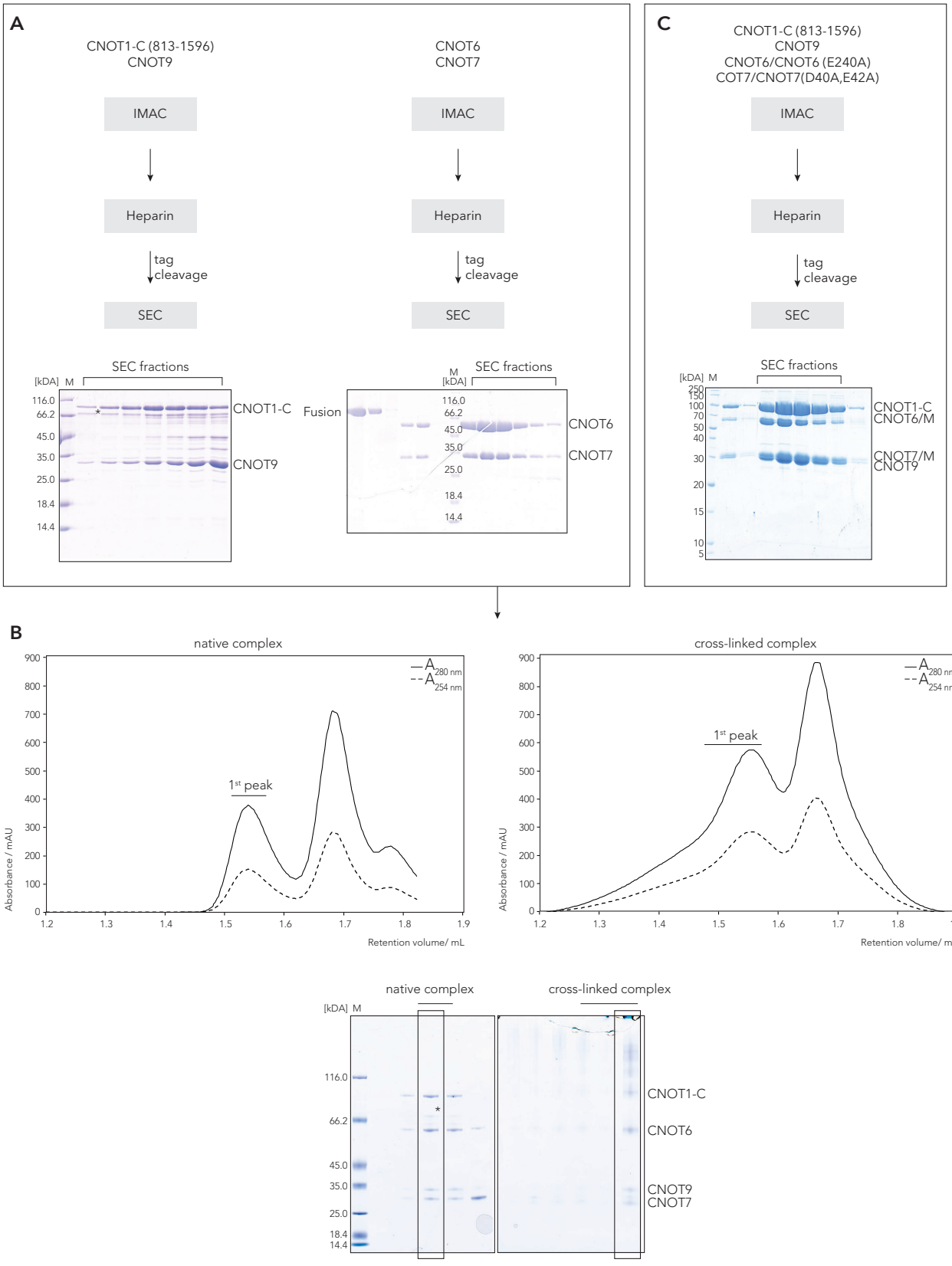

Figure 4.2. Reconstitution of Ccr4-Not$_{CORE}$. **A,** Purification strategies of the CNOT1-C:CNOT9 and CNOT6:CNOT7 subcomplexes. Coomassie-stained SDS-PAGE analyses show the final step of each purification. **B,** SEC elution profiles of the reconstituted and cross-linked Ccr4-Not$_{CORE}$ complexes from a S6i 3.2/300 SEC column. Coomassie-stained SDS-PAGE analysis of the peak fractions of the respective elution profile. Black boxes indicate the fractions used for cryo-EM sample preparations. **C,** Purification of co-expressed CNOT1-C (813-1596), CNOT9, CNOT6/M, CNOT7/M in insect cells. Coomassie-stained SDS-PAGE analysis shows the SEC fractions. M indicates the lane with size markers (in all gels of the thesis).

Cryo-EM studies of Ccr4-Not$_{CORE}$

Samples of the peak fractions from native and cross-linked complex reconstitutions (Fig. 4.2 B) were applied on R1.2/1.3 Cu200 grids and plunge-vitrified using the Vitrobot Mark IV and examined in cryo-EM for their behavior in ice, suitable concentrations, and freezing conditions. The cross-linked complex showed well distributed particles and a homogeneous ice layer in the range of 0.1-0.25 mg/mL (450 nM-1130 nM) with 0.04 % of detergent β-OG (data not shown). A large dataset of 5450 movies was collected on a Titan Krios microscope, equipped with a K2 direct electron detector. Details of sample preparation and data collection are described in 3.5. As can be seen on the representative micrograph in Fig. 4.3 A, the individual particles are clearly visible and well distributed. After alignment and dose-weighing of the micrographs using MotionCor2, particles were automatically picked using Gautomatch. After initial 2D classification, the generated 2D class averages were used for automated template picking with Gautomatch. About 2.2 million particles were extracted with a box size of 256 px and subjected to several rounds of reference-free 2D classification with a circular mask of 200 Å in subsets. Representative 2D class averages (4.3 A, right panel) show a heterogeneous dataset with particles of different sizes as well as flexible regions (less well resolved details). The majority of 2D classes likely represent the individual subunits, only a few class averages are larger and could represent the tetrameric complex. High-resolution features are only visible in the first two very similar classes. An initial 3D model was generated from subsets of 2D classified particles and used as 3D reference for 3D classification after low-pass filtering. The 3D classes (4.3 B) show L-shaped particles with two arms of approximately equal length and, like the 2D classification, exhibit heterogeneity as the distance of the two arms of the L varies. In some classes the arms even appear to be connected, resulting in a more triangular shape. The class with the highest occupancy and resolution was selected and subjected to further processing. After two more steps of 3D classifications, the class with the highest occupancy and resolution

was selected and subjected to 3D auto-refinement. As can be seen in 4.3 B in the spherical angular distribution, the sample suffers from a strong preferred orientation. This was already suggested in 2D and continued in 3D. The achievable resolution was limited by the strong preferred orientation and the small number of particles in total. The estimated nominal resolution of $\sim$ 9 Å using an ad-hoc b-factor of -100 (automatically determined b-factor of -242), is likely over-refined and not representing the true resolution due to the preferred orientation in one direction. The resolution was not sufficient to unambiguously assign the atomic models of CNOT6:CNOT7 and CNOT1(CN9BD):CNOT9 to the density (Fig. 4.4, B).

Various processing techniques were used to mitigate the strong preferred orientation. The most successful was the Topaz picker embedded in the cryoSPARC environment. Details of the particle picking are described in 3.5 and shown in Fig. 4.3 C. After one round of 2D classification, the cleaned particle stack was subjected to *ab initio* reconstruction. Three reconstructions were selected and subjected to another *ab initio* reconstruction job with the much higher maximum resolution limit of 5 Å instead of default 12 Å. The resulting 3D reconstructions are highly over-refined and further processing steps did not reveal the same detail as the *ab initio* reconstructions. These classes were nevertheless useful for placing the atomic models and obtaining more information about the composition of heterogeneity. Rigid-body fitting of simulated maps of the atomic models to interpret the 3D reconstructions of cryoSPARC using UCSF chimera is shown in Fig. 4.4 C-E. The dataset appears to consist of individual subunits (Fig. 4.4, D) or the CNOT6:CNOT7 subcomplex in slightly different conformations (Fig. 4.4 C, E).

A complex containing all four proteins is not visible, either because of flexibility or because of disintegration and insufficient cross-linking or general underrepresentation.

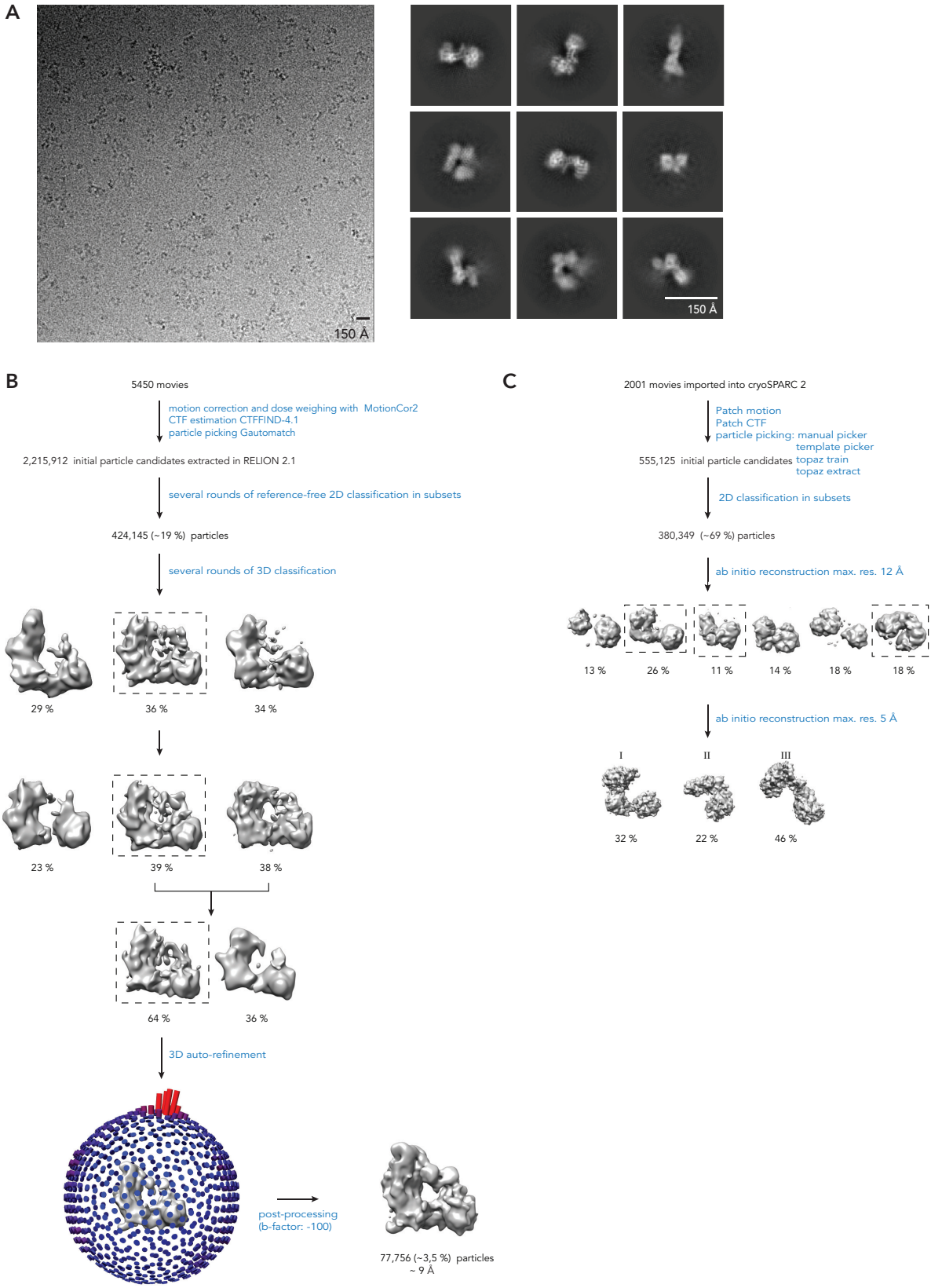

Figure 4.3. Cryo-EM dataset of Ccr4-Not$_{CORE}$. A, Representative micrograph (left panel) and 2D class averages with a circular mask of 200 Å (right panel) of the Ccr4-Not$_{CORE}$ dataset, recorded on a Titan Krios microscope, operating at 300 kV, equipped with a K2 Summit direct detector at a nominal magnification of 130,000x which corresponds to a pixel size of 1.06 Å/px. Scalebars indicate 150 Å. **B, C** Processing schemes of the single-particle cryo-EM dataset of the Ccr4-Not$_{CORE}$ sample in RELION 2.1/3.1.1 and cryoSPARC 2. The dashed rectangles indicate the classes selected for further processing steps.

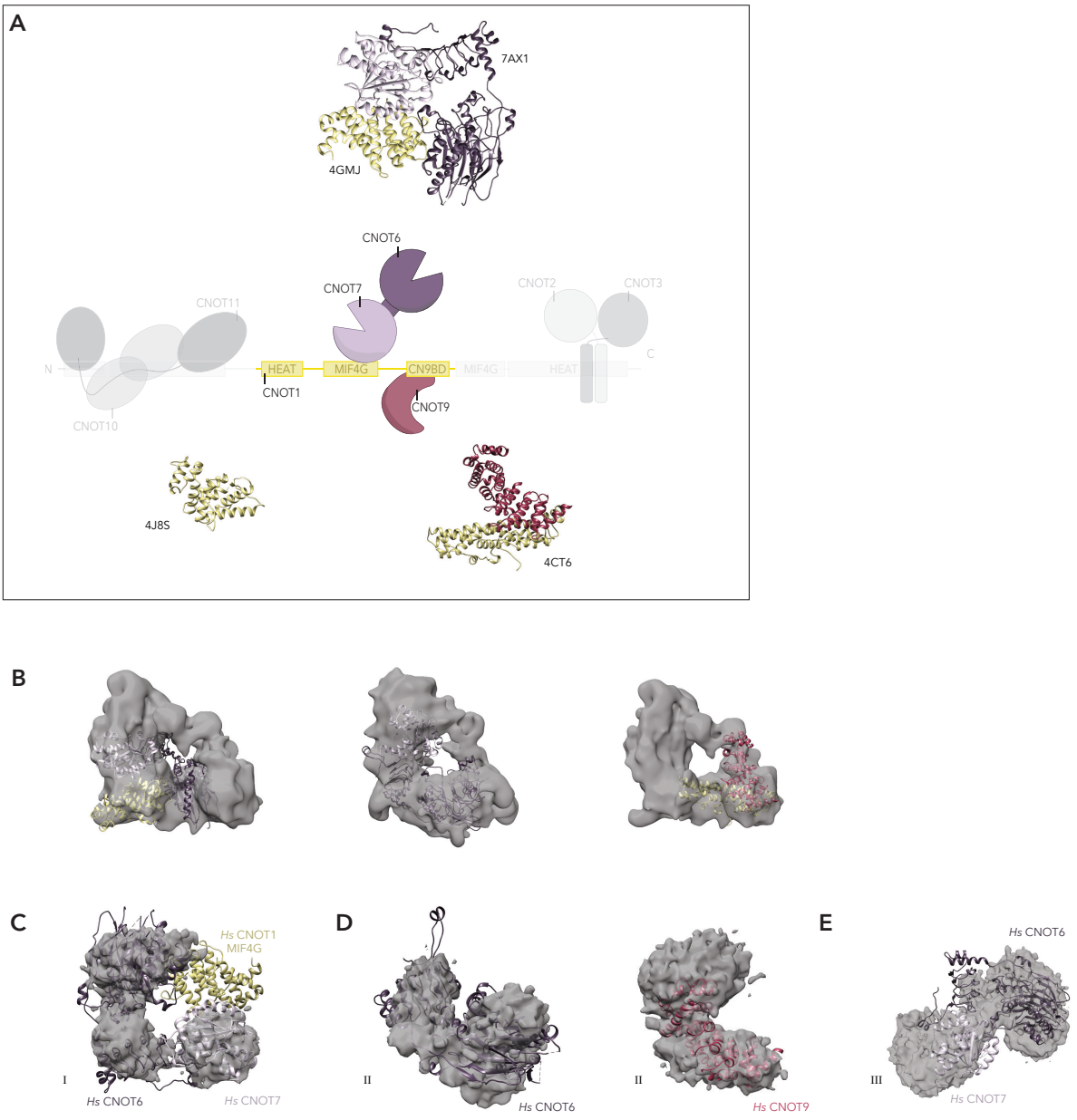

Figure 4.4. Possible interpretation of the 3D reconstructions of Ccr4-Not$_{CORE}$ with available structural models. A, Schematic representation of Ccr4-Not$_{CORE}$ complex with available atomic models of the CNOT1$_{820\text{-}999}$ HEAT domain (PDB:4J8S), the CNOT1$_{1352\text{-}1594}$ CN9BD:CNOT9 (PDB:4CT6) subcomplex and a composite model of a CNOT6:CNOT7:MIF4G (PDB:7AX1, 4GMJ) subcomplex in cartoon representation. Domains of CNOT1 are highlighted in pale yellow, CNOT6 in dark purple, CNOT7 in light purple and CNOT9 in dark red. Rigid-body fitting of the atomic models into 3D reconstructions processed in RELION 2.1/3.1 (**B**) and cryoSPARC 2 (**C-E**) using UCSF chimera. **B,** Simulated maps from the atomic models can be fitted with a correlation of 0.83 for CNOT6:CNOT7, 0.76 for CNOT1$_{1093\text{-}1317}$ MIF4G:CNOT6:CNOT7, and 0.851 for CNOT1$_{1352\text{-}1594}$ CN9BD-CNOT9 into the density. **C-E,** Simulated maps from CNOT1$_{1093\text{-}1317}$ MIF4G:CNOT6:CNOT7, can be fitted with a correlation of 0.7 into Class I, CNOT9 with a correlation of 0.803 or CNOT6 with a correlation of 0.756 can be fitted into Class II. Simulated maps of the nucleases CNOT6:CNOT7 can be fitted with a correlation of 0.77 into Class III.

4.1.2 Purification and reconstitution of Ccr4-Not$_{\Delta C}$

Ccr4-Not$_{\Delta C}$:BTG2

The hexameric Ccr4-Not$_{\Delta C}$ complex consists of the CNOT10, CNOT11, CNOT6, CNOT7, and CNOT9 subunits, which bind to a shorter CNOT1-N (1-1596) construct lacking the C-terminus containing the binding sites for CNOT2:CNOT3 (see schematic representation in Fig. 4.5).

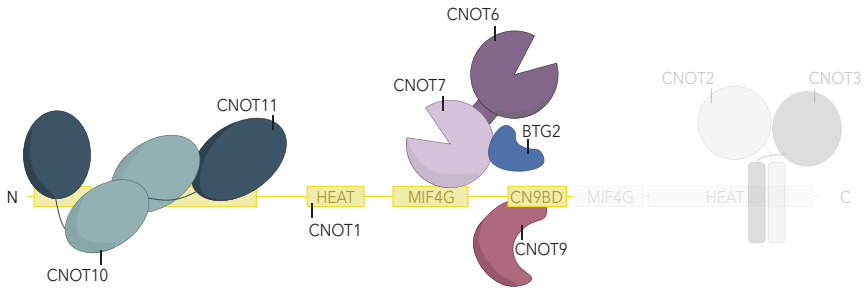

Figure 4.5. Schematic representation of the Ccr4-Not$_{\Delta C}$:BTG2 complex. The subunits of this subcomplex, CNOT1-N (yellow), CNOT10 (pale green), CNOT11 (dark blue), the nucleases CNOT6 (dark purple) and CNOT7 (light purple), CNOT9 (dark red) and BTG2 (blue) are highlighted. Other parts of Ccr4-Not are colored in light grey.

It was reconstituted from purified subcomplexes co-expressed in *E. coli*. The boundaries of the CNOT1 construct were selected based on Mathys *et al.*, 2014, lacking the C-terminus to simplify the complex reconstitution and to reduce the flexibility for the structural characterization. Constructs for CNOT10Δ (1-714 Δ492-504) and CNOT11 (6-510) omitted regions predicted to be unstructured, while CNOT6, CNOT7, and CNOT9 were cloned and expressed as full-length versions. The CNOT1-N:CNOT9 and CNOT10Δ:CNOT11 subcomplexes were purified in a three-step purification procedure. The quality of the final subcomplexes was verified by SDS-PAGE (see Fig. 4.6 A). The resulting CNOT1-N:CNOT9 complex was stochiometric but some proteolytic degradation was apparent on SDS-PAGE analysis, while the CNOT10Δ:CNOT11 heterodimer was purified in pure quality. CNOT6

and CNOT7 were co-expressed with BTG2 in *E. coli* to stabilize the subcomplex and thereby improve solubility. BTG2 is an antiproliferative protein, that is directly interacting with CNOT7 and PABPC1, thereby stimulating deadenylation (described in 1.3.4). The trimeric complex was purified in a three-step purification procedure including proteolytic tag-cleavage. The Coomassie-stained SDS-PAGE analysis revealed a double band at the height of CNOT7, which was identified by mass spectrometry analysis as CNOT7 with incomplete cleavage of the 8.6 kDa SUMO tag.

Ccr4-Not$_{\Delta C}$ with BTG2 was reconstituted by mixing the purified subcomplexes CNOT1-N:CNOT9, CNOT10Δ:CNOT11, and CNOT6:CNOT7:BTG2 in a 1:1.2:1.2 molar ratio. According to the SDS-PAGE analysis, the excess of subcomplexes was successfully removed by SEC (see Fig. 4.6 B, 2nd and 3rd peak), the reconstituted complex appeared pure and stoichiometric, however the double band of CNOT7 could not be separated.

Cryo-EM studies of Ccr4-Not$_{\Delta C}$:BTG2

The complex was reconstituted as described before and directly used to prepare samples for cryo-EM. The sample was applied on R1.2/1.3 Cu200 grids and plunge-vitrified using the Vitrobot Mark IV. In total 840 movies were collected on a Talos Arctica microscope, operating at 200 keV, equipped with a Falcon 3 direct detector. The micrographs show clearly visible and well distributed individual particles, which, however, do not appear completely homogeneous in size and shape (Fig. 4.7, A left panel). After alignment and dose-weighing using MotionCor2, the CTF parameters were determined by GCTF. Particles were picked automatically by Gautomatch. From particle extraction on, all processing steps were carried out in RELION 2.1. The initially picked 250,000 particle candidates were cleaned in reference-free 2D classification with a circular mask of 230 Å. The dataset is very heterogeneous as the representative 2D class averages (4.7 A, right panel) show particles of different sizes and less well resolved densities indicating flexibility. The colored

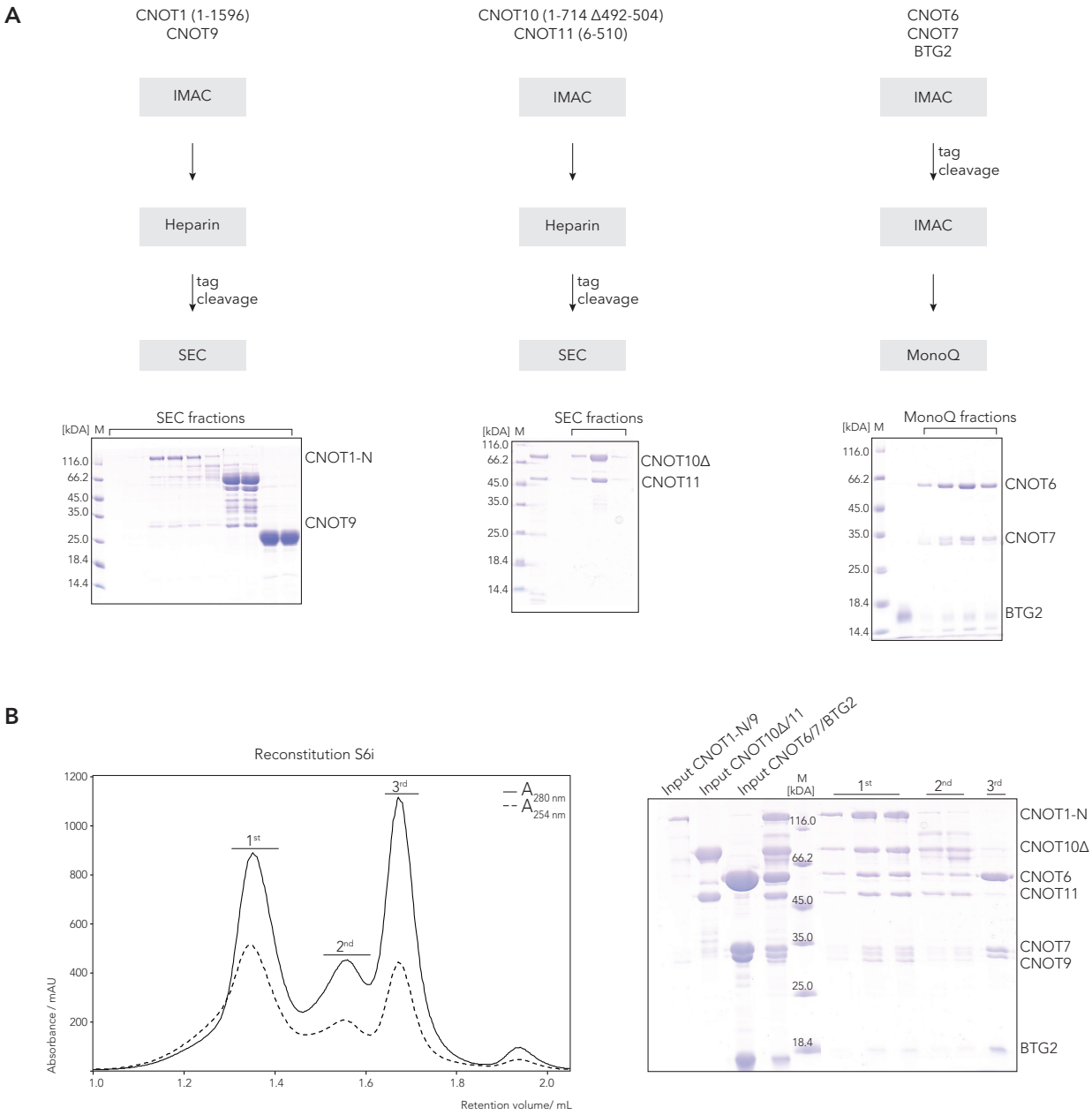

Figure 4.6. Reconstitution of Ccr4-Not$_{\Delta C}$:BTG2 complex. A, Purification strategies of CNOT1-N (1-1596):CNOT9, CNOT10Δ (1-714 Δ492-504): CNOT11 (6-510), and CNOT6:CNOT7:BTG2 subcomplexes. Coomassie-stained SDS-PAGE analyses show the last step of each purification. **B,** Reconstitution of the Ccr4-Not$_{\Delta C}$:BTG2 complex. The complex was reconstituted by mixing the purified subcomplexes CNOT1-N:CNOT9, CNOT10Δ:CNOT11, CNOT6:CNOT7:BTG2 in 1:1.2:1.2 molar ratio. Left panel, SEC elution profile. Right panel, Corresponding Coomassie-stained SDS-PAGE with samples from the subcomplexes, the input and peak fractions.

circles indicate different particle groups sorted by eye. The class averages, which make up the majority of particles, are indicated by a purple circle. These 2D class averages show W-shaped particles, with some high-resolution features and a lower-resolution additional density extending from one side of the W. The dashed lines indicate classes where the extension is missing. A small particle that probably represents a single subunit that has separated from the complex or a top view is indicated by the red circle. However, due to the limited resolution, the subunit cannot be identified unambiguously. The largest particle which shows most high-resolution features, marked in blue, represents about 2 % of the particles. Overall, none of the 2D class averages shown appear to be large enough to represent the entire hexameric Ccr4-Not complex and BTG2. The CNOT1:CNOT10:CNOT11 subcomplex already comprises a diameter of ∼140 Å, and most of the 2D classes are smaller with a diameter of max. ∼110 Å, but a view that obscures most of the complex cannot be ruled out. The heterogeneity suggests partial disintegration or flexible binding of the subunits, which cannot be resolved.

After 2D classification the cleaned particle stack was subjected to 3D classification, using a 3D model from a negative stain data set (data not shown) as a reference. Fig. 4.7 B shows the resulting 3D models. The class that had the most detail and the highest occupancy was selected and further classified. The resulting model was then subjected to 3D auto-refinement without solvent flattening and applied a negative b-factor of 100 during post-processing. The final density from about 28,000 particles (11 % of total particles) reached an estimated resolution of ∼14 Å. The dashed box (Fig. 4.7 B) marks the 3D reconstruction resulting from the final 3D classification, that was used to position the known atomic models of subunits and subcomplexes, as it had more detail than the refined and post-processed densities.

Rigid-body fitting of simulated maps of the atomic models to interpret the 3D reconstruction (see Fig. 4.8 D-F) using UCSF chimera confirmed what was already suggested in the

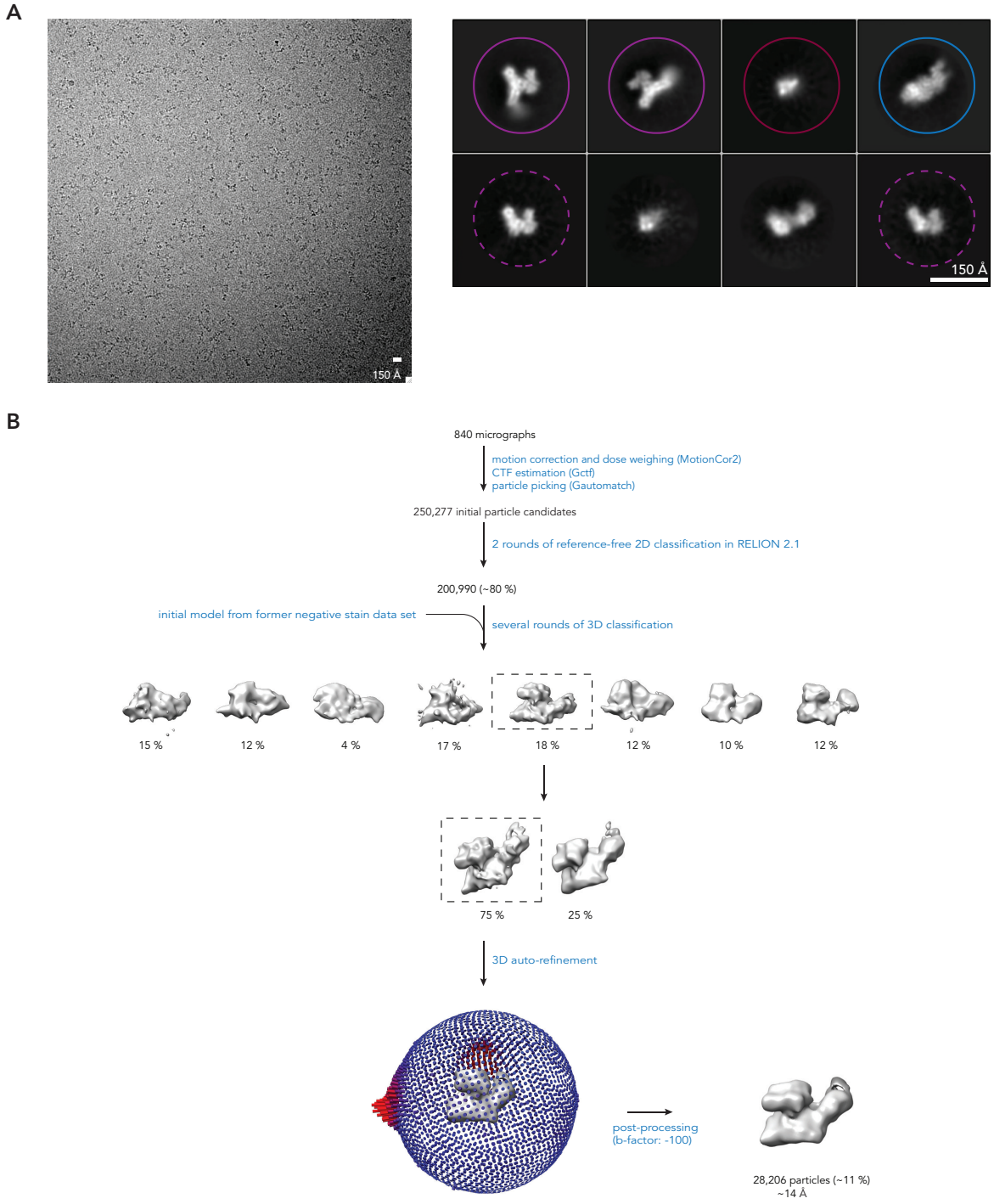

Figure 4.7. Cryo-EM dataset of Ccr4-Not$_{\Delta C}$:BTG2. A, Representative micrograph (left panel) and 2D class averages with a circular mask of 230 Å(right panel) of the Ccr4-Not$_{\Delta C}$:BTG2 dataset. The colored circles mark subsets of similar 2D class averages. Pixelsize = 1.608 Å/px, scalebars indicate 150 Å. **B,** Processing scheme of the cryo-EM dataset.

2D classification, that the density was too small to accommodate all subunits of the hexameric Ccr4-Not$_{\Delta C}$ complex and BTG2. The atomic model of the nuclease:BTG2 module shown is a composite model of the human CNOT6:CNOT7 (PDB:7AX1), CNOT7:Tob (PDB:2d5r), BTG2 (PDB:3E9V), and CNOT7:MIF4G (PDB:4GMJ) crystal structures. The position of the CNOT6 nuclease domain is rotated relative to the yeast Ccr4 nuclease domain (not shown) by approximately 80°, indicating the flexibility of this domain, and thus could be arranged differently. Tob is a homolog of BTG2 and superposition of the structures showed a very similar fold, so it was hypothesized that BTG2 might bind to CNOT7 in a similar manner.

Simulated maps of the atomic models of the nuclease module with BTG2 (correlation of 0.855) and the CNOT9 module (correlation of 0.916) could be placed in several positions in the 3D reconstruction by rigid-body fitting (Fig. 4.8 E, F), whereas a the N-terminal module could only be placed in one specific position in the density (correlation of 0.838) (Fig. 4.8, D). The simulated map of the N-terminal module at 15 Å looks very similar to the 3D reconstruction, so the 3D reconstruction probably corresponds to this module only (Fig. 4.8, C). Accordingly, the hexameric Ccr4-Not complex with BTG2 appears to be too flexible or to have disassembled.

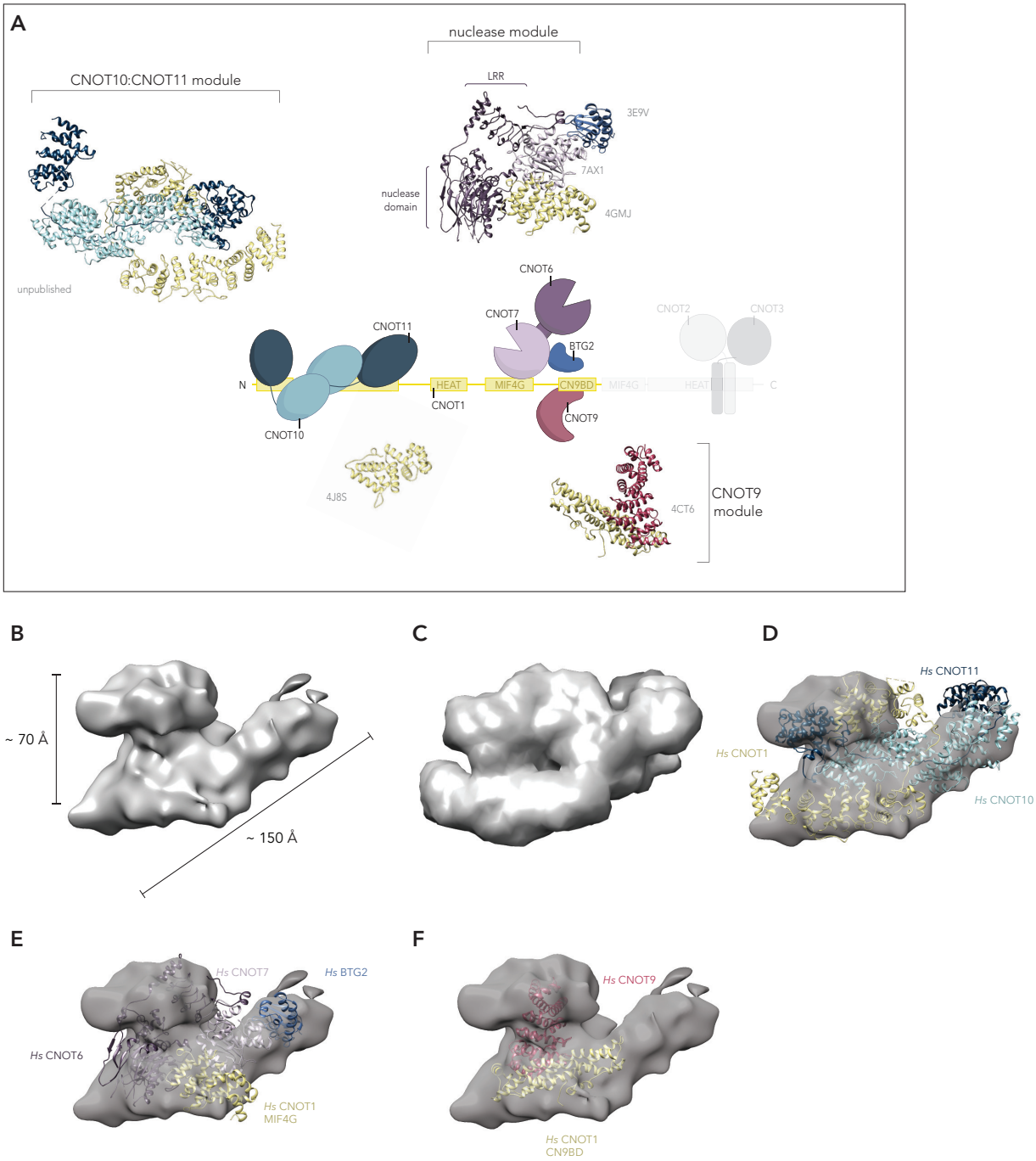

Figure 4.8. Possible interpretation of the 3D reconstruction of Ccr4-Not$_{\Delta C}$:BTG2. A, Schematic representation of Ccr4-Not$_{\Delta C}$:BTG2 complex with available atomic models of the CNOT1$_{820\text{-}999}$ HEAT domain (PDB:4J8S), the CNOT9 module: CNOT1$_{1352\text{-}1594}$ CN9BD:CNOT9 (PDB:4CT6), a composite model of the nuclease module: CNOT1$_{1093\text{-}1317}$ MIF4G (PDB:4GMJ), human CNOT6:CNOT7 (PDB:7AX1), CNOT7:Tob(PBD:2D5R), and BTG2 (PDB:3EV9), and the CNOT10:CNOT11-module (unpublished): CNOT1$_{1\text{-}662}$:CNOT10:CNOT11 in cartoon representation. Domains of CNOT1 are highlighted in pale yellow, CNOT6 in dark purple, CNOT7 in light purple, CNOT9 in dark red, CNOT10 in light blue, CNOT11 in dark blue and BTG2 in blue. **D, E,F** Rigid-body fitting of simulated maps of atomic models of the modules in the 3D reconstruction (**B**) from a cryo-EM dataset of vitrified Ccr4-Not$_{\Delta C}$:BTG2 complex using UCSF chimera. While the simulated map (**C**) of the N-terminal CNOT10:CNOT11 module can be placed relatively clearly in the density (correlation of 0.838) (**D**), the nuclease module (correlation of 0.855) (**E**) and CNOT9 module (correlation of 0.916) (**F**), can be placed in multiple positions in the density.

4.1.3 Ccr4-Not$_{\Delta C}$

Since and co-expression of BTG2 and incomplete cleavage of the SUMO tag of His-SUMO-CNOT7 appeared as a major source for heterogeneity in the sample (ratio cleaved to uncleaved 2:1) the His-3C-CNOT7-3C-CNOT6 fusion construct expressed in Hi5 insect cells as described in 4.1.1 was used to reconstitute the hexameric Ccr4-Not$_{\Delta C}$ complex. The SEC elution profile of the reconstituted complex and the corresponding Coomassie-stained SDS-PAGE (Fig. 4.9 B) show an equimolar stoichiometric complex, that is free of impurity bands and elutes in a single mildly tailing peak. Although the homogeneity of the complex was improved, screening of the sample for larger and more homogeneous particles in negative staining and cryo-EM under different conditions did not reveal significant differences compared to Ccr4-Not$_{\Delta C}$:BTG2 (data not shown). Most of the complex disintegrated during sample preparation for cryo-EM and therefore no high-resolution 3D reconstruction could be obtained. Since the two smaller subcomplexes Ccr4-Not$_{CORE}$ and Ccr4-Not$_{\Delta C}$ behaved similarly unstable in cryo-EM, the next step was to express and purify all subunits in full-length, thus potentially stabilizing the complex.

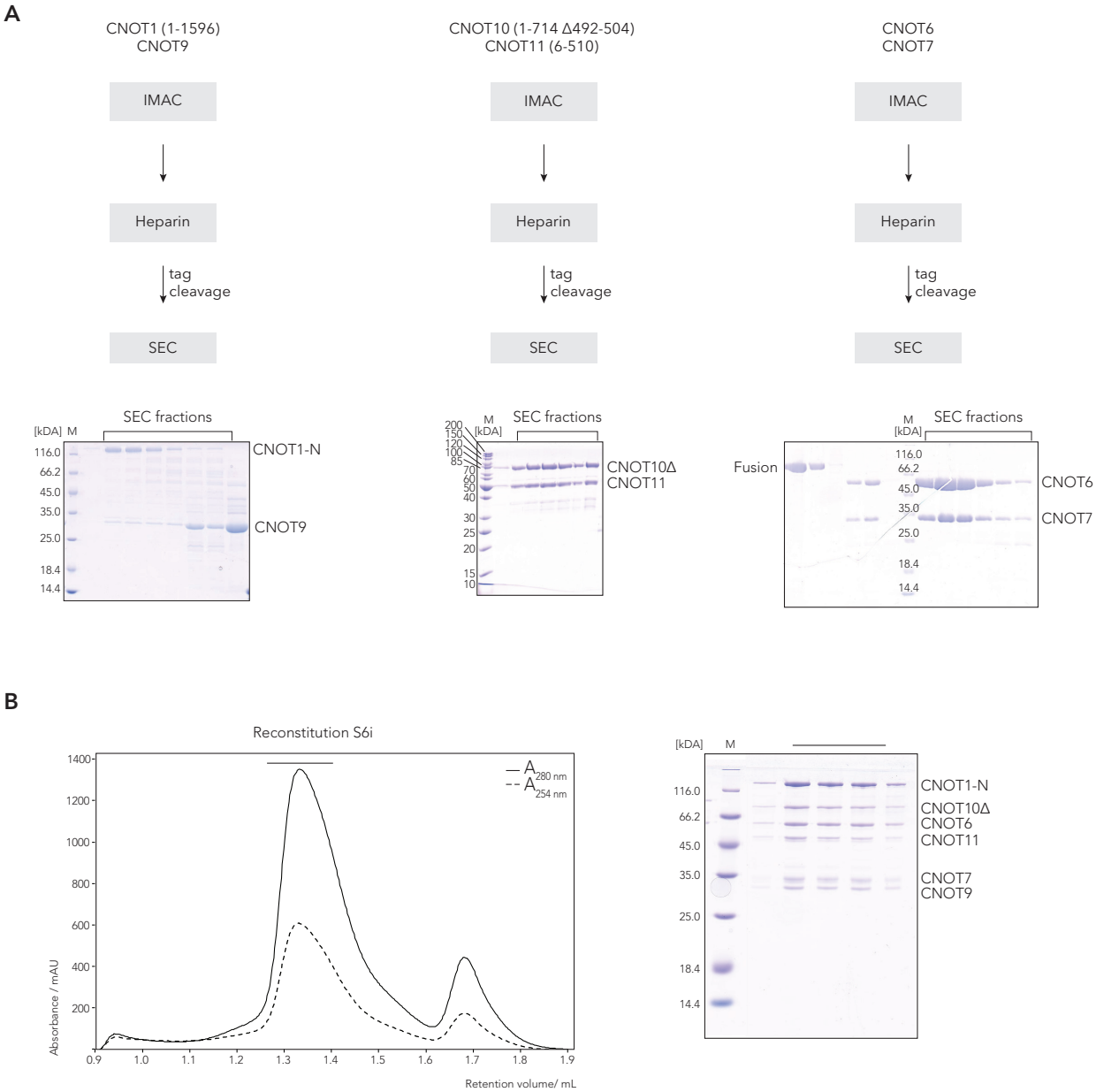

Figure 4.9. Reconstitution of Ccr4-Not$_{\Delta C}$ complex. **A,** Purification of CNOT1-N (1-1596):CNOT9, CNOT10Δ (1-714 Δ492-504): CNOT11 (6-510), and CNOT6:CNOT7 subcomplexes. Coomassie-stained SDS-PAGE analyses show the last step of each purification. **B,** Left, SEC elution profile of the reconstituted Ccr4-Not$_{\Delta C}$ complex. Right, Corresponding Coomassie-stained SDS-PAGE of the purified recombinant subcomplexes CNOT1-N:CNOT9, CNOT10Δ:CNOT11, CNOT6:CNOT7, as well as the reconstituted complex.

4.2 Purification of full-length Ccr4-Not complex

4.2.1 Expressions of subcomplexes from insect cells

To reconstitute the full Ccr4-Not complex, the scaffold protein CNOT1 is crucial because all other modules dock to it. The full-length version of ∼260 kDa protein was expressed in bacteria and insect cells, but SDS-PAGE analysis showed low yields and strong degradation (data not shown). Large amounts of shorter, partially degraded CNOT1 lead to the presence of multiple different subcomplexes because the other subunits can still bind to shorter versions. Therefore, strategies to reduce degradation and stabilize CNOT1 were tried. To prevent degradation, various constructs with different affinity tags on both termini were cloned and tested for expression in insect cells. A construct with an N-terminal His-TEV-tag and a C-terminal 3C-MBP-tag, expressed in Hi5 insect cells showed the best yields and low amounts of degradation. To further stabilize CNOT1, co-expression with various subunits of the complex in insect cells was tested by titrating the respective P2 viruses into the same expression flask (see Fig. 4.10). The test expression with subsequent pull-down experiments of His-tagged proteins revealed when CNOT1 was co-expressed with full-length CNOT2 and CNOT3, the C-terminal MBP-tag showed no difference in expression (see Fig. 4.10 C) and therefore from that point on the CNOT1 construct without MBP tag was used. The addition of further subunits or subcomplexes to one expression, did not significantly change the yield of CNOT1, but the amounts of the other proteins were comparably low, so that the original expression strategies of co-expressing CNOT10:CNOT11, and CNOT6:CNOT7 (CNOT6M:CNOT7M) respectively were retained (see Fig. 4.10 D, E). Due to purity and yields, CNOT9 was still used from *E. coli* expressions.

The Ccr4-Not complex reconstituted from co-expressed subcomplexes eluted in a single, symmetric peak in the second SEC run after the excess of subcomplexes was removed in the first SEC run. Previous problems with concentration and proteolytic degradation of

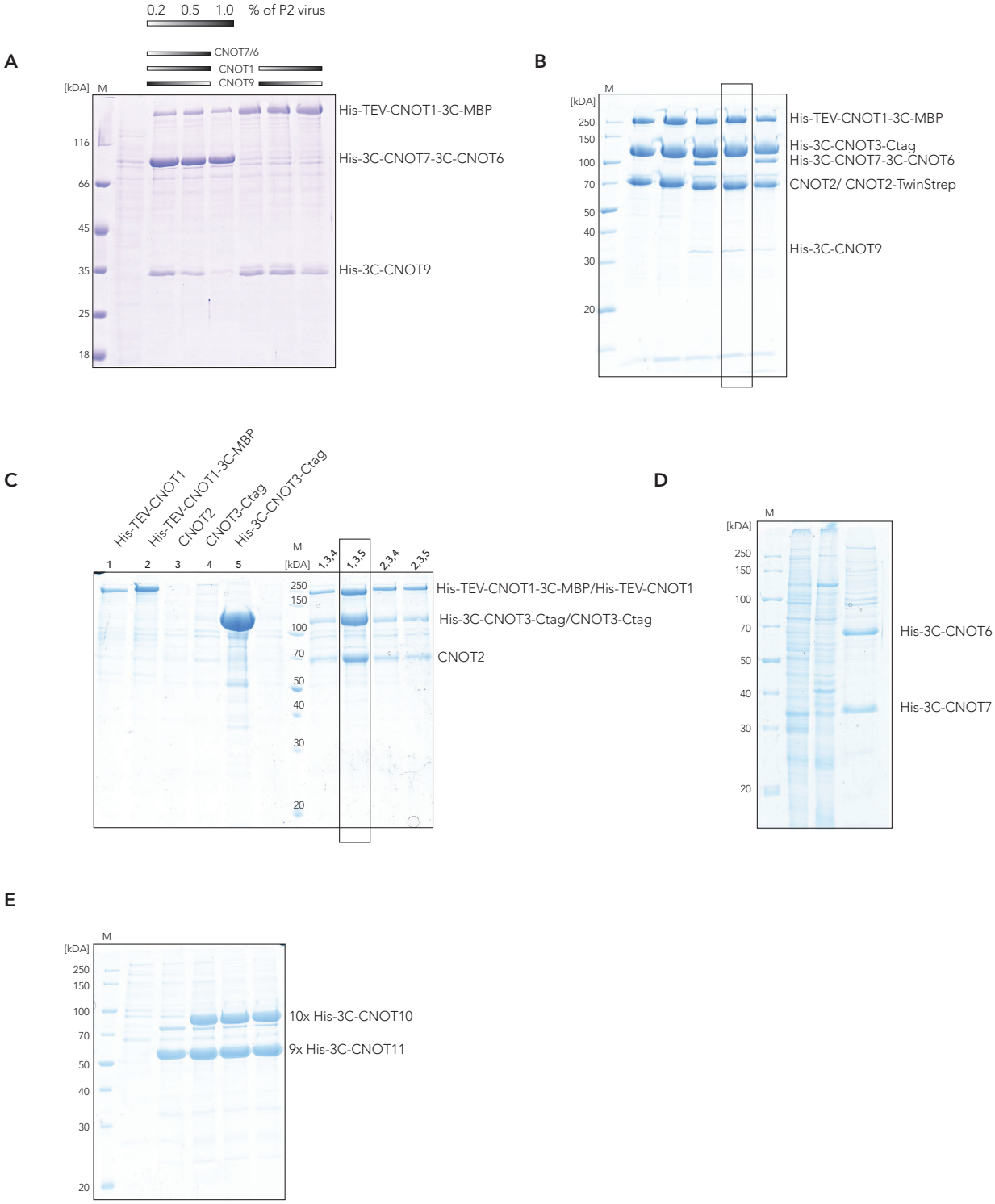

Figure 4.10. Co-expression of Ccr4-Not subunits in insect cells. A-E, Coomassie-stained SDS-PAGE analyses of pull-down experiments of His-tagged proteins of 25 mL (10 mL in **D**) test expressions in High Five cells. **A,** The white-grey gradient is indicating increasing amounts (0.2 %, 0.5 %, 1 %) of used P2 virus. **B, C,** Rectangular boxes indicate the chosen conditions, used for further expressions.

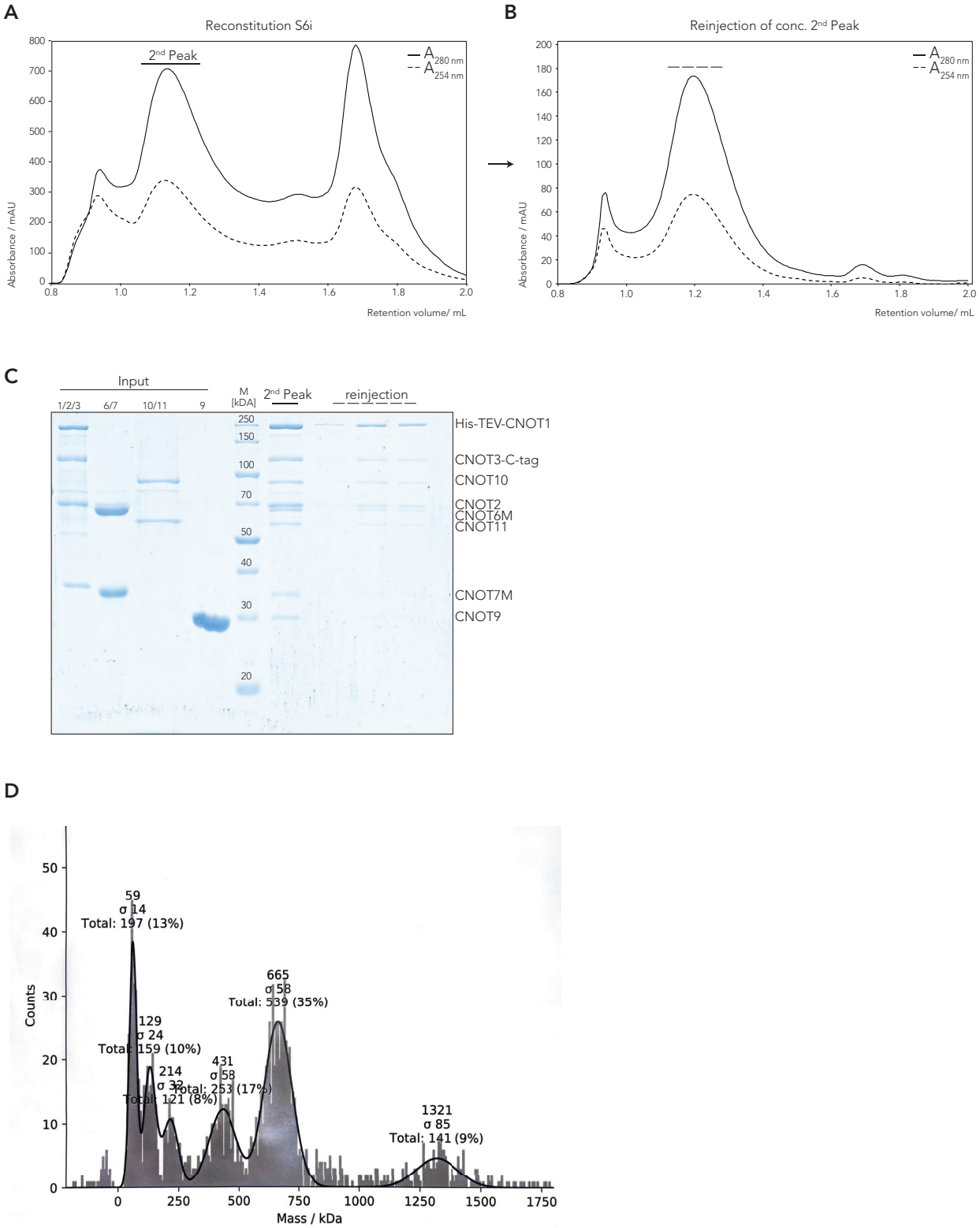

Figure 4.11. Reconstitution of the full Ccr4-Not complex. A, Representative SEC elution profile of the reconstituted Ccr4-Not complex. The second peak was concentrated and reinjected. The corresponding SEC elution profile is shown in **B**. **C,** Coomassie-stained SDS-PAGE of the purified recombinant subcomplexes CNOT1:CNOT2:CNOT3, CNOT6M:CNOT7M, CNOT10:CNOT11, and CNOT9 as well as the reconstituted complex after SEC shown in **A, B**. **D,** The sample was subjected to mass photometry after gelfiltration. The histogram shows, that the sample is composed of several subcomplexes.

CNOT1 were resolved. Although SDS-PAGE analysis indicated a stoichiometric complex (see Fig. 4.11), screening in negative staining and cryo-EM showed strong heterogeneity of particles. This was independent of the method of complex reconstitution (gel filtration, density gradient ultracentrifugation, or pull-down - data not shown).

To better understand the heterogeneity of the particles in EM, the composition of the sample after reconstitution by SEC was investigated using mass photometry (MP). MP is based on interference reflection microscopy. A 20 µL drop of protein or protein complexes (∼30 nM) in solution is placed on a coverslip on a microscope objective, and a camera records the naturally occurring adsorption and desorption events of the molecules. The interference of the light scattered by adsorbed molecules and the light reflected by the surface and correlates directly with molecular mass (Young *et al.*, 2018; Sonn-Segev *et al.*, 2020). The method has been shown to provide useful information on the composition of the sample under native conditions with minimal amounts of sample (Sonn-Segev *et al.*, 2020).

The histogram of the peak fraction of the SEC of the full Ccr4-Not complex (Fig. 4.11 D) showed a mixture of subcomplexes of different molecular weights, with only about 35 % representing the full complex of 665 kDa, consistent with the heterogeneity of the particles observed of the sample in electron microscopy (data not shown). To overcome this apparent heterogeneity in size, a new strategy was employed, in which all subunits were co-expressed together and purified in two consecutive pull-downs of subunits from both ends of the Ccr4-Not complex to ensure that all subunits were present. Co-expression has also the advantage of higher reproducibility, as titration of different viruses for expression in insect cells introduces some variability in each expression, as the lifespan and strength of each virus varies. On top, purification of multiple subcomplexes is more time-consuming and minor modifications can add up with many purification steps.

4.2.2 Co-expressions of the full-length proteins from insect cells

Several systems for insect cells were tested to co-express and purify all subunits simultaneously. While test expressions of the complex using the MultiBac system (Sari *et al.*, 2016) showed low yields and still degradation of CNOT1, in test expressions using the GoldenBac (Neuhold *et al.*, 2020) system, not all subunits appeared to be expressed (data not shown).

Up to 25 cDNAs can be assembled into one vector for expression in insect cells using the biGBac system (Weissmann *et al.*, 2016). To achieve this, the cDNAs of interest are cloned into pLIB vectors containing an expression cassette with a polyhedrin promotor. The cassettes are then amplified by PCR with specific linker sequences and up to five cassettes are assembled using Gibson assembly (Gibson *et al.*, 2009) with a pBIG1 vector. In a second step, the poly gene cassettes of the pBIG1 vectors are excised by PmeI digestion and assembled into pBIG2 vectors via Gibson assembly.

For the Ccr4-Not complex, four subunits were cloned into each of the vectors pBIG1a and pBIG1b (Fig. 4.12). His-TEV-CNOT1, CNOT2, CNOT3-C-tag, and CNOT9 were cloned into pBIG1a. CNOT10, CNOT11-TwinStrep, CNOT6 (or CNOT6M), and CNOT7 (or CNOT7M) were cloned into pBIG1b. The combination of which subunits were cloned together was based on results from the previously described co-expression experiments. The affinity tags were chosen so that purification of the complex could be performed in two consecutive pull-downs from both ends of the complex. Thus, CNOT11, which binds to the N-terminus of scaffold protein CNOT1, was cloned with a C-terminal TwinStrep-tag, and CNOT3, which binds to the C-terminus of CNOT1, was C-terminally tagged with a C-tag. Combinations of cassettes with the active forms of the two nucleases or active site mutants were then assembled via Gibson assembly into pBIG2ab vectors. After generation of a baculovirus, Hi5 cells were infected.

The purification steps are described in detail in 3.3. After an initial affinity chromatog-

raphy step over a StrepTactin column including a high-salt wash with a buffer containing 1 M NaCl, all eight subunits were present in good amounts (yields of 30 mg per liter of insect cell culture) and with only minor impurities. The complex was frozen and stored after that step. Depending on the follow-up experiments, the complex was further purified via SEC or C-tag pull-down. Coomassie-stained SDS-PAGE analysis suggests that both methods purify a stoichiometric Ccr4-Not in sufficient yields with only minor impurities (see Fig. 4.13 B, C). The complex was aliquoted into lobind tubes, spiked with 5 % of glycerol, flash-frozen, and stored at -80 °C for structural and biochemical experiments. To ensure that the 1M salt elution in the C-tag pull-down did not affect the composition of the complex, both elution fractions (2 mM peptide and 1 M NaCl) were compared in MP measurements. The histograms (Fig. 4.13 D) look very similar with the majority (81 % and 84 %) of particles of a molecular weight around 630 kDa. The theoretical MW of the full Ccr4-Not is 681.9 kDa, but the precision of the MP weight determination depends on the accuracy of the calibration. The presence of all subunits was confirmed by mass-spectrometry data. The co-expression and purification strategy appears superior to the *in vitro* assembly. It yields a reconstituted human Ccr4-Not complex with significant improvement in homogeneity and purity if compared to the strategy presented in 4.11.

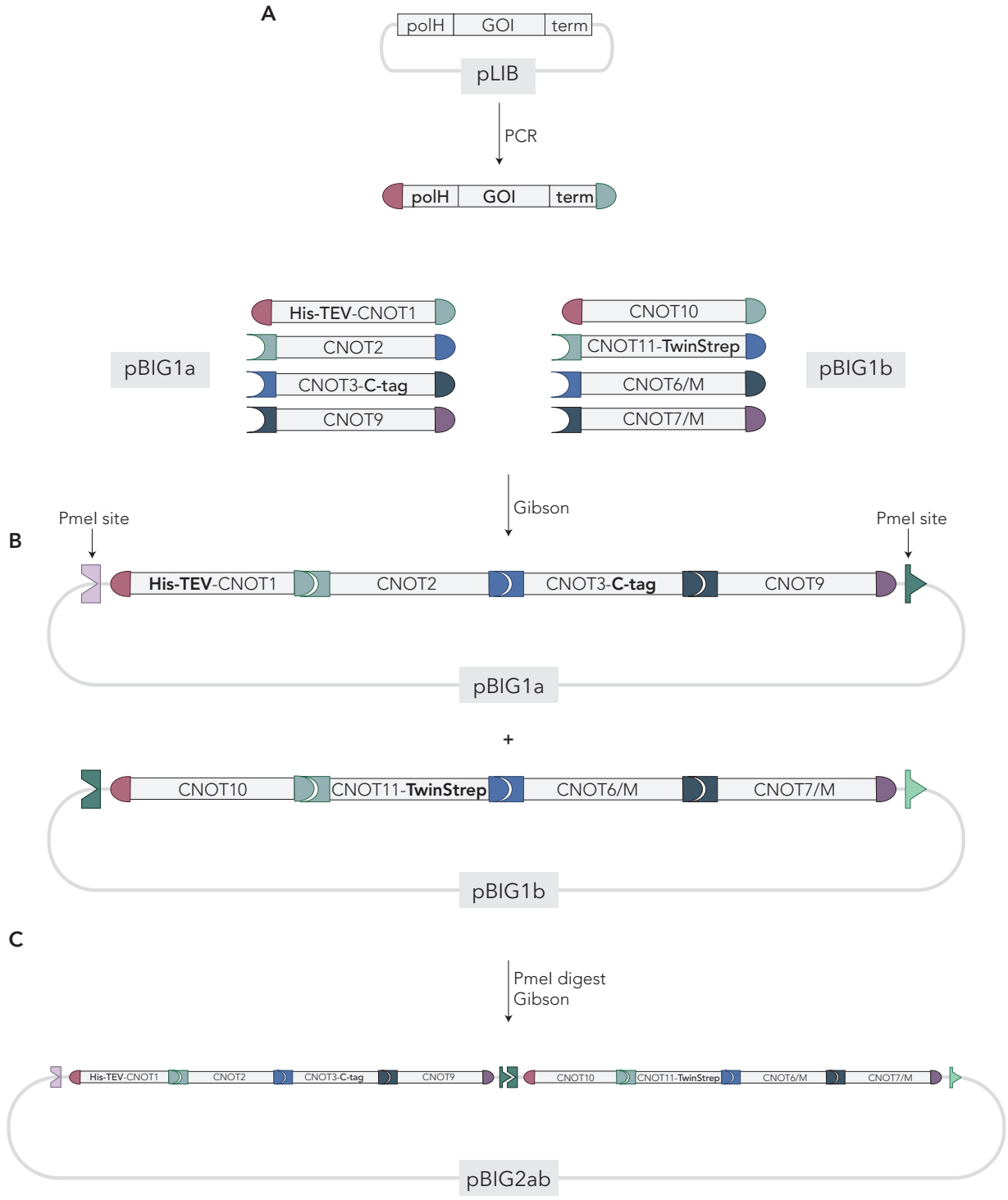

Figure 4.12. Overview of biGBac assembly process. Schematic representation of biGBac assembly procedure with subunits of Ccr4-Not adapted from (Weissmann *et al.*, 2016). **A,** In the first step, cDNAs are cloned into pLIB vectors containing a polyhedrin promotor (polH). The cassettes are then amplified by PCR with specific linker sequences (depicted by color-matching objects). **B,** The cassettes are assembled into one pBIG1 vector using Gibson. **C,** The poly gene cassettes are excised by PmeI digest and assembled using Gibson assembly into a pBIG2 vector.

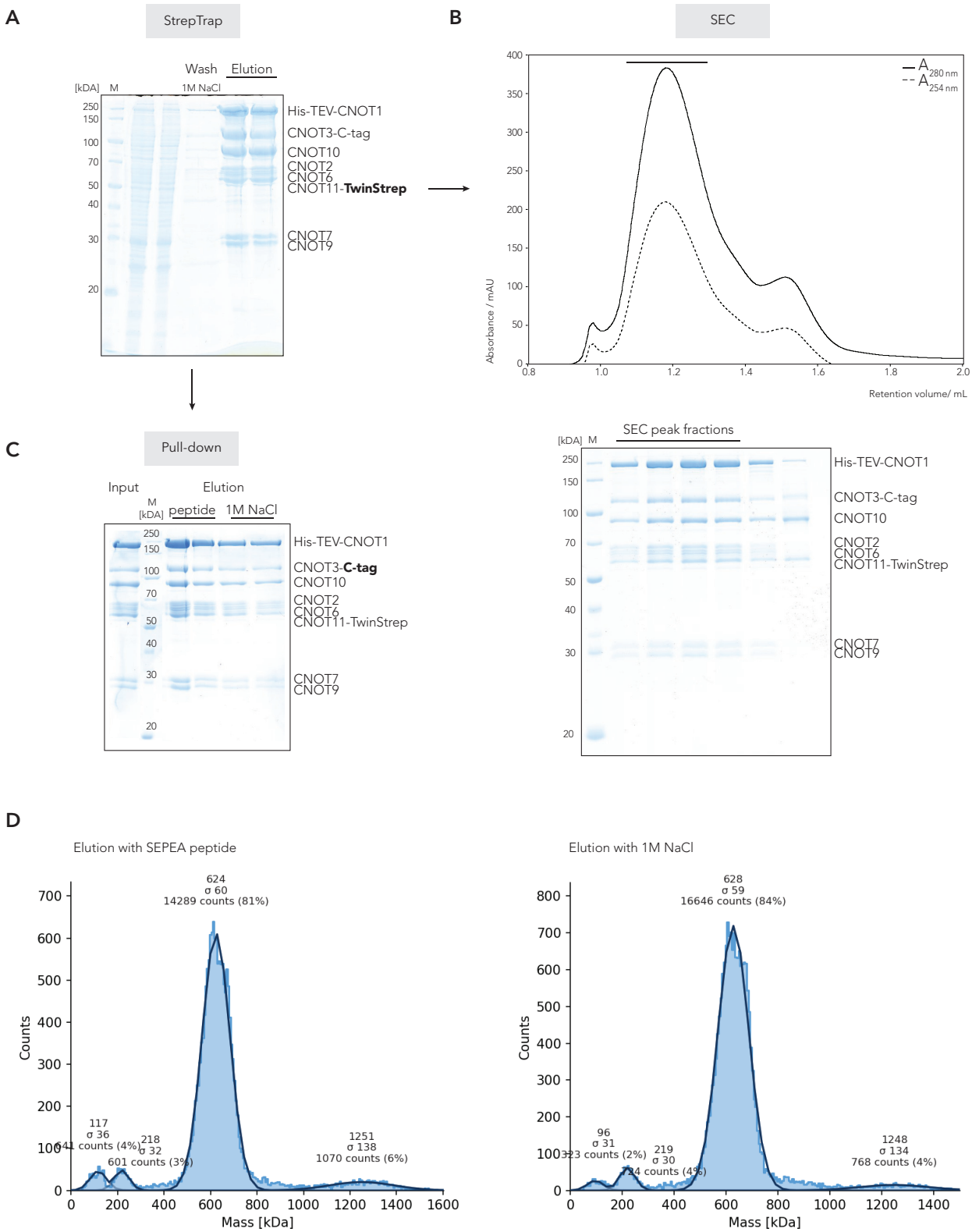

Figure 4.13. Purification scheme of a Ccr4-Not complex co-expressed in insect cells. A, Coomassie-stained SDS-PAGE of the first purification step: the Ccr4-Not complex is bound to Strep-Tactin by a TwinStrep tag on the C-terminus of CNOT11. **B,** Representative SEC elution profile of the complex after StrepTactin elution. The corresponding Coomassie-stained SDS-PAGE analysis is shown below. **C,** Coomassie-stained SDS-PAGE analysis of a pull-down experiment of C-tag tagged CNOT3 as final purification step. **D,** Histograms of MP measurements to compare pull-down elutions with different compositions of elution buffers. Left, Elution with 2 mM SEPEA peptide. Right, elution with 1 M NaCl.

Cryo-EM studies of the full-length Ccr4-Not complex

Initial screenings of the sample in EM also showed a mixture of particles of different sizes. Since the sample in solution consists of up to 84 % of the intact complex, it is possible that the complex disintegrates at the air-water interface, as was the case with the smaller partial complexes (data not shown). However, in contrast to the smaller partial complexes, testing different freezing conditions using detergents and cross-linkers such as BS^3 or glutaraldehyde resulted in a higher number of intact complexes on grids with additional support film and the detergent β-OG. The sample for the final dataset was purified as described in 4.2.2, 0.04 % (v/v) of β-OG was added, and vitrified on a R2/1 holy carbon grid with an additional layer of 2 nm carbon support film. A large dataset of 17,803 movies was acquired on a Titan Krios microscope equipped with a K3 direct electron detector and operating at 300 keV. As can be seen in Fig. 4.14 A, particles are identifiable, despite some aggregation, but the size of the individual particles is difficult to assess due to poor signal-to-noise ratio (SNR) caused by the additional carbon layer. Details of sample preparation, data acquisition, and processing are described in 3.5 and shown in Fig. 4.14. Data processing followed a two-way strategy, using the Topaz picker integrated into the cryoSPARC processing suite, to improve particle picking. After manual selection of a small subset of particles and initial cleaning and classification the particles were used to train the Topaz picker. The particles extracted by Topaz extract were subjected to reference-free 2D classification in subsets and the coordinates of the cleaned stacks were then exported to RELION 3.0 for further 2D classification. The resulting 2D class averages (Fig. 4.14 B) of 2-times binned particles are similar in size but differ in composition or conformation. The classes are still blurred, but some higher resolution details are resolved. However, after re-extracting the particles with the original pixel size and performing another 2D classification, the resulting 2D class averages were blurrier and high-resolution details were no longer visible. Binning or down-sampling of the data is done by Fourier cropping, which

removes the signal above a certain frequency in reciprocal space, increasing SNR at low resolution and limiting noise at high resolution, making it easier to find the correct alignments. The lower SNR after re-extraction therefore made it difficult to align the particles correctly. To increase the SNR by the number of particles, the 2D class averages were used as templates for template-picking in Gautomatch. About 3.9 million initial particle candidates were picked and cleaned up by several rounds of 2D classification and then subjected to several rounds of 3D classification. The resulting 3D reconstructions (Fig. 4.14) show both classes of slightly expanded and more compact shape. Both shapes (indicated by the dashed rectangle) were selected and subclassified individually. The particles of the classes with the highest occupancy and resolution were selected, pooled, and subjected to a further round of 3D classification with a soft-edged mask. The best two of the resulting 3D reconstructions were selected and the particles were re-extracted with the original pixel size of 1.094 Å/px. The particles were then subjected to a final 3D classification resulting in the four classes shown below in the processing scheme. The classes shown were individually subjected to 3D auto-refinements, but the refined 3D reconstructions showed masking artifacts (not shown) with mainly density at the edges of the mask and no density in the center, which could not be overcome by varying mask sizes. This could be due to the even lower SNR, since for the 'gold-standard' FSC the data is split into halves and refined individually. Therefore, the 3D class, indicated by the dashed rectangle, with 22 % occupancy and an estimated resolution of ∼14 Å was used to place the atomic models in (see Fig. 4.16).

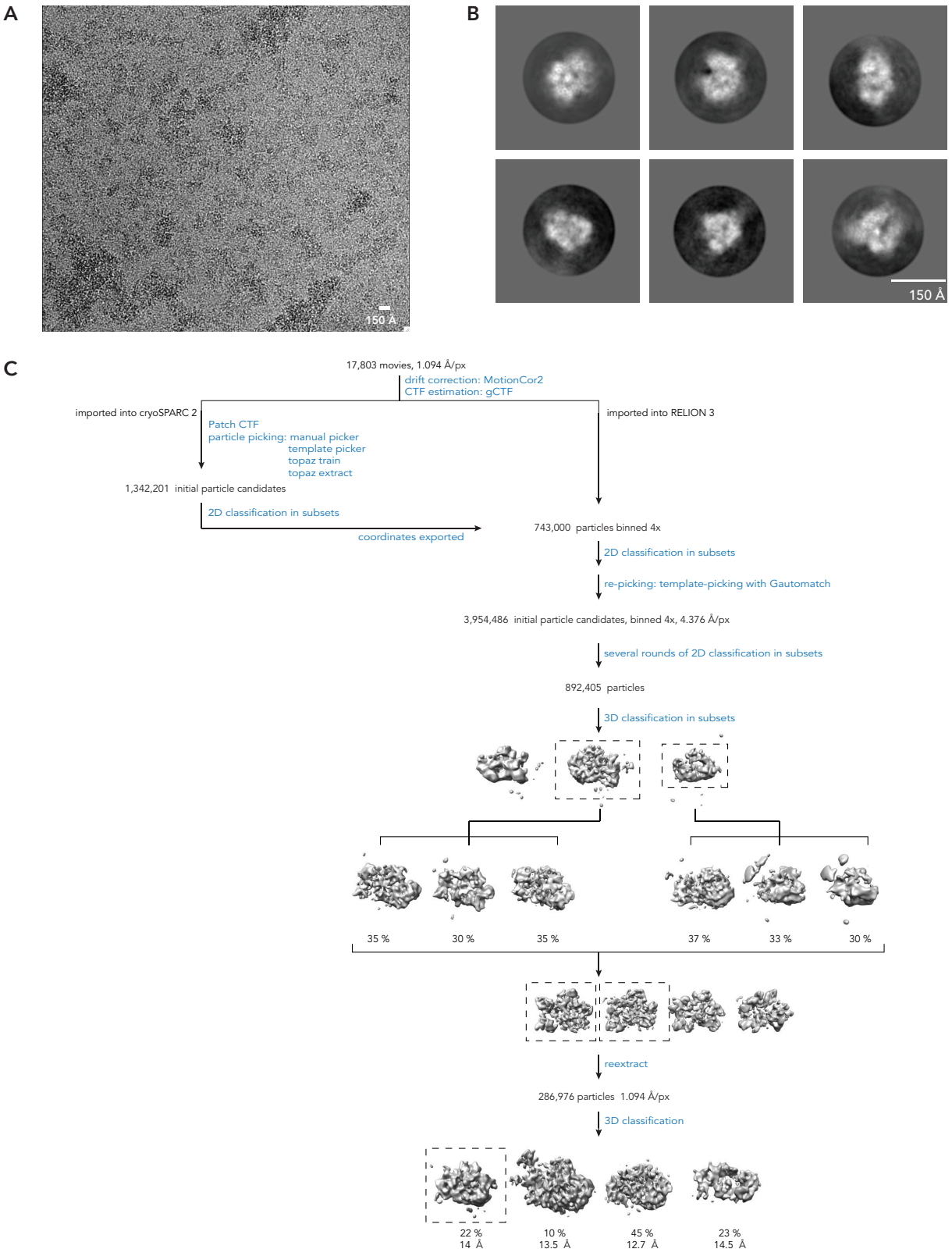

Figure 4.14. Cryo-electron microscopy of vitrified full-length Ccr4-Not complex. A, Micrograph of purified full-length Ccr4-Not complex, vitrified on a Cu200 R2/1 holey carbon grid with 2 nM carbon film, acquired on a Titan Krios electron microscope, operating at 300 keV, equipped with a K3 direct detector and a post-column energy filter. **B,** Representative 2D class averages derived from reference-free 2D classification in RELION 3.0. Box size 192 pixels. Scalebars indicate 150 Å. **C,** Processing strategy.

Analysis of 3D reconstruction

The selected 3D reconstruction from the final 3D classification is shown in Fig. 4.16 A. It has a kind of triangular shape with dimensions of ∼120 Å to ∼190 Å. Since the resolution achieved was not sufficient to clearly assign the available atomic models, cross-linking mass spectrometry (XL-MS) analysis was used to obtain more information about the structural proximity of individual subunits. The sample for XL-MS was purified as previously described in a two-step procedure of StrepTactin affinity chromatography and C-tag pull-down. The elution from the C-tag beads was carried out under high-salt conditions, because the SEPEA peptide would interfere with the cross-linking reagent in the subsequent chemical cross-linking reaction, as BS^3 reacts mainly with primary amines (lysine residues and N-termini of proteins). After a titration with increasing amounts of cross-linker (Fig. 4.15 A), the condition (1 mM BS^3 for 10 min on ice) at which both the cross-linked complex and individual subunits were visible in a good ratio to prevent over cross-linking was chosen. The identified cross-links were mapped to available atomic models (Fig. 4.15, A) using the Xlink Analyzer (Kosinski *et al.*, 2015) software tool in UCSF chimera. Of 227 identified inter- and intra-cross-links, 103 could be mapped (see Figure 4.15 B); the remaining cross-links were between residues absent in the crystal structures. The BS^3 cross-linker has a spacer length of 11.4 Å, which, together with the length of the lysine side chains, allows a theoretical distance of C_α - C_α of up to 24 Å. However, experimental data from known structures actually showed longer distances, probably due to dynamics of lysine residues and backbone (Merkley *et al.*, 2014). Therefore, an additional tolerance of ∼3-6 Å is usually used, resulting in a total permissible distance of 30 Å, which was also used as the threshold in this study. The red lines in Fig. 4.15 D, E show the identified cross-links that violate the threshold, whereas the blue lines indicate cross-links within the specified range of 30 Å. Several cross-links between subcomplexes are mutually exclusive, indicating alternative conformations and confirming the flexibility of the complex observed in previous

cryo-EM data sets. After filtering the cross-links by cross-link confidence scores greater than 90, the remaining 24 cross-links (∼10 % of all inter- and intra-cross-links) were used to create a possible model to fit into the 3D reconstruction from the cryo-EM dataset. The nuclease module ($CNOT1_{1093\text{-}1317}$ MIF4G:CNOT6:CNOT7) is positioned according to cross-links with cross-link confidence scores above 55 as none were identified above 90. The model could represent a possible conformation and should only be used as an initial guide to the global architecture of the assembly. A simulated map of the model fits into the 3D reconstruction with a correlation of 0. 872 as shown in the rigid-body fit shown in Fig. 4.16, B, suggesting that likely all subunits are present but in different conformations. In contrast to the smaller subcomplexes described above, at least the majority of the particles appear to represent the full complex, which does not disintegrate. This is likely due to a stabilizing effect, as all subunits are expressed together and in full-length. On top, the carbon support film pulling the complex away from the air-water interface.

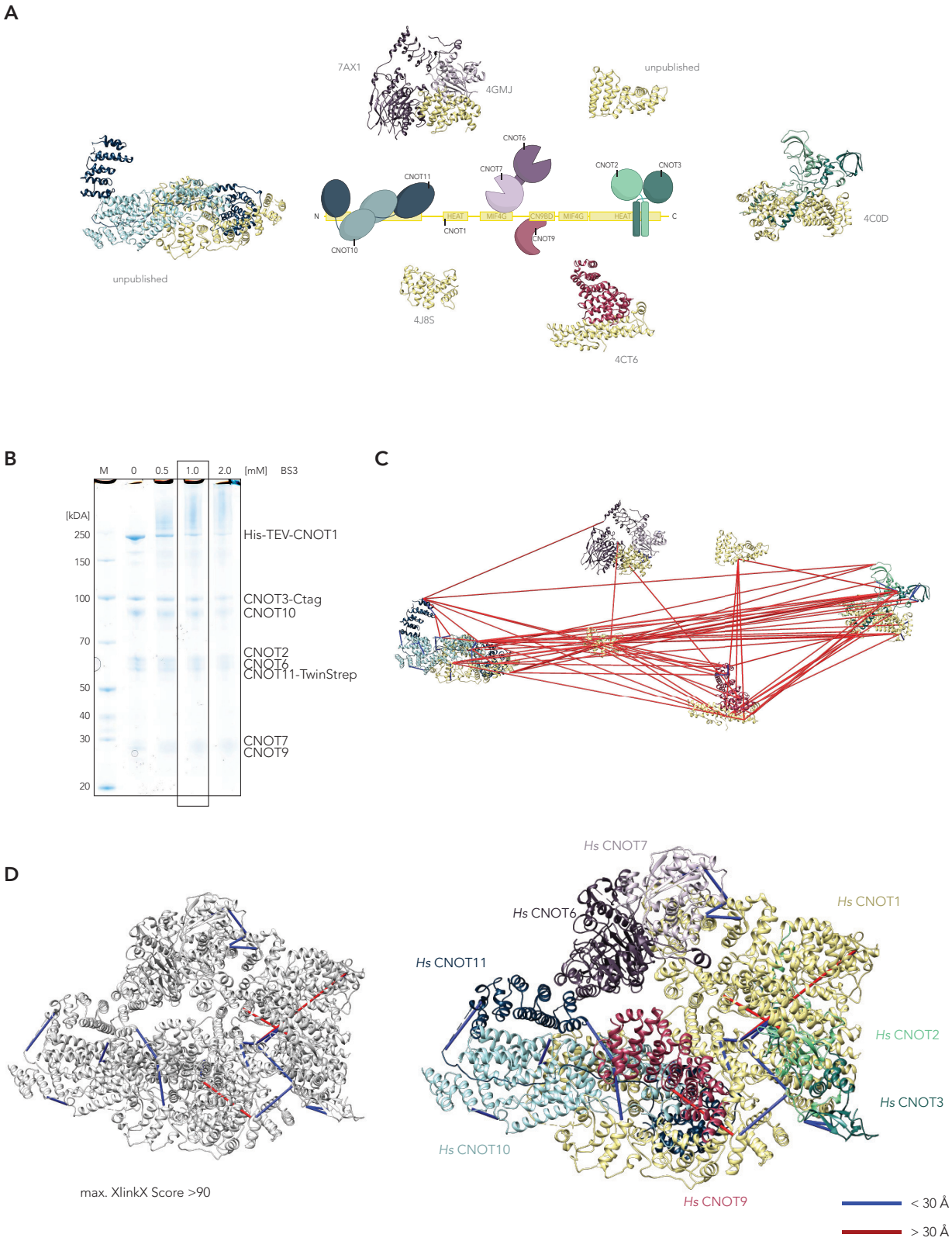

Figure 4.15. Cross-linking mass spectrometry of Ccr4-Not. A, Schematic representation of Ccr4-Not complex architecture with the corresponding available atomic models of subunits or subcomplexes in cartoon representation. The nuclease module is a composite model of PDB 7AX1 and 4GMJ. **B,** SDS-PAGE analysis of titration experiment with increasing amounts of BS^3 cross-linker after 10 min incubation on ice. **C,** XL-MS data mapped on atomic models from (**A**) using Xlink Analyzer (Kosinski *et al.*, 2015) in Chimera. **D, left,** Composite model of Ccr4-Not built up from crystal structures positioned based on cross-linking data filtered for cross-link confidence scores higher 90 except the nuclease module, which is positioned based on cross-link confidence scores over 55. **D, right,** the model with individual proteins coloured for improved visibility. Blue lines indicate distances below the 30 Å threshold, red lines indicate distances above 30 Å.

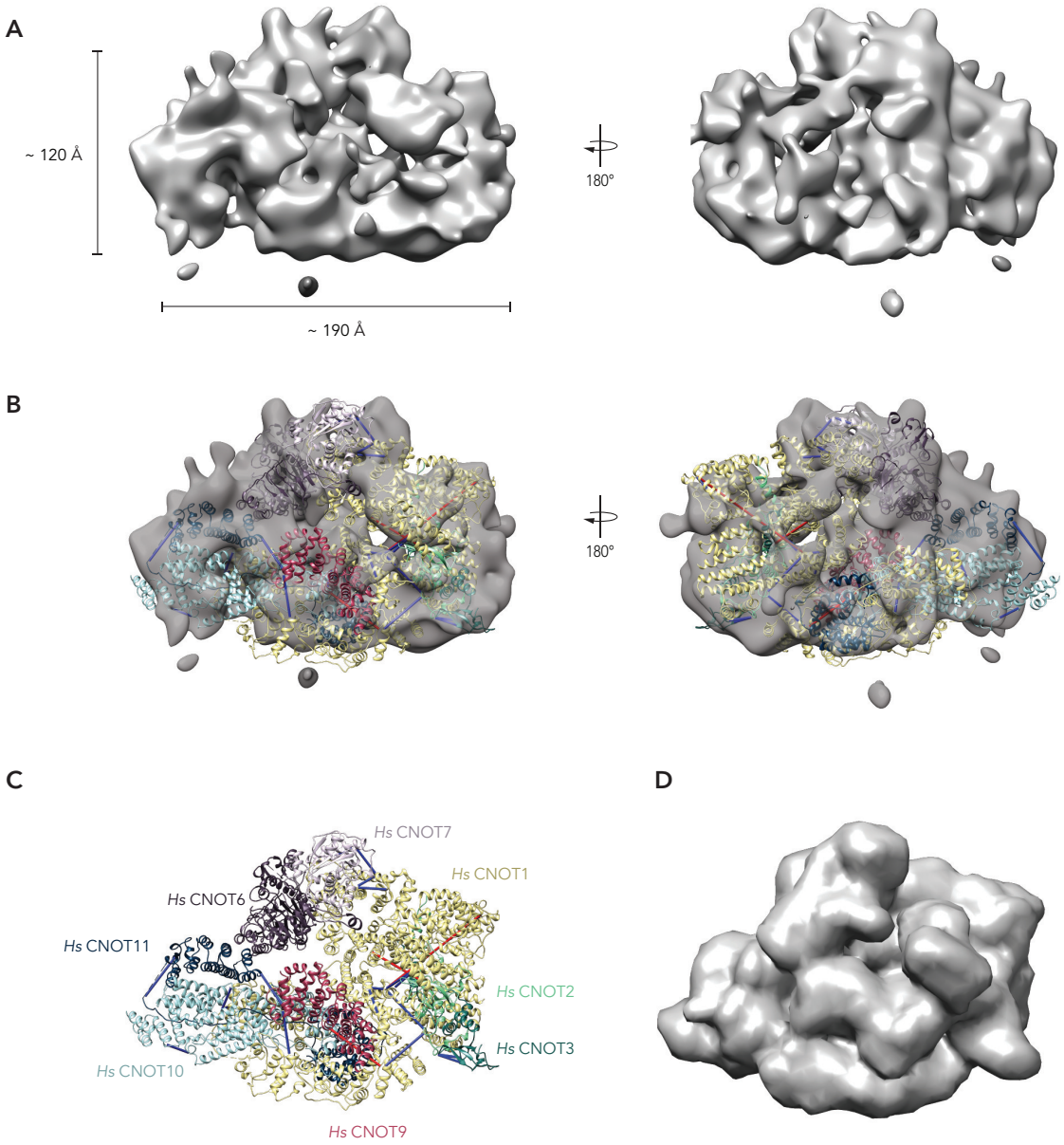

Figure 4.16. Rigid-body fitting of Ccr4-Not complex. A, The 3D reconstruction from the Titan Krios dataset of the Ccr4-Not complex with dimensions of ∼120 to ∼190 Å. **B,** A simulated map of the composite atomic model (**D**) from 4.15 D can be positioned in the density with a correlation of 0.872. **C,** Composite model from 4.15 D based on XL-MS data. **D,** Simulated map at 15 Å of composite model, that was fitted into the EM 3D reconstruction with a correlation of 0.872.

.

However, the complex appears very flexible, in part due to long loops connecting the folded domains of CNOT1, as confirmed by XL-MS data and structure prediction tools. The

large data set was collected to counteract the problems caused by flexibility due to fewer particles per conformation. However, the poor SNR hampered the ability to separate the conformations and thereby limiting the overall resolution. Subsequent attempts to resolve the structure therefore consisted of finding a cofactor and/or substrate that would stabilize the complex in a particular conformation, making it more suitable for cryo-EM.

4.3 Ccr4-Not and ARE-binding protein TTP

By its very nature, the Ccr4-Not complex has a variety of interactors, mainly RBPs, that recruit the complex to its mRNA targets. To stabilize the complex in a distinct conformation, the tandem zinc finger protein TTP was chosen because it is known to bind specifically to ARE-containing transcripts as well as to several sites of the Ccr4-Not complex that are well characterized (Fabian *et al.*, 2013; Bulbrook *et al.*, 2018).

Full-length TTP was cloned with different N- and C-terminal affinity tags, as it has a central tandem zinc finger domain but the N- and C-termini are considered as low-complexity regions (see Fig. 1.4). It was recombinantly expressed in bacteria because TTP is highly regulated by post-translational modifications and phosphorylation of the CNOT1 interacting motif has been shown to weaken the interaction with Ccr4-Not (Clement *et al.*, 2011; Fabian *et al.*, 2013). The purification strategies for two constructs that differ by their C-terminal tag are shown in Fig. 4.17. The construct with a C-terminal StrepII-tag, was captured on a StrepTactin column in the first step, however SDS-PAGE analysis still showed many degradation bands, which could be separated by a heparin purification step, but was associated with large losses. The resulting TTP protein could not be concentrated using commercial concentrators and was also not stable after cleavage of the N-terminal His-GST-tag. Purifications of a construct with a C-terminal C-tag followed a three-step purification procedure. First, the protein was captured on a HisTrap, then applied to

a heparin column and finally purified in a C-tag pull-down experiment after cleavage of the N-terminal tag. This strategy has the advantage that higher concentrations can be achieved, and TTP was stable after removal of the N-terminal tag. However, some degradation products and the SEPEA peptide were still present, that could cause problems in subsequent experiments.

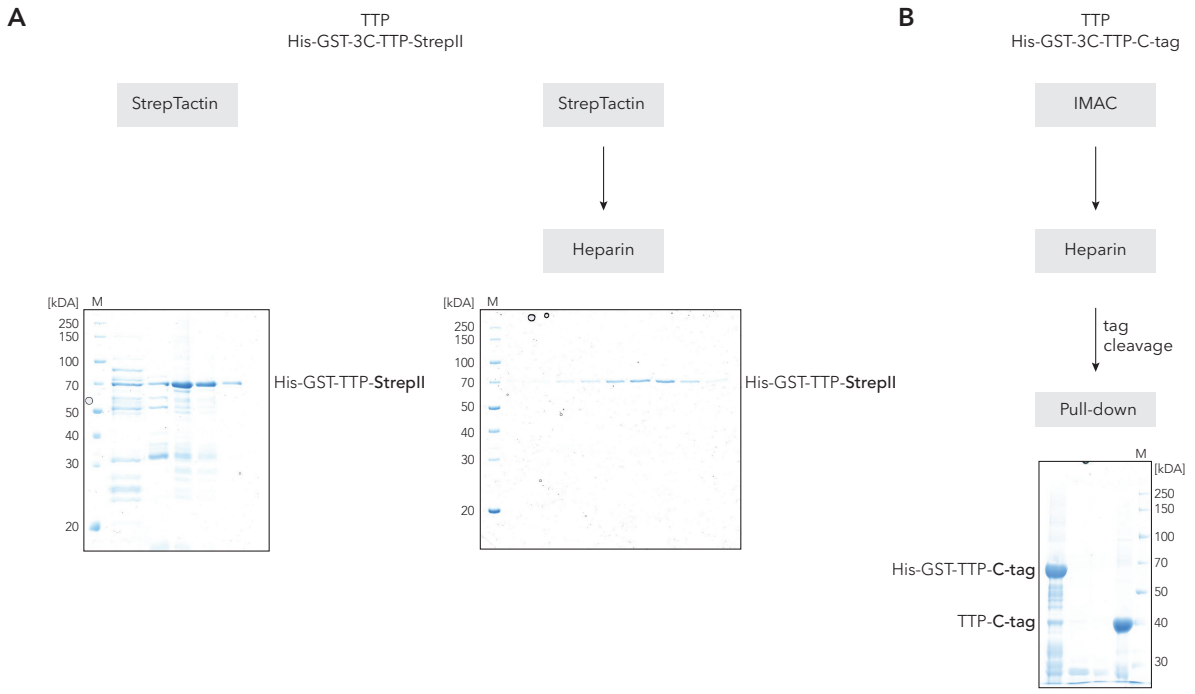

Figure 4.17. Purification scheme of human TTP. Purification strategies of two TTP constructs with differing C-terminal tags. His-GST-3C-TTP-StrepII (**A**), and His-GST-3C-TTP-C-tag (**B**). The Coomassie-stained SDS-PAGE analyses show the last step of the purification, respectively.

Several strategies were tested to reconstitute a stoichiometric Ccr4-Not:TTP complex, each of which had advantages and disadvantages. When the complex was mixed from individually purified subcomplexes, and after incubation with TTP applied to an S6i SEC column, the Ccr4-Not peak shifted and the complex eluted together with TTP already in the void volume (Fig. 4.18 A). Since TTP still had the His-GST tag and offers several binding sites for Ccr4-Not, multimers or aggregates are possible. However, SDS-PAGE analysis showed a stoichiometric complex, CNOT7 and CNOT9 were also present, but because the gel had

been run longer than usual to better separate TTP, CNOT2, and CNOT6, the smaller CNOT7 and CNOT9 had already run out of the gel. The peak fraction of the gelfiltration elution was cross-linked with 1 mM BS^3 for 10 min on ice as previously described and vitrified on an R2/1 grid with additional 2 nm carbon layer. The representative electron micrograph from a small cryo-EM dataset (Fig. 4.18 B) shows particles of different sizes and aggregates as seen previously and also expected from a SEC void peak. The corresponding 2D class averages look very similar to those previously obtained from the large dataset the full-length complex (see Fig. 4.14 B).

Alternative strategies were tested to better separate the reconstituted complex from excess subunits and improve sample homogeneity for structural studies. Ultracentrifugation over a 10-25 % sucrose gradient in the presence of 0.03 % (v/v) of the cross-linker glutaraldehyde (GA), known as GraFix (Kastner *et al.*, 2008)), resulted a distinct band at high molecular weights in the fractions of the gradient corresponding to a stoichiometric Ccr4-Not:TTP complex in the control tube without cross-linker, as shown by SDS-PAGE analysis (Fig. 4.19 A). However, the sample was lost during the necessary concentration process and sucrose removal, as was previously the case for the Ccr4-Not complex without TTP. Therefore, the sample was not examined by electron microscopy and it is not known whether GraFix reduced heterogeneity.

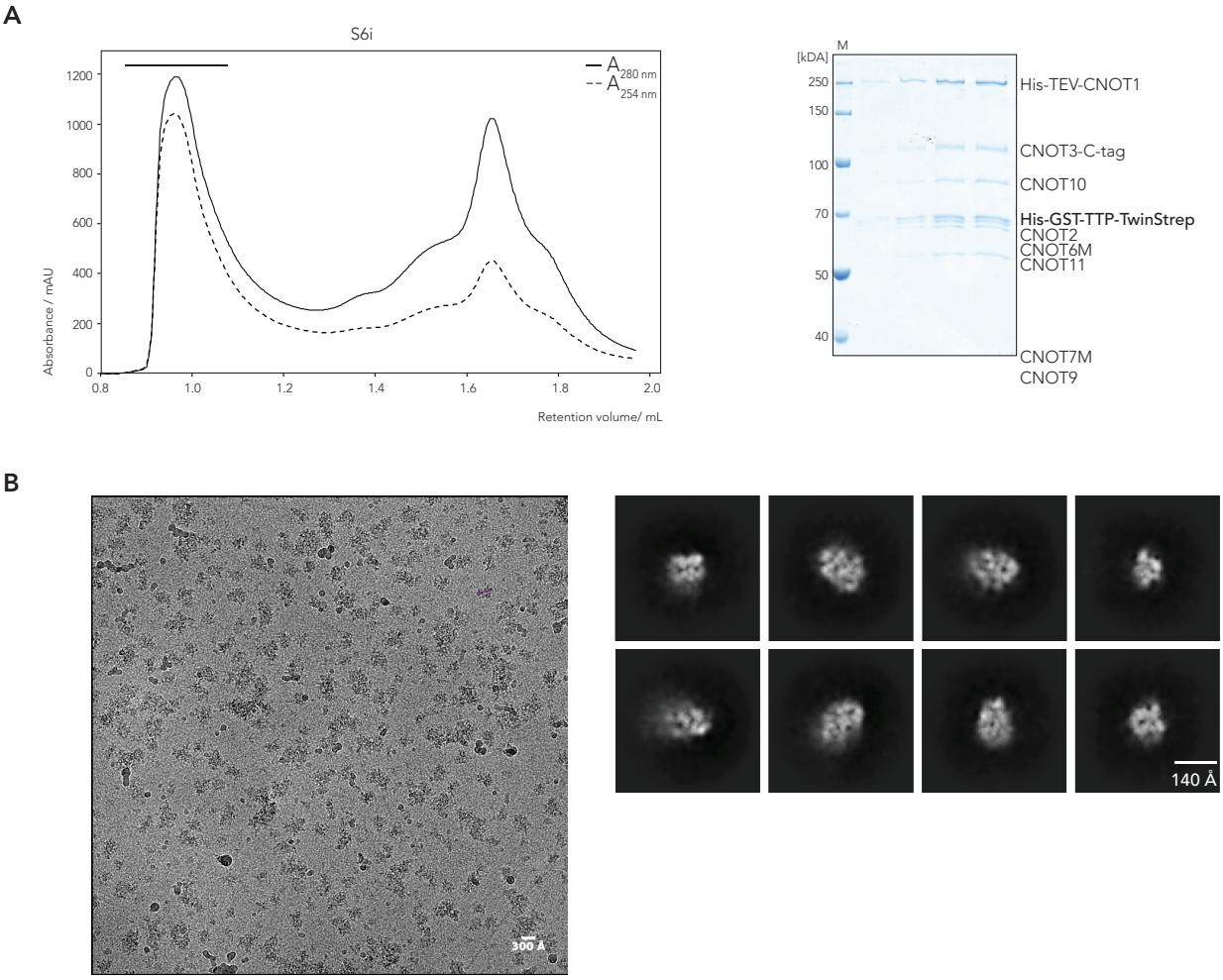

Figure 4.18. Complex formation on S6i. A, left The elution profile of pre-mixed Ccr4-Not:TTP on a S6i column. The formed complex elutes in the void volume. **A, right** The corresponding Coomassie-stained SDS-PAGE analysis shows a stochiometric complex with no visible impurities. **B,** Representative micrograph (left panel) and 2D class averages (right panel) of the Ccr4-Not:TTP dataset, recorded on a Talos Arctica microscope, operated at 200 keV, equipped with a Falcon 3 direct detector at a nominal magnification of 57,000x which corresponds to a pixelsize of 2.53 Å/px. Scalebars indicate 300 and 140 Å.

A home-made column with S6 resin with a larger column volume (∼ 8 mL CV compared to 2.4 mL) achieved better separation from the void peak (Fig. 4.19 B), but the concentrations obtained were only sufficient for negative staining EM (Fig. 4.20 top row). An electron micrograph of the cross-linked sample still shows particles of different sizes. To analyze the composition or heterogeneity of the sample after gel filtration and before cross-

linking, the sample was subjected to MP measurement. MP measurements of a fraction of the gel filtration peak at 0.1 mg/mL (157 nM) (Fig.4.19, D) were diluted to 15 nM immediately before measurement and showed two distinct peaks with 145 kDa (12 %) and 742 kDa (67 %).The peak with 742 kDa probably corresponds to the Ccr4-Not:TTP complex, since its theoretical MW is about 744.5 kDa, and the 145 kDa peak might refer to a CNOT2:CNOT3 subcomplex (theoretical MW of 142 kDa). An additional C-tag pull-down after the longer S6 column (Fig. 4.19 C) apparently did not improve homogeneity as judged by negative stain. Instead, the SEPEA peptide in the elution buffer appeared to coat the negative staining grid, significantly reducing the amount of Ccr4-Not:TTP particles on the grid (Fig. 4.20 bottom row). At high concentrations, the peptide also interfered with the MP measurements, so histograms cannot be interpreted with confidence and are therefore omitted for this particular sample.

Another attempt to increase homogeneity was the incubation with a model substrate RNA prior to cross-linking and negative staining. The RNA used contained a canonical ARE motif (UUAUUUAUU) in a 3'-UTR-like sequence that is recognized by the tandem zinc finger domain of TTP and a downstream poly(A) tail of 30 A, However, this also did not result in visible changes in heterogeneity on negative stain micrographs (Fig. 4.20).

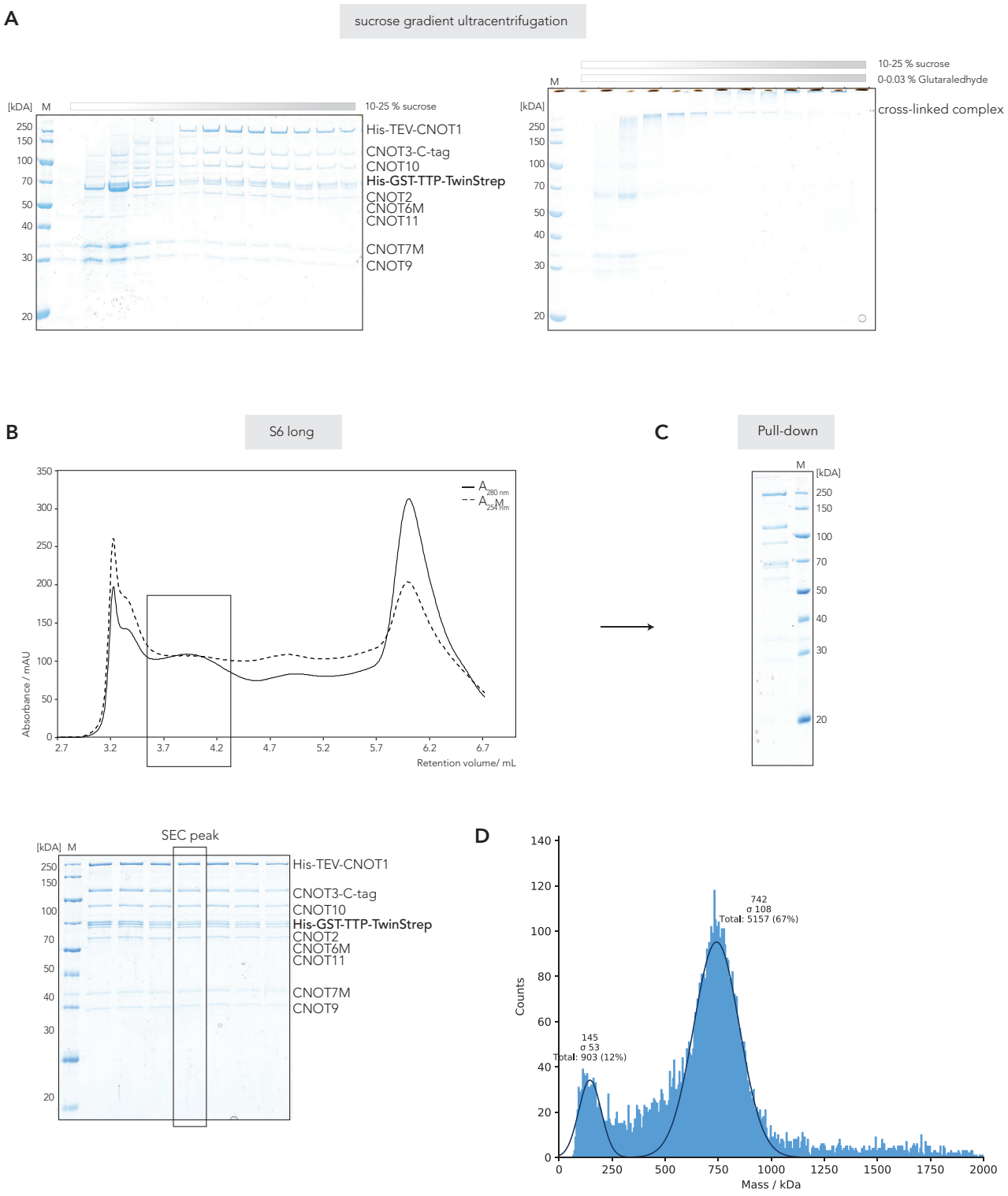

Figure 4.19. Complex formation and analysis of Ccr4-Not:TTP complex. A, SDS-Page analyses of sucrose gradient ultracentrifugation of the native complex (left) and the corresponding chemically cross-linked complex using GraFix (right). **B,** SEC elution profile of pre-mixed Ccr4-Not:TTP on home-made S6 column. The corresponding Coomassie-stained SDS-PAGE analysis below shows a stoichiometric complex without impurity bands. The elution fractions were pooled and subjected to a C-tag pull-down experiment, the elution is shown in **C**. **D,** MP measurements indicate, that the SEC peak fraction is composed of two main species; the main peak at 742 kDa may correspond to the Ccr4-Not:TTP complex and the peak at 145 kDa may correspond to a CNOT2:CNOT3 subcomplex.

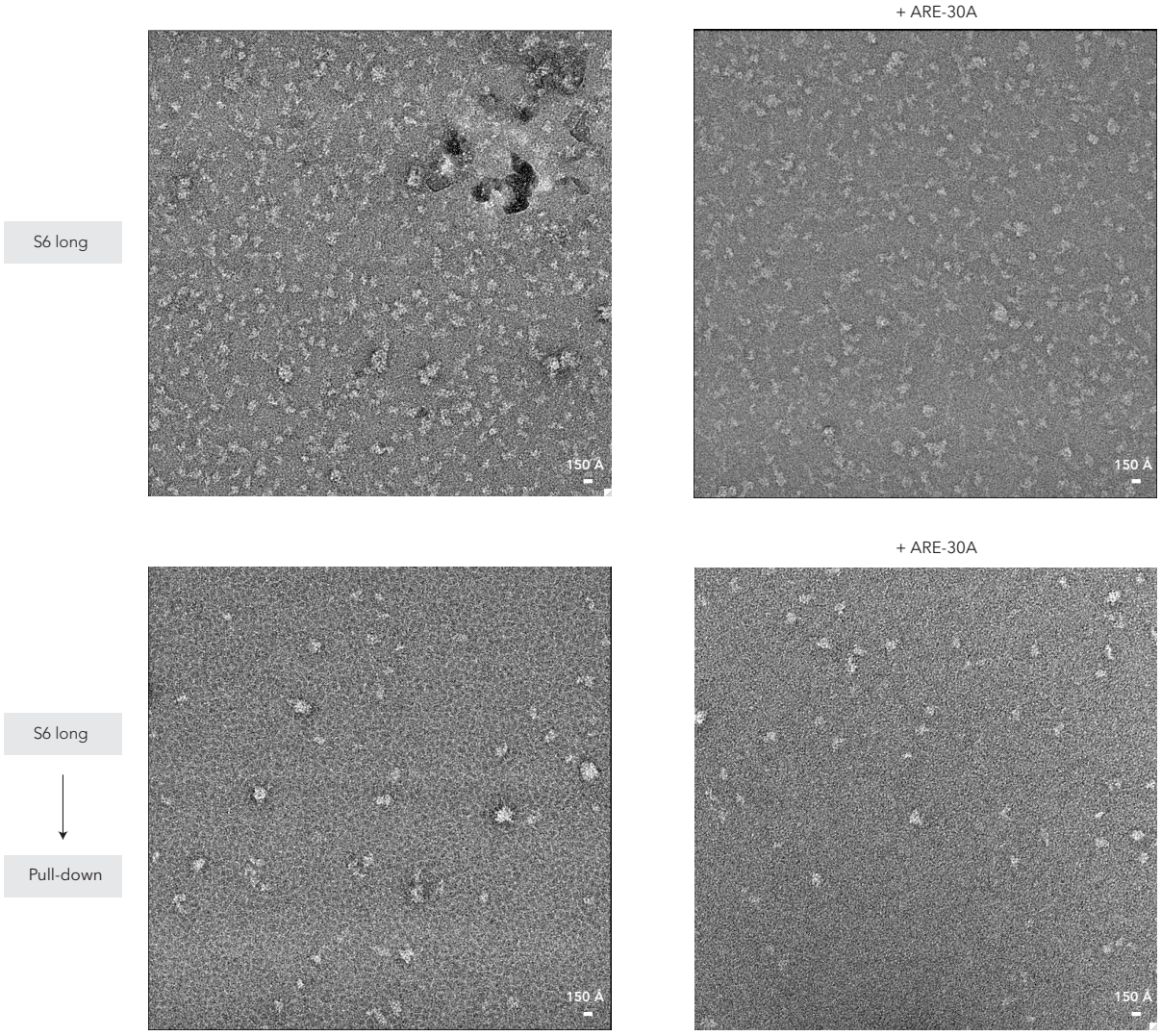

Figure 4.20. Comparison of different complex formation strategies. Negative staining micrographs acquired on a Titan Halo microscope operated at 300 keV, at a nominal magnification of 58,000x which corresponds to a pixel size of 1.85 Å/px. The sample was purified on the home-made S6 long column, followed by an optional C-tag pull-down experiment. The panels on the right show the sample after incubation with an ARE-30A RNA, before cross-linking and sample preparation for negative staining.

Since the optimization attempts mentioned above did not yield significant improvements in homogeneity, the strategy of two consecutive pull-downs of subunits from both ends of the Ccr4-Not complex was also used for reconstitution of the complex with TTP. To remove the SEPEA peptide from the buffer, Ccr4-Not and TTP-C-tag were purified in

parallel with a final C-tag pull-down, then mixed together and subjected to a second Strep pull-down, resulting in a stoichiometric complex, with no visible impurities (Fig. 4.21 B, left panel). To gain deeper insight into eventual changes in the architecture of Ccr4-Not in complex with a substrate, Ccr4-Not:TTP eluted from the StrepTactin pull-down was also incubated with the TTP-specific substrate RNA (5' CAC AUC UUA UUU AUU UAA AU [A]25 GGG AA 3'). The poly(A) tail of the RNA contained three guanosine nucleotides at the pre-penultimate position to stall the complex as it has been shown that multiple non-A nucleotides in a row, particularly guanosines, delayed the deadenylation *in vitro* of yeast and human Pan2 exonuclease as well as (*S. pombe*) Caf1 and Ccr4 and human CNOT6 and CNOT7 (Tang *et al.*, 2019; Chen *et al.*, 2021). Both samples were cross-linked with 1 mM BS^3 for 10 min on ice as Ccr4-Not alone and subjected to XL-MS analysis. The identified cross-links were mapped on available crystal structures and a predicted structure of TTP from AlphaFold 2 (Jumper *et al.*, 2021). Of 242 identified intra- and inter-cross-links in the Ccr4-Not:TTP sample, 82 could be mapped on available atomic models (Fig. 4.21, C). Figure 4.21 D shows the 72 mapped cross-links (of 259 identified intra- and inter-cross-links) of the Ccr4-Not:TTP:RNA sample. Cross-links between TTP and several domains of CNOT1 as well as CNOT3 were detected in both samples. In the presence of RNA, the cross-linking pattern changes at many sites; in particular, fewer cross-links are found between the N-terminal CNOT10:CNOT11 module (especially the flexibly attached C-terminal CNOT11 domain) and the C-terminally located NOT module (Fig. 4.21 C,D). The XL-MS experiments are one-time experiments that need to be repeated to confirm the cross-links. Therefore, no detailed analysis of the individual cross-links was performed. However, the presence of multiple mutually exclusive cross-links in both samples suggests the presence of multiple conformations rather than a single specific conformation. Since the XL-MS data are preliminary, the cross-linking pattern of the Ccr4-Not complex and Ccr4-Not:TTP in the presence or absence of RNA is compared in Fig. 5.3 in the discussion.

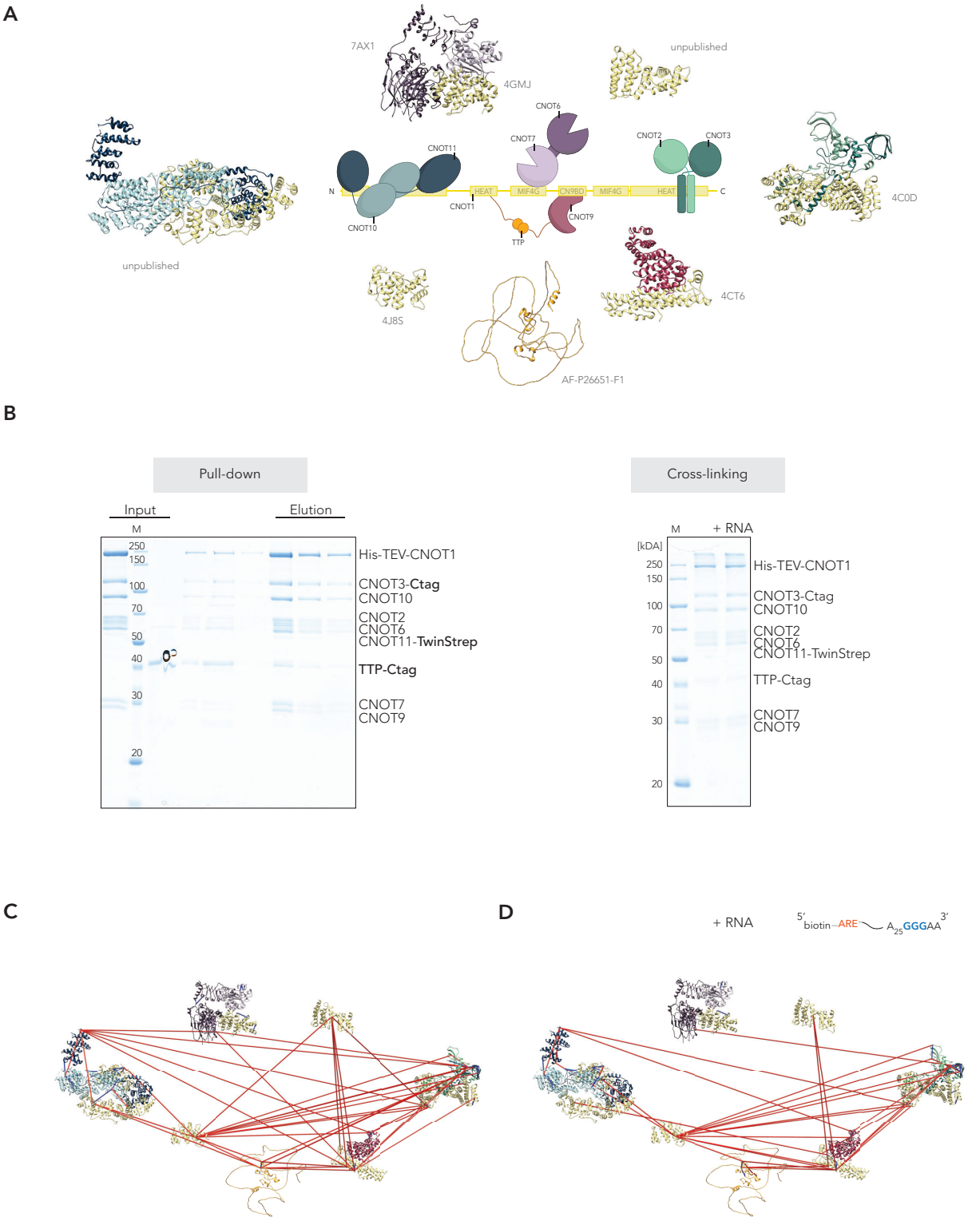

Figure 4.21. Cross-linking mass spectrometry of Ccr4-Not:TTP. A, Schematic representation of the architecture of the Ccr4-Not complex and TTP with the corresponding available atomic models of subunits or subcomplexes in cartoon representation. The structure of TTP is predicted by AlphaFold2 (Jumper *et al.*, 2021). **B,** Ccr4-Not and TTP were purified in parallel C-tag pulldowns and then subjected together to a second StrepTactin pulldown pulling on the TwinStrep tag on the C-terminus of CNOT11. **B, left,** Coomassie-stained SDS-PAGE analysis of input and elution fractions of StrepTactin pull-down experiment. **B, right,** The elution fraction was cross-linked with 1 mM of BS^3 for 10 min on ice in the presence or absence of ARE-25A-GGG-AA RNA shown on Coomassie-stained SDS-PAGE analysis. **C, D,** XL-MS data of Ccr4-Not:TTP (**C**) and Ccr4-Not:TTP:RNA (**D**) mapped on atomic models from (**A**) using Xlink Analyzer (Kosinski *et al.*, 2015) in UCSF Chimera, indicated by red lines. The modules are positioned distant from each other for better visualization.

Other interactor proteins were also tested, including the antiproliferative factor BTG2, the poly-A-binding protein PABPC1, and the RNA helicase DDX6. After interaction studies with pull-down and SEC experiments, samples were screened in EM, but the problem with structural heterogeneity remained (data not shown).

4.4 Biochemical characterization

It has been previously shown that recombinantly expressed and purified Ccr4-Not complexes successfully remove poly(A) tails of substrate RNAs and are recruited by RNA-binding proteins to specific target mRNAs in *in vitro* deadenylation assays (Raisch *et al.*, 2019; Stowell *et al.*, 2016; Webster *et al.*, 2019). To better understand Ccr4-Not's activity and also to ensure that the here described recombinant overexpressed and purified complex was intact and fully functional, the deadenylation activity was also tested in *in vitro* deadenylation assays.

The assay setup was similar to published protocols (Raisch *et al.*, 2019; Stowell *et al.*, 2016; Webster *et al.*, 2019). The RNA substrates used consisted of a 3' UTR-like 20-mer (5' CAC AUC CAA CUU CUC UAA AU 3') (Raisch *et al.*, 2019) with downstream poly(A) tails of 30 nt or 60 nt length with or without a G-triplet stalling sequence at position 25 or 55, and additionally labeled with fluorophores (Atto-550 or Atto-647N) at their 5'end for visualization, were synthesized by Ella Biotech GmbH. Both fluorophores were tested on the same substrates to exclude fluorophore bias in the reactions. The additional stalling sequence was tested in order to find a suitable substrate to stabilize the complex in one conformation for structural studies.

After initial screening for a suitable time range and ratio of enzyme complexes to RNA that allowed the reaction to be followed, 40 nM of active complex and 200 nM of total RNA per reaction and a time course with time points at 0, 10, 20 and 60 min was chosen. Reactions

were performed at 37 °C in a buffer adopted with minor modifications from Webster *et al.* (2019); Raisch *et al.* (2019). Either reaction buffer or complexes with catalytically inactive mutants of both nucleases (CNOT6M: CNOT6(E240A) and CNOT7M: CNOT7(D40A, E42A)) served as negative controls.

4.4.1 Ccr4-Not prefers substrate with longer poly(A) tail

The full Ccr4-Not complex was recombinantly co-expressed in insect cells and purified as described above in section 4.2.2. It was previously reported, that the length, but not the sequence, of the 3'UTR affects the deadenylation activity of the human Ccr4-Not complex (Raisch *et al.*, 2019). To test how the length of the poly(A) tail affects the deadenylation activity, the complex was mixed with substrate RNAs with the same 3'UTR sequence but with poly(A) tails of 30 or 60 nt length both individually and in competition, and deadenylation was monitored over time. Deadenylation of R-60A RNA proceeds very similarly in the presence and absence of the RNA with the shorter poly(A) tail, whereas deadenylation of R-30A RNA proceeds more slowly in the presence of the long RNA (Fig. 4.22 B), suggesting that Ccr4-Not prefers the RNA with the longer poly(A) tail.

4.4.2 G-triplet in poly(A) tail affects deadenylation activity

The tetrameric Ccr4-Not$_{CORE}$, comprising only the central part of CNOT1, both nucleases CNOT6 and CNOT7, and CNOT9 was recombinantly expressed in insect cells using the biGBac system and purified as described in 4.1.1. The WT Ccr4-Not$_{CORE}$ was functionally active and removed the poly(A) tails of the R-60A substrate RNA. The reaction proceeds even after the last adenosine of the poly(A) tail (Fig. 4.23 B, first box). No deadenylation activity was detected for the Ccr4-Not$_{CORE}$DM complex with active site mutants of both nucleases (CNOT6 E240A, CNOT7 D40A, E42A), indicating that no contaminating ex-

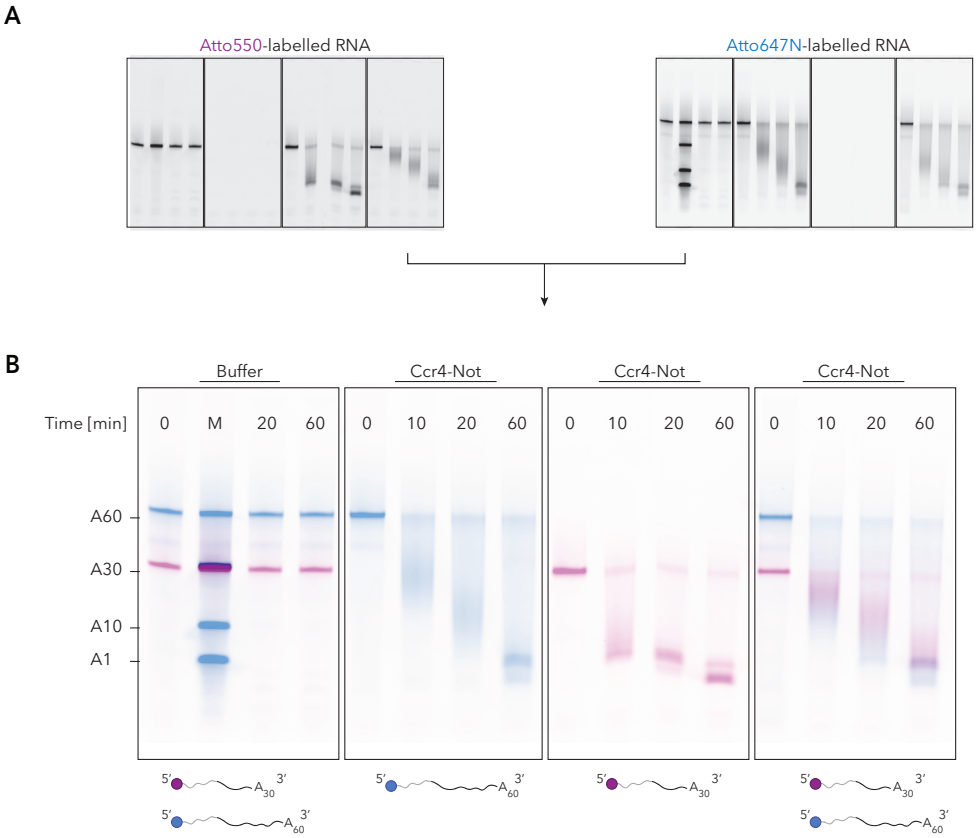

Figure 4.22. Ccr4-Not prefers RNA with longer poly(A) tail. A, Deadenylation time course experiment, with 200 nM of 20-mer A[30] and 20-mer A[60] total RNA and 40 nM of the Ccr4-Not complex, analyzed by Urea-PAGE. Gels were scanned twice to detect each fluorophore before signals were overlaid using Fiji. **B,** Overlay of (**A**). In competition, the rate of deadenylation of R-60A RNA does not change, whereas the rate of deadenylation of R-30A slows down.

onuclease was co-purified and responsible for the degradation past the last A of the poly(A) tail (Fig. 4.23 B, box 2).

The full Ccr4-Not complex deadenylates the R-60A substrate faster than the core complex (compared in Fig. 4.25 A) and unlike the core complex, deadenylation of most substrates stops at the last A of the poly(A) tail (see Fig. 4.24 B, second box) suggesting higher selectivity of the full-complex for poly(A) close to the RNA body. In case of a G-triplet at position -2 from the 3'end of the poly(A) tail, the deadenylation activity of the core complex was drastically reduced. Regardless of total poly(A) tail length, after 20-60 min, a low amount of deadenylated substrates became visible, but most of the substrate was

still complete. When both R-55A-GGG AA and R-60 competed, the R-60A RNA was deadenylated slightly slower compared to before (Fig. 4.23 B, box 4 vs. box 1).

In contrast to the core complex, the full complex (Fig. 4.24 B, third box) removed the poly(A) tails of most of the R-55A-GGG-AA substrate, however significantly slower than of R-60A RNA. When R-60A and R-55A-GGG-AA competed (Fig. 4.24 B, box 4), deadenylation of both substrates was slower than for either substrate, regardless of the total length of the poly(A) tail.

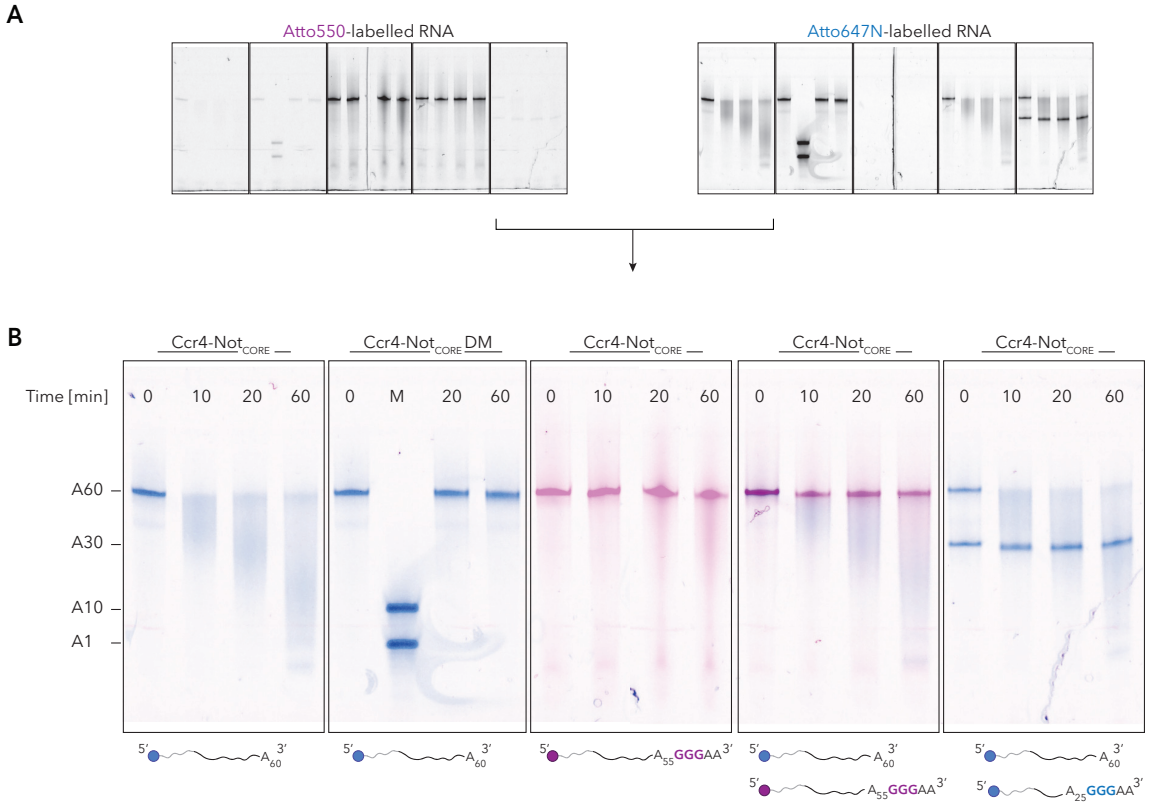

Figure 4.23. G-triplet significantly decreases deadenylation activity of Ccr4-Not$_{CORE}$. A, Deadenylation time course experiment of the deadenylation of 5' fluorescently labelled RNA comparing 60A poly(A) tails with 55A-GGG-AA tails by Ccr4-Not$_{CORE}$. The reactions were analyzed by Urea-PAGE. Gels were scanned twice to detect each fluorophore before signals were overlaid in Fiji. **B,** Overlay of **A.**

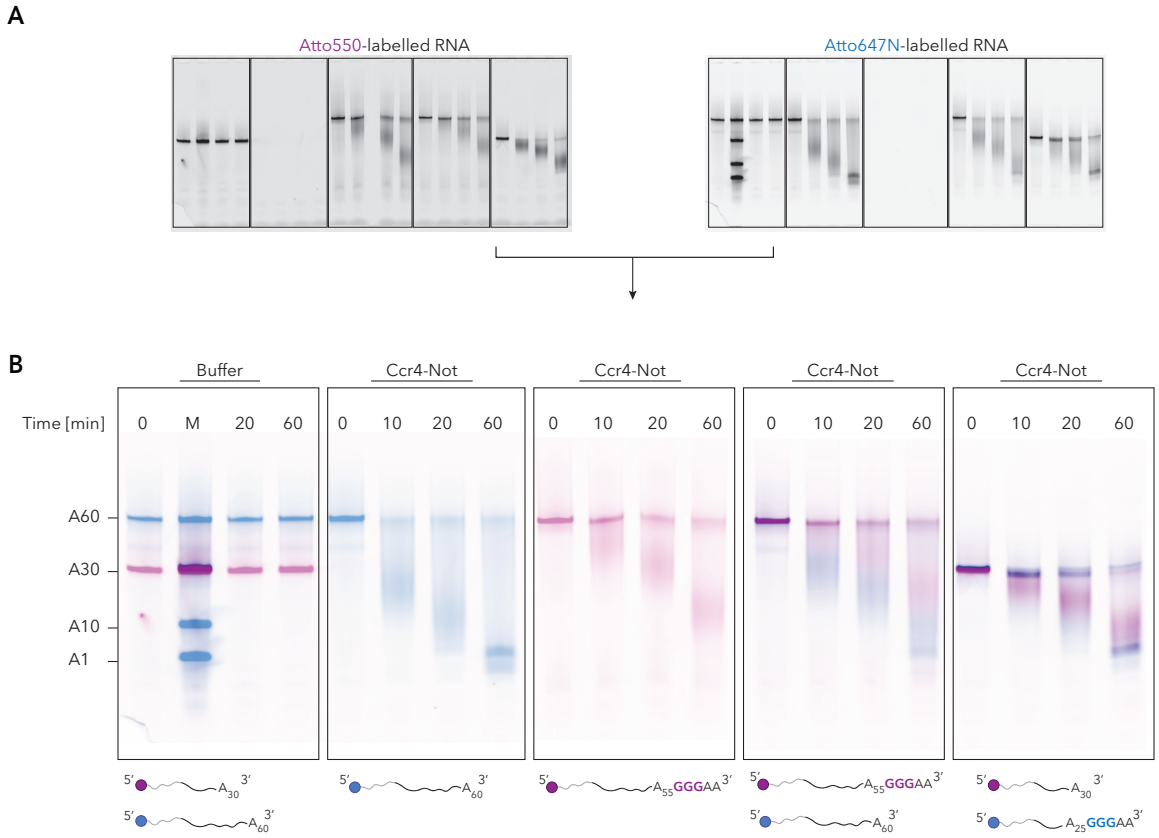

Figure 4.24. G-triplet slows down deadenylation activity of Ccr4-Not. A, Deadenylation of 5' fluorescently labelled RNA comparing poly(A) was analyzed by Urea-PAGE. Gels were scanned twice to detect each fluorophore before signals were overlaid. **B,** Overlay of (A) and colored using Fiji. The deadenylation rate of Ccr4-Not is slower in presence of a G-triplet at position -2 of the 3' poly(A) tail.

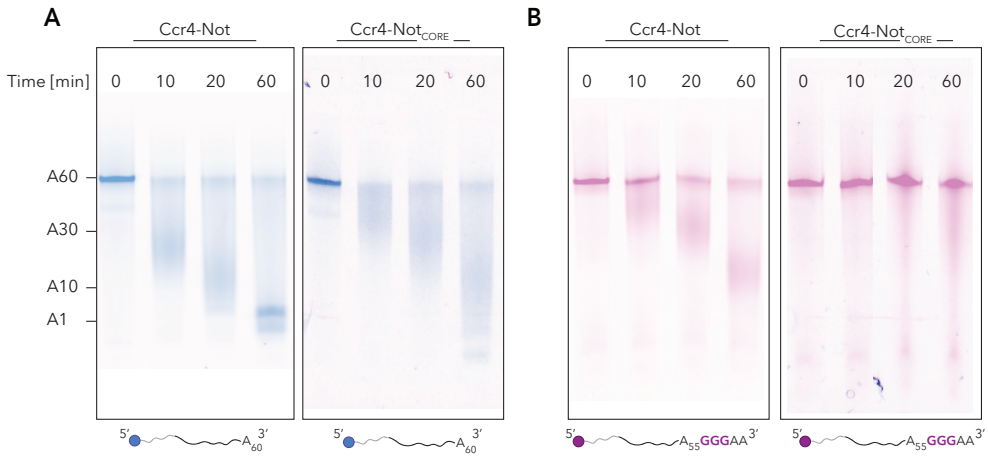

Figure 4.25. Comparison of deadenylation activities of Ccr4-Not and Ccr4-Not$_{CORE}$. The deadenylation assays from 4.23 and 4.24 were positioned next to each other for better visualization. **A,** The full Ccr4-Not complex shows higher deadenylase activity and specificity for poly(A) than Ccr4-Not$_{CORE}$. **B,** The full Ccr4-Not complex is slowed down but not stalled by the stalling R-55A-GGG-AA substrate.

4.4.3 RNA-binding protein TTP enhances deadenylation of ARE-RNA

It was reported that the deadenylation activity of fission yeast Ccr4-Not is enhanced in the presence of specific RNA-binding proteins such as Mmi1, Puf3 and Zfs1 (Stowell *et al.*, 2016; Webster *et al.*, 2019) and slows down the human complex in presence of sequence motifs like Bam-CBM interacting with CNOT9, thereby blocking its RNA binding surface (Raisch *et al.*, 2019). The RNA-binding protein TTP recognizes specifically ARE-motifs within the 3'UTR of its target transcripts, leading to their decay. Therefore, RNA substrates containing the ARE-sequence UUAUUUAUU within the 20-mer 3'UTR (5' CAC AUC UUA UUU AUU UAA AU 3') and downstream poly(A) tails of 30 A length or 25A-GGG-AA were used. First, the influence of the ARE-motif within the 3'UTR was tested. The deadenylation time-course experiment shows accelerated deadenylation of R-ARE-30A compared to the R-30A substrate (Fig. 4.26 B, box 1 and 2). To test the effect of TTP on deadenylation activity, TTP was recombinantly expressed in *E. coli* and purified as described above in 4.3. It was added to 200 nM of buffered RNA at a final concentration of 250 nM and incubated on ice for 15 min before adding the active Ccr4-Not complex at a final concentration of 40 nM to start the deadenylation reaction. Addition of TTP to the reaction with R-30A did not significantly alter the deadenylation pattern. However, the addition of TTP significantly increased the rate of deadenylation of the R-ARE-30A substrate, indicating a specific acceleration. When R-ARE-25A-GGG-AA and R-ARE-30A compete, the R-ARE-25A-GGG-AA substrate is partially deadenylated at a rate similar to that without the stalling sequence. However, the remaining substrate is not deadenylated at all. The R-ARE-30A substrate is deadenylated slightly slower, comparable to the R-30A RNA without additional TTP (Fig. 4.26 B, last box).

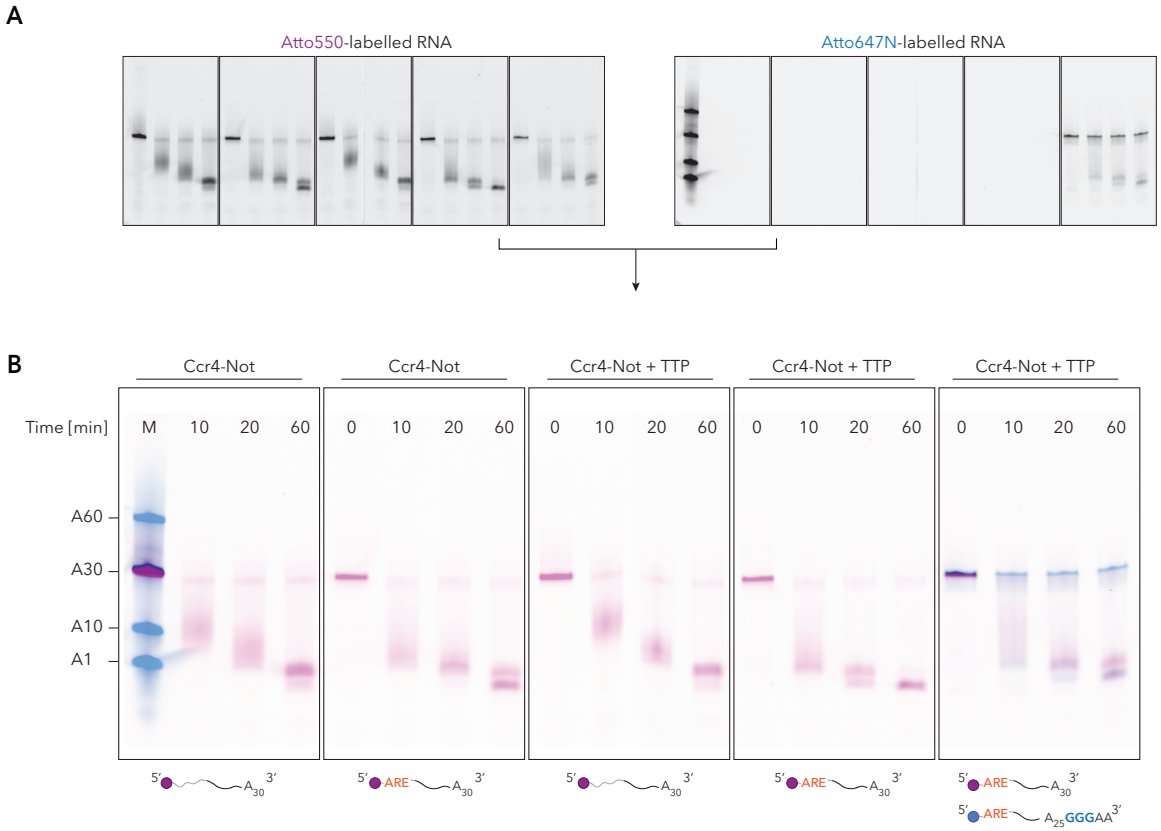

Figure 4.26. TTP accelerates deadenylation of ARE-RNA. A, Deadenylation of 5' fluorescently labelled RNA containing an ARE-motif in presence or absence of TTP was analyzed by Urea-PAGE. Gels were scanned twice to detect each fluorophore before signals were overlaid and colored in Fiji. **B,** Overlay of (A). The R-ARE-30A is deadenylated faster than the R-30A. In presence of TTP, only the deadenylation reaction of R-ARE-30A is significantly accelerated.

Chapter 5

Discussion and Outlook

5.1 Discussion

In this thesis, a strategy for recombinant co-expression and purification of the full-length human Ccr4-Not complex in insect cells was presented. The purified complex was structurally characterized by negative stain- and cryo-electron microscopy and by cross-linking mass spectrometry. Ccr4-Not's deadenylation activity was studied in *in vitro* deadenylation assays in the presence of one of its interactors, the ARE-binding protein TTP. Although, a 3D reconstruction of the human Ccr4-Not complex was only resolved to medium resolution, the biochemical and biophysical studies of the sample and the experimental conditions presented will be useful for future experiments.

5.1.1 EM studies on Ccr4-Not

Structural studies of the global architecture of the Ccr4-Not complex have so far been limited to complexes from yeast species. Two available structures representing the budding yeast and fission yeast complexes were determined by negative stain- and cryo-electron microscopy, albeit at medium to low resolution (Nasertorabi *et al.*, 2011; Ukleja *et al.*, 2016). In both cases, complexes were subjected to GraFix, a method for cross-linking protein complexes during density gradient centrifugation (Kastner *et al.*, 2008), prior to

EM studies to stabilize the particles and increase sample homogeneity. Resolution was still limited due to apparent flexibility and persistent heterogeneity (Nasertorabi *et al.*, 2011; Ukleja *et al.*, 2016).

The human Ccr4-Not complex, which was structurally investigated in this study, showed similar properties in negative stain- and cryo-EM. Even the smaller, presumably more stable subcomplexes of Ccr4-Not, Ccr4-Not$_{CORE}$, Ccr4-Not$_{\Delta C}$, showed strong heterogeneity in particle sizes and shapes and partial aggregation or disintegration of particles on EM micrographs (see Fig. 4.3,4.7 and chapters 4.1.1,4.1.3). Different methods for obtaining more stable, homogeneous complexes, such as sucrose density ultracentrifugation and gel filtration to reconstitute the complexes, were subsequently compared by negative stain- and cryo-EM. Only minor differences were observed, indicating that the apparent disintegration and aggregation were likely caused by interactions with the air-water interface (AWI) during EM sample preparation.

The sample preparation of biological samples for cryo-electron microscopy must meet certain requirements. The sample must be protected from the electron beam, remain hydrolyzed in the high vacuum of the microscope, while the protective layer must be thin enough for the electron beam to penetrate (Taylor & Glaeser, 2008). The commonly used method involves applying of a few microliters of sample in a buffer solution onto a metal grid, covered with a holey carbon support layer, that has been hydrophilized before. The extra liquid is removed with filter paper, and the remaining thin layer of ideally well-dispersed particles is plunge frozen in a cryogen like liquid ethane to form a vitreous layer of ice (Adrian *et al.*, 1984; Dubochet & McDowall, 1981; Taylor & Glaeser, 1974). In the few seconds between blotting and vitrification, the particles move due to Brownian motion, diffusing about 10-1000 times to the AWI according to theoretical estimations (Naydenova & Russo, 2017). Interactions with the AWI can cause conformational change, induce a preferred orientation, or lead to partial or complete unfolding through hydrophobic inter-

actions (D'Imprima *et al.*, 2019). The extent of adsorption of particles to the AWI thereby depends on numerous factors, which include protein concentration, structural stability, surface hydrophobicity, as well as buffer conditions, presence of detergents etc (Noble *et al.*, 2018). However, it appears to be a widespread behavior, as a study of various protein samples using cryo-electron tomography (cryoET) revealed that most of the particles prepared by conventional methods indeed adsorbed at the air-water interface, although the samples varied widely in terms of denaturation, preferred orientation, and ice thickness (Noble *et al.*, 2018).

Interactions with the AWI can be altered by the addition of surfactants, the use of grids that provide an additional interface e.g. affinity grids, or by shortening the time between sample application and freezing (reviewed by Dmitry Lyumkis in Glaeser *et al.*, 2021). Unfortunately, there is no condition that applies equally to all samples; therefore sample-specific optimization of the freezing conditions is necessary.

In this study, detergents such as nonyl phenoxypolyethoxylethanol (NP-40), β -OG, Lauryl Maltose Neopentyl Glycol (LMNG) below critical micelle concentration (CMC) and also the surfactant Amphipol A8-35 (Amphipol) were successfully tested to overcome decomposition of the complexes, shown exemplary for β -OG in Fig. 5.1. Since the complexes appeared to be sensitive to the AWI, exposure to additional hydrophobic surfaces, such as concentrator membranes, was avoided for the full-length complex after reconstitution. Therefore, the protein concentration was limited (max. $\sim$ 1 µM for the full Ccr4-Not complex). At this concentration, particles were visible in free ice using LMNG, amphipol, and β-OG, but not NP-40 (data not shown). As the distribution of ice thickness over the whole grid appeared most homogeneous and most reproducible with 0.04 % (v/v) of β-OG, this condition was used for all further grid-preparations.

Aggregation and partial complex disintegration were also counteracted by cross-linking with BS^3 or glutaraldehyde. In addition to cross-linking, BS^3 and glutaraldehyde also re-

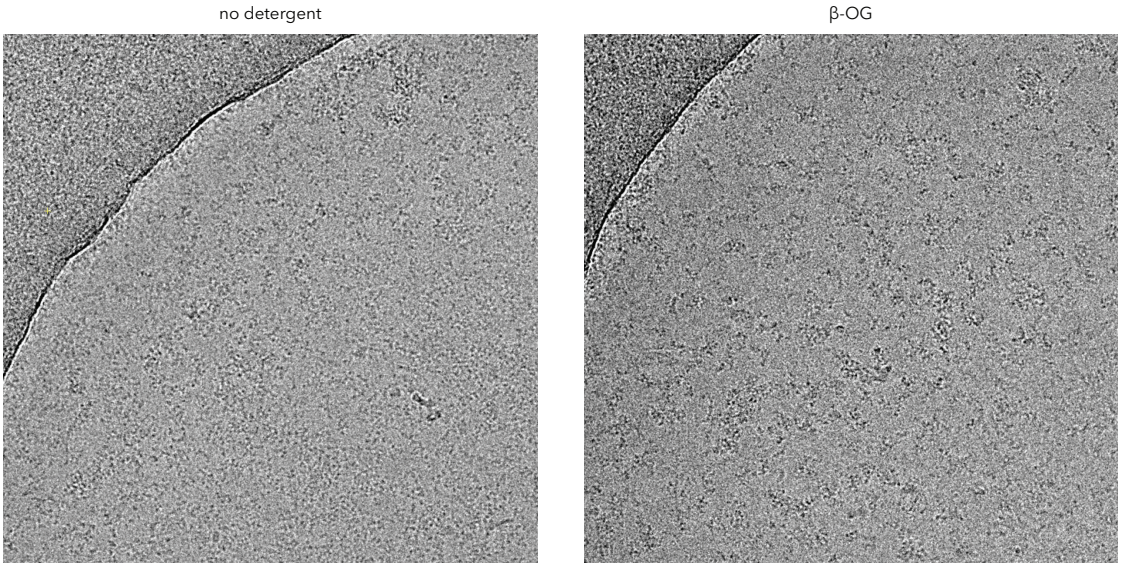

Figure 5.1. The addition of detergent reduces disintegration and aggregation. Representative cryo-EM micrographs of vitrified full Ccr4-Not complex. The disintegration and aggregation of particles is reduced by the addition of 0.04 % (v/v) of β -OG.

act with exposed residues thereby altering surface properties. However, the heterogeneity in particle sizes for Ccr4-Not$_{\mathrm{CORE}}$ and Ccr4-Not$_{\Delta\mathrm{C}}$ remained, and processing of the data sets did not result in 3D reconstructions that contained all subunits. This could be due to disintegration because of too mildly cross-linking or flexible attachment of the subunits in the context of the smaller complexes.

Samples of the full-length Ccr4-Not complex, reconstituted from purified subcomplexes showed similar behavior on EM micrographs. However, disintegration of the complex was significantly reduced when the complex was co-expressed in insect cells. The improved sample of the full Ccr4-Not complex showed more particles of similar larger diameters around 200-250 Å even without cross-linking on cryo-EM micrographs with 0.04 % (v/v) of β-OG and on grids with additional support layer such as carbon or a home-made layer of graphene oxide after a protocol of Palovcak *et al.*, 2018. However, processing of screening data sets revealed additional compositional heterogeneity, and less well resolved densities

indicated a high degree of sample flexibility, which was predicted by structure prediction tools and also confirmed by XL-MS data (Fig. 4.15).

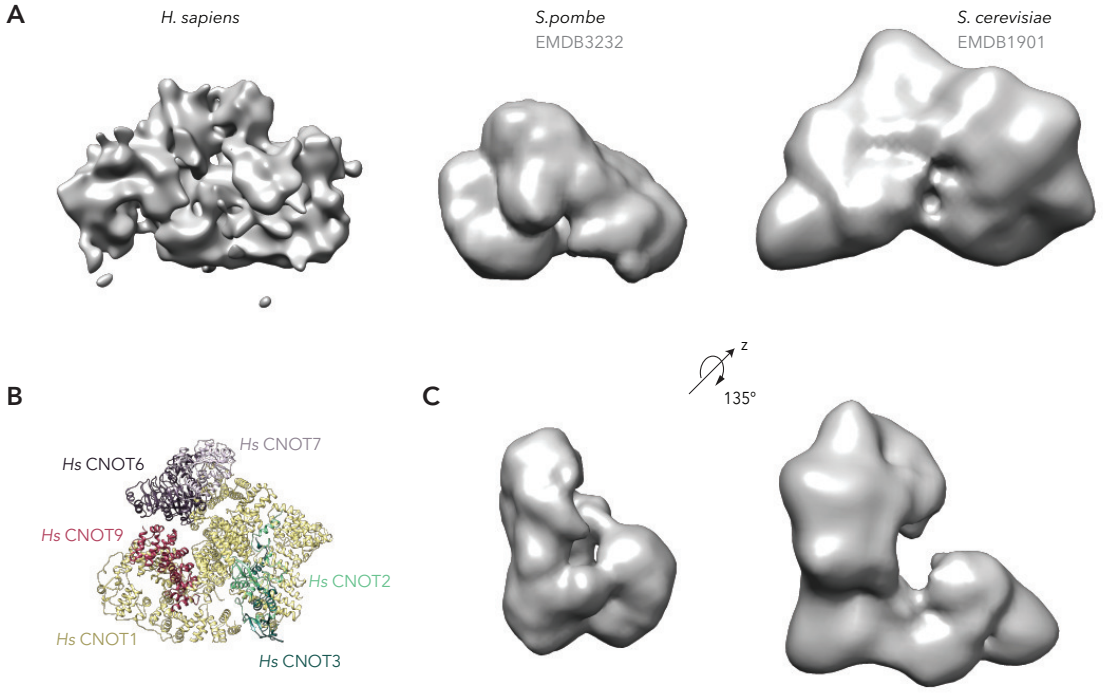

Figure 5.2. Comparison of yeast and human of Ccr4-Not structures. A, 3D reconstructions of Ccr4-Not complexes from *H. sapiens* (this study), *S. pombe* (EMDB3232) and *S. cerevisiae* (EMDB1901) with increased threshold compared to the maps with the approximate threshold of the published papers (**C**) turned 135°around the z-axis (Ukleja *et al.*, 2016; Nasertorabi *et al.*, 2011). **B,** Composite model from Fig. 4.15, D without CNOT10 and CNOT11.

The resolution of a 3D reconstruction obtained from a large (17k micrographs) data set to counteract the apparent flexibility was hampered by the poor SNR of this data set. The 'final' 3D reconstruction of the Ccr4-Not complex presented here, appears to be large enough to accommodate all subunits as was tested by positioning of a possible model based on XL-MS data (see Fig. 4.16).

The overall shape is relatively similar to the previously determined low to medium-resolution L-shaped structures of budding and fission yeasts (Ukleja *et al.*, 2016; Nasertorabi *et al.*,

2011) when the threshold of the 3D reconstructions is slightly increased (see Fig. 5.2 A). The dimensions of the complexes from *S. cerevisiae* and *H. sapiens* are similar with 180-190 Å (yeast) and 120-190 Å (human). However, the structure of the fission yeast complex, reported to be 140-150 Å, appeared to be smaller (110-150 Å). A simulated map of the model of the human Ccr4-Not complex described here, without the species-specific CNOT10 and CNOT11 (Fig. 5.2, B), could be fitted using rigid-body fitting in UCSF Chimera with a correlation of 0.702 into the *S. pombe* structure and 0.819 into the *S. cerevisiae* density (data not shown). However, no meaningful comparisons can be made without higher resolution and accurate subunit placement.

5.1.2 Ccr4-Not and ARE-binding protein TTP

To reduce the apparent flexibility, attempts were made to stabilize the complex in a specific conformation with an interacting protein that binds several subunits of the complex simultaneously. Therefore, the complex was reconstituted with RNA-binding protein TTP, which interacts specifically with ARE-containing RNAs and was previously reported to interact with the CNOT1 and CNOT9 subunits of the Ccr4-Not complex (Fabian *et al.*, 2013; Bulbrook *et al.*, 2018). Various strategies to reconstitute the complex in the presence or absence of the specific ARE-RNA were tested and screened for improved homogeneity of particles in negative stain and cryo-EM. However, in the conditions used, no structural stabilization of the complex was detectable. The particles appeared even more heterogeneous in size as additional larger complex assemblies and aggregation were visible on the micrographs. This could result from the presence of several binding sites of TTP, that may connect more than one Ccr4-Not complex. An alternative explanation is aggregation as TTP possesses many low-complexity regions.

The suggested compositional heterogeneity and flexibility was also supported by XL-MS data of Ccr4-Not:TTP in the presence/absence of an ARE-stalling RNA (Fig. 4.21). The

comparison of XL-MS data of Ccr4-Not and Ccr4-Not:TTP/RNA should be taken with caution, as it was a one-time experiment. Nevertheless, the global cross-linking pattern changes in the presence of TTP and TTP:RNA. In this more visual representation (Fig. 5.3), cross-links are mapped only when the corresponding residues are present in the crystal structures and the predicted structure of TTP in AlphaFold2 (Jumper *et al.*, 2021). The total number of identified crosslinks in the samples are described in Table 5.1. The lower number of mapped cross-links in the samples with TTP is due to changes in the cross-linking pattern, as many of the identified cross-links are located between the N-terminus of CNOT3 or the N-terminus of CNOT10 (which are absent in the atomic models) and other subunits of the complex (Fig 5.4).

Table 5.1. Total numbers of identified cross-links.

Complex	Total number of cross-links	Number of mapped cross-links
Ccr4-Not	227	103
Ccr4-Not:TTP	242	82
Ccr4-Not:TTP:RNA	259	70

Comparison of Ccr4-Not:TTP in the absence or presence of RNA suggests structural rearrangements due to the binding of RNA, as the cross-linking pattern changes. In particular, the CNOT10:CNOT11 module has less cross-links to the other subunits, but also a cross-link of TTP to the NOT module disappears. In the presence of RNA, new cross-links appear within the nuclease module (see Fig. 5.3). The XL-MS measurements have to be repeated to confirm the identified cross-links. To identify the protein-RNA interactions, the data could be complemented by RNA-protein cross-linking mass spectrometry.

One could imagine that depending on the type of RNA substrate, different modules of the complex contribute to RNA binding and therefore the conformation of the complex changes. This is supported by interaction studies with isolated components or subcom-

plexes of Ccr4-Not (Raisch *et al.*, 2019; Poetz *et al.*, 2021). A recent study showed binding of an RNA substrate under electrophoretic mobility shift assay (EMSA) conditions of the CNOT10:CNOT11 module and CNOT9, but not the NOT module (unlike the *S. cerevisiae* NOT module (Bhaskar *et al.*, 2013) which binds to RNA) (Raisch *et al.*, 2019). Increase in deadenylation activity was also observed in the presence of the CNOT9 and NOT modules compared with the nuclease module alone. The presence of the CNOT10:CNOT11 module, however, increased deadenylation activity only when the RNA-binding surface of CNOT9 was blocked, in this case by the additional recruitment factor *Dm* bag-of-marbles (BAM). It is therefore likely, that CNOT9 stabilizes RNA binding in the case of bulk mRNA decay but compensates for the CNOT10:CNOT11 module in the case of blockage of the RNA-binding surface of CNOT9 by a specific RBP (Raisch *et al.*, 2019; Poetz *et al.*, 2021).

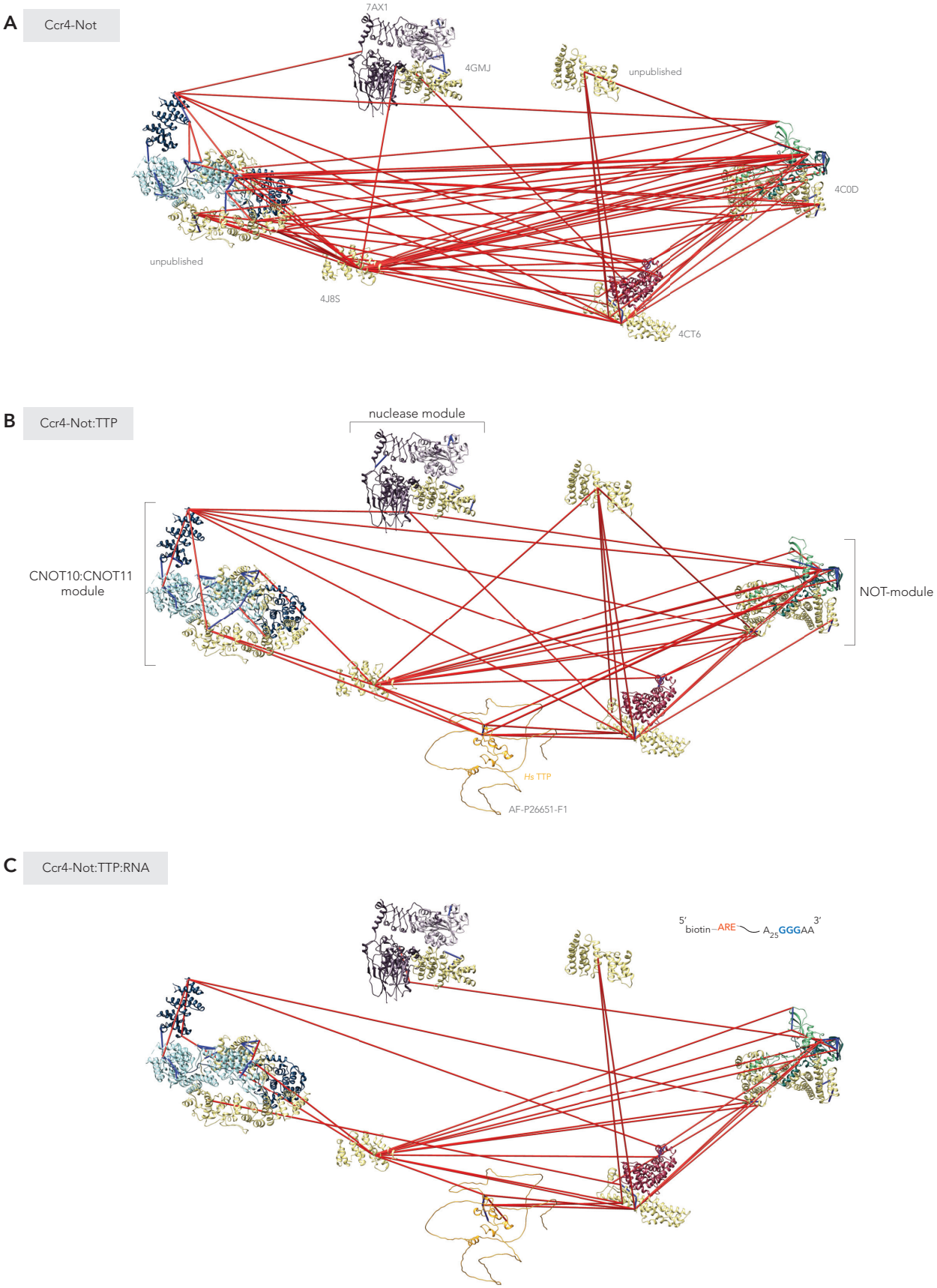

Figure 5.3. Comparison of XL-MS data of Ccr4-Not complexes. Identified XL-MS cross-links (red lines) of the Ccr4-Not complex, (**A**) in complex with TTP (**B**) and TTP and RNA (**C**) after cross-linking with 1 mM BS^3 mapped onto crystal structures of subcomplexes and subunits in UCSF Chimera using XlinkAnalyzer. The modules are positioned distant from each other for better visualization.

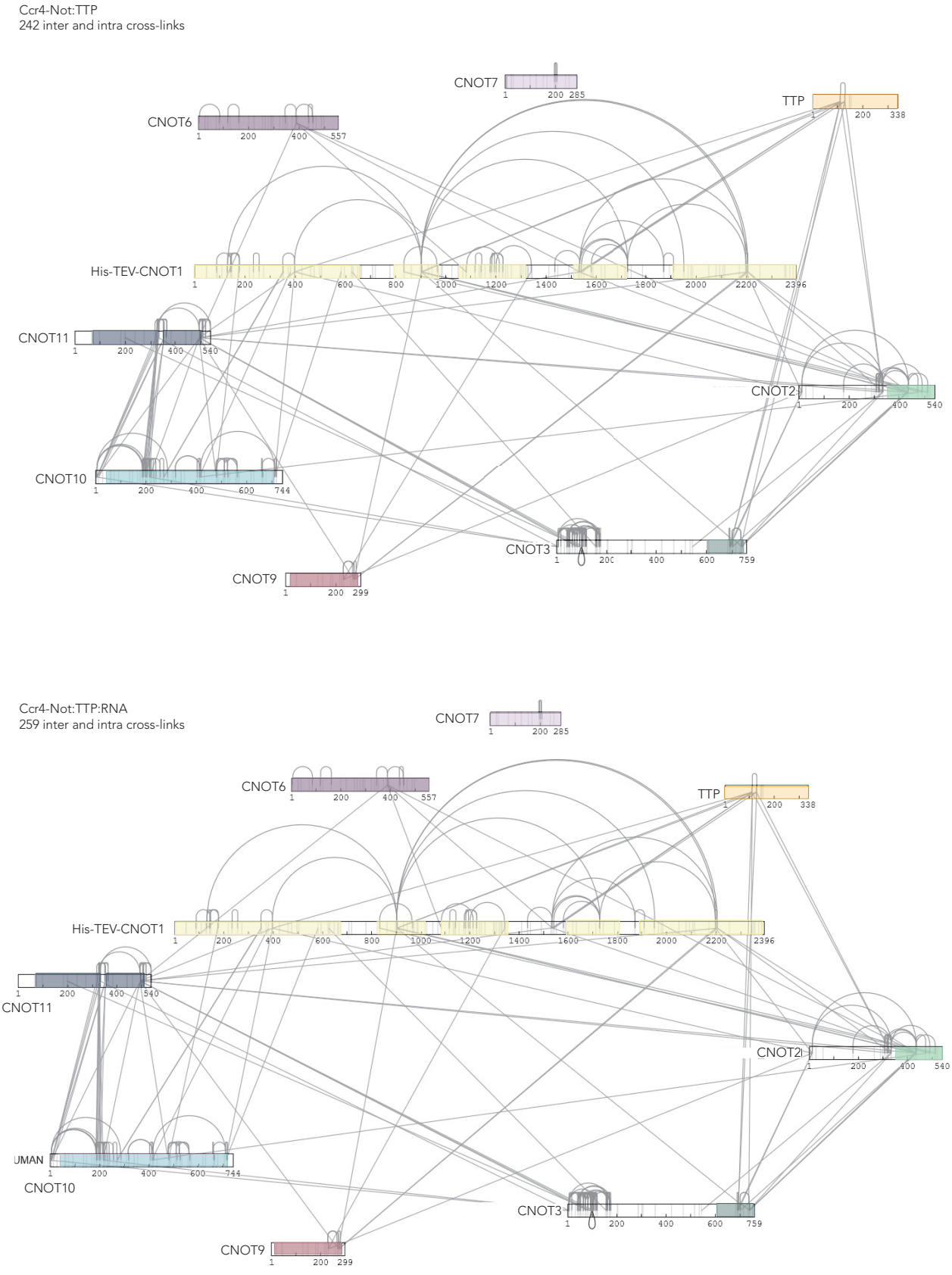

Figure 5.4. XL-MS data of Ccr4-Not:TTP/RNA Identified XL-MS inter and intra cross-links of the BS^3 cross-linked Ccr4-Not:TTP complex and Ccr4-Not:TTP:RNA complex. Regions, present in the crystal structures (4.15) of subcomplexes are highlighted in the respective color of the subunit as in 4.15.

5.1.3 Biochemical characterization

Previous studies with recombinantly expressed and purified Ccr4-Not complexes from *S.pombe* and *H. sapiens* showed greater deadenylation activity and greater selectivity for poly(A) nucleotides compared to the isolated nucleases in *in vitro* deadenylation assays (Stowell *et al.*, 2016; Webster *et al.*, 2018; Raisch *et al.*, 2019; Webster *et al.*, 2019). In this study, the full Ccr4-Not complex, which was co-expressed in insect cells, was also more active overall compared to the tetrameric Ccr4-Not$_{CORE}$ (see Fig. 4.25). Additionally, the full complex appeared to be more selective for the end of the poly(A) tail at the junction with the 3'UTR. However, when a G triplet was positioned at the third-to-last position of the poly(A) tail, the deadenylation activity of the full complex was not as strongly inhibited as that of the core complex (see Fig. 4.25). To further investigate the 'stalling' of the core complex, the reaction should be analyzed on gels with a higher polyacrylamide concentration at the level of single nucleotides, and the reaction should be performed at a 1:1 ratio (RNA:enzyme complex) with shorter time points and longer total run time. CNOT7's deadenylation activity in context of the isolated human nuclease module is pH-dependent (Chen *et al.*, 2021). It tends to be lower at the pH of 6.8, used here, compared to pH 7.4. Since CNOT6 and CNOT7 are affected differently by non(A) nucleotides (Chen *et al.*, 2021), the assays should also be performed at higher pH values. However, the effect of pH on the deadenylase activity of CNOT7 may be less in the context of the full complex. A comparison of the activities with the complex reconstituted from individual subcomplexes might be an interesting control experiment.

While previous work, that characterized a recombinant fission yeast Ccr4-Not complex, showed that the sequence/structure but not the length of the upstream 3' UTR, affected the deadenylation activity (Stowell *et al.*, 2016; Webster *et al.*, 2019), the human complex was shown to be more affected by the length of the 3' UTR but hardly by the sequence or

structure, as a small stem-loop delayed the rate of deadenylation initially but proceeded until the RNA body was reached (Raisch *et al.*, 2019). In this study, a substrate with the canonical ARE motif (5' CAC AUC **UUA UUU AUU** UAA AU 3') was deadenylated faster than the substrate with a divergent 3'UTR sequence (see Fig. 4.26 B) (similar to the fission yeast complex (Webster *et al.*, 2019)). At least in this particular example, there appears to be an intrinsic sequence specificity or preference of the Ccr4-Not complex. In addition, a competition assay was performed to determine whether the complex preferentially deadenylates substrates with shorter or longer poly(A) tails. Under the conditions tested, RNA with a 60A tail was preferred by the full complex over a substrate with a 30A tail (Fig 4.22). The preference could be due to the fact that the modules with RNA binding capacities (e.g. CNOT10:CNOT11, CNOT9) contribute not only to the stabilization of a longer 3'UTR but also to the stabilization of a longer poly (A) tail, but to confirm this, the experiments would have to be repeated with complexes of different module compositions.

Targeted deadenylation

Additional factors were shown to modulate the deadenylation activity of Ccr4-Not. In fission yeast Mmi1, Puf3 and Zfs1 accelerated the reaction in a sequence-specific manner (Stowell *et al.*, 2016; Webster *et al.*, 2019). On the other hand, the deadenylation activity of the human complex could be slowed down by the addition of *Dm* BAM or RNF219, which associate with the concave surface of CNOT9, and thereby interfering RNA-binding (Raisch *et al.*, 2019; Poetz *et al.*, 2021). In this study, the presence of the interactor TTP also resulted in faster deadenylation when the 3'UTR-like sequence of the substrate contained an ARE motif (Fig. 4.26). In a competition assay of ARE-RNA with or without the G-triplet in the presence of TTP, it appeared that some of the triple-G-stalling substrate was deadenylated at the same rate as the non-stalling substrate, but much of the stalling substrate remained complete. To understand if this is just due to the slow reaction

and 5:1 (RNA:enzyme complex) ratio or if some of the complexes are actually stalled, this assay should also be repeated at a 1:1 ratio of RNA to enzymes and over a much longer period of time to see if all substrates are eventually processed.

To investigate the physiological relevance of the poly(A) tail length preference these experiments need to be repeated in the presence of PABPC1, since it was previously shown, that both nucleases from human and fission yeast exhibited different deadenylation activities in the presence of the poly(A) binding protein Pab1/PABPC1 (Yi *et al.*, 2018; Webster *et al.*, 2018).

5.2 Outlook

The Ccr4-Not complex is a multifaceted key player in the regulation of gene expression. The methods provided here for expression and purification of the complex, as well as the conditions of the biochemical assays, can serve as a basis for further investigation of the complex network that regulates deadenylation activity of Ccr4-Not. In particular, regulation in the presence of PABPC1 is likely to be physiologically relevant and should be included in biochemical assays and structural studies. Also, RNA binding properties of the individual modules to different RNA substrates as well as the influence of RNA sequence and structure and RNA modifications on deadenylation activity of the complex are of interest.

Due to the dynamic nature and the amount of interacting proteins of the Ccr4-Not complex, the complex likely exists in different compositions and conformations in the cell. In order to decipher at least one of these conformations unambiguously interpretable, a set of binding partners or conditions must be found to stabilize it for cryo-EM. Cross-linking mass-spectrometry with various interactors could contribute to faster find a suitable binding partner(s) for cryo-EM studies. Once the conditions for one interactor/substrate are found, they may also be suitable to study the interaction of the Ccr4-Not complex with other interactors.

Bibliography

Adrian, M., Dubochet, J., Lepault, J., & McDowall, A. W. Cryo-electron microscopy of viruses. *Nature* **308**(5954):32–36 (1984).

Albert, T. K., Hanzawa, H., Legtenberg, Y. I., de Ruwe, M. J., van den Heuvel, F. A., Collart, M. A., Boelens, R., & Timmers, H. T. M. Identification of a ubiquitin–protein ligase subunit within the CCR4–NOT transcription repressor complex. *The EMBO journal* **21**(3):355–364 (2002).

Alles, J., Legnini, I., Pacelli, M., & Rajewsky, N. Rapid nuclear deadenylation of mammalian messenger RNA. *bioRxiv* (2021).

Ameres, S. L. & Zamore, P. D. Diversifying microRNA sequence and function. *Nature reviews Molecular cell biology* **14**(8):475–488 (2013).

Andrade, M. A. & Bork, P. HEAT repeats in the Huntington's disease protein. *Nature genetics* **11**(2):115–116 (1995).

Aslanidis, C. & De Jong, P. J. Ligation-independent cloning of PCR products (LIC-PCR). *Nucleic acids research* **18**(20):6069–6074 (1990).

Baer, B. W. & Kornberg, R. D. Repeating structure of cytoplasmic poly (A)-ribonucleoprotein. *Proceedings of the National Academy of Sciences* **77**(4):1890–1892 (1980).

Baer, B. W. & Kornberg, R. D. The protein responsible for the repeating structure of cytoplasmic poly (A)-ribonucleoprotein. *Journal of Cell Biology* **96**(3):717–721 (1983).

Bai, Y., Salvadore, C., Chiang, Y.-C., Collart, M. A., Liu, H.-Y., & Denis, C. L. The CCR4 and CAF1 proteins of the CCR4-NOT complex are physically and functionally separated from NOT2, NOT4, and NOT5. *Molecular and cellular biology* **19**(10):6642–6651 (1999).

Bakheet, T., Williams, B. R., & Khabar, K. S. ARED 3.0: the large and diverse AU-rich transcriptome. *Nucleic acids research* **34**(suppl_1):D111–D114 (2006).

Barckmann, B. & Simonelig, M. Control of maternal mRNA stability in germ cells and early embryos. *Biochimica Et Biophysica Acta (BBA)-Gene Regulatory Mechanisms* **1829**(6-7):714–724 (2013).

Basquin, J., Roudko, V. V., Rode, M., Basquin, C., Séraphin, B., & Conti, E. Architecture of the nuclease module of the yeast Ccr4-not complex: the Not1-Caf1-Ccr4 interaction. *Molecular cell* **48**(2):207–218 (2012).

Bawankar, P., Loh, B., Wohlbold, L., Schmidt, S., & Izaurralde, E. NOT10 and C2orf29/NOT11 form a conserved module of the CCR4-NOT complex that docks onto the NOT1 N-terminal domain. *RNA biology* **10**(2):228–244 (2013).

Bazzini, A. A., Del Viso, F., Moreno-Mateos, M. A., Johnstone, T. G., Vejnar, C. E., Qin, Y., Yao, J., Khokha, M. K., & Giraldez, A. J. Codon identity regulates mRNA stability and translation efficiency during the maternal-to-zygotic transition. *The EMBO journal* **35**(19):2087–2103 (2016).

Benjamin, D. & Moroni, C. mRNA stability and cancer: an emerging link? *Expert opinion on biological therapy* **7**(10):1515–1529 (2007).

Bepler, T., Morin, A., Rapp, M., Brasch, J., Shapiro, L., Noble, A. J., & Berger, B. Positive-unlabeled convolutional neural networks for particle picking in cryo-electron micrographs. *Nature methods* **16**(11):1153–1160 (2019).

Bernstein, P., Peltz, S., & Ross, J. The poly (A)-poly (A)-binding protein complex is a major determinant of mRNA stability in vitro. *Molecular and cellular biology* **9**(2):659–670 (1989).

Bertani, G. Studies on lysogenesis I: the mode of phage liberation by lysogenic Escherichia coli. *Journal of bacteriology* **62**(3):293–300 (1951).

Bhandari, D., Raisch, T., Weichenrieder, O., Jonas, S., & Izaurralde, E. Structural basis for the Nanos-mediated recruitment of the CCR4–NOT complex and translational repression. *Genes & development* **28**(8):888–901 (2014).

Bhaskar, V., Basquin, J., & Conti, E. Architecture of the ubiquitylation module of the yeast Ccr4-Not complex. *Structure* **23**(5):921–928 (2015).

Bhaskar, V., Roudko, V., Basquin, J., Sharma, K., Urlaub, H., Séraphin, B., & Conti, E. Structure and RNA-binding properties of the Not1–Not2–Not5 module of the yeast Ccr4–Not complex. *Nature structural & molecular biology* **20**(11):1281–1288 (2013).

Blobel, G. A protein of molecular weight 78,000 bound to the polyadenylate region of eukaryotic messenger RNAs. *Proceedings of the National Academy of Sciences* **70**(3):924–928 (1973).

Boeck, R., Tarun, S., Rieger, M., Deardorff, J. A., Müller-Auer, S., & Sachs, A. B. The Yeast Pan2 Protein Is Required for Poly (A)-binding Protein-stimulated Poly (A)-nuclease Activity. *Journal of Biological Chemistry* **271**(1):432–438 (1996).

Boland, A., Chen, Y., Raisch, T., Jonas, S., Kuzuoğlu-Öztürk, D., Wohlbold, L., Weichenrieder, O., & Izaurralde, E. Structure and assembly of the NOT module of the human CCR4–NOT complex. *Nature structural & molecular biology* **20**(11):1289–1297 (2013).

Braun, J. E., Huntzinger, E., Fauser, M., & Izaurralde, E. GW182 proteins directly recruit cytoplasmic deadenylase complexes to miRNA targets. *Molecular cell* **44**(1):120–133 (2011).

Braun, J. E., Huntzinger, E., & Izaurralde, E. The role of GW182 proteins in miRNA-mediated gene silencing. *Ten years of progress in GW/P body research* pages 147–163 (2013).

Brook, M., Tchen, C. R., Santalucia, T., McIlrath, J., Arthur, J. S. C., Saklatvala, J., & Clark, A. R. Posttranslational regulation of tristetraprolin subcellular localization and protein stability by p38 mitogen-activated protein kinase and extracellular signal-regulated kinase pathways. *Molecular and cellular biology* **26**(6):2408–2418 (2006).

Brower, P. T., Gizang, E., Boreen, S. M., & Schultz, R. M. Biochemical studies of mammalian oogenesis: synthesis and stability of various classes of RNA during growth of the mouse oocyte in vitro. *Developmental biology* **86**(2):373–383 (1981).

Bulbrook, D., Brazier, H., Mahajan, P., Kliszczak, M., Fedorov, O., Marchese, F., Aubareda, A., Chalk, R., Picaud, S., Strain-Damerell, C. *et al.* Tryptophan-mediated interactions between tristetraprolin and the CNOT9 subunit are required for CCR4-NOT deadenylase complex recruitment. *Journal of molecular biology* **430**(5):722–736 (2018).

Burd, C. G., Matunis, E. L., & Dreyfuss, G. The multiple RNA-binding domains of the mRNA poly (A)-binding protein have different RNA-binding activities. *Molecular and cellular biology* **11**(7):3419–3424 (1991).

Burow, D. A., Martin, S., Quail, J. F., Alhusaini, N., Coller, J., & Cleary, M. D. Attenuated codon optimality contributes to neural-specific mRNA decay in Drosophila. *Cell reports* **24**(7):1704–1712 (2018).

Buschauer, R., Matsuo, Y., Sugiyama, T., Chen, Y.-H., Alhusaini, N., Sweet, T., Ikeuchi, K., Cheng, J., Matsuki, Y., Nobuta, R. *et al.* The Ccr4-Not complex monitors the translating ribosome for codon optimality. *Science* **368**(6488) (2020).

Cano, F., Rapiteanu, R., Sebastiaan Winkler, G., & Lehner, P. J. A non-proteolytic role for ubiquitin in deadenylation of MHC-I mRNA by the RNA-binding E3-ligase MEX-3C. *Nature communications* **6**(1):1–8 (2015).

Carreno, A. & Lykke-Andersen, J. The Conserved CNOT1 Interaction Motif of Tristetraprolin Regulates ARE-mRNA Decay Independently of the p38 MAPK-MK2 Kinase Pathway. *bioRxiv* (2022).

Chang, C.-T., Muthukumar, S., Weber, R., Levdansky, Y., Chen, Y., Bhandari, D., Igreja, C., Wohlbold, L., Valkov, E., & Izaurralde, E. A low-complexity region in human XRN1 directly recruits deadenylation and decapping factors in 5–3 messenger RNA decay. *Nucleic Acids Research* **47**(17):9282–9295 (2019).

Chang, H., Lim, J., Ha, M., & Kim, V. N. TAIL-seq: genome-wide determination of poly (A) tail length and 3 end modifications. *Molecular cell* **53**(6):1044–1052 (2014).

Chang, H., Yeo, J., Kim, J.-g., Kim, H., Lim, J., Lee, M., Kim, H. H., Ohk, J., Jeon, H.-Y., Lee, H. *et al.* Terminal uridylyltransferases execute programmed clearance of maternal transcriptome in vertebrate embryos. *Molecular cell* **70**(1):72–82 (2018).

Chekulaeva, M., Mathys, H., Zipprich, J. T., Attig, J., Colic, M., Parker, R., & Filipowicz, W. miRNA repression involves GW182-mediated recruitment of CCR4–NOT through conserved W-containing motifs. *Nature structural & molecular biology* **18**(11):1218–1226 (2011).

Chen, C.-Y. A. & Shyu, A.-B. AU-rich elements: characterization and importance in mRNA degradation. *Trends in biochemical sciences* **20**(11):465–470 (1995).

Chen, C.-Y. A. & Shyu, A.-B. Mechanisms of deadenylation-dependent decay. *Wiley Interdisciplinary Reviews: RNA* **2**(2):167–183 (2011).

Chen, J., Rappsilber, J., Chiang, Y.-C., Russell, P., Mann, M., & Denis, C. L. Purification and characterization of the 1.0 MDa CCR4-NOT complex identifies two novel components of the complex. *Journal of molecular biology* **314**(4):683–694 (2001).

Chen, Y., Boland, A., Kuzuoğlu-Öztürk, D., Bawankar, P., Loh, B., Chang, C.-T., Weichenrieder, O., & Izaurralde, E. A DDX6-CNOT1 complex and W-binding pockets in CNOT9 reveal direct links between miRNA target recognition and silencing. *Molecular cell* **54**(5):737–750 (2014).

Chen, Y., Khazina, E., Izaurralde, E., & Weichenrieder, O. Crystal structure and functional properties of the human CCR4-CAF1 deadenylase complex. *Nucleic Acids Research* **49**(11):6489–6510 (2021).

Chicoine, J., Benoit, P., Gamberi, C., Paliouras, M., Simonelig, M., & Lasko, P. Bicaudal-C recruits CCR4-NOT deadenylase to target mRNAs and regulates oogenesis, cytoskeletal organization, and its own expression. *Developmental cell* **13**(5):691–704 (2007).

Chlebowski, A., Lubas, M., Jensen, T. H., & Dziembowski, A. RNA decay machines: the exosome. *Biochimica et Biophysica Acta (BBA)-Gene Regulatory Mechanisms* **1829**(6-7):552–560 (2013).

Christie, M., Boland, A., Huntzinger, E., Weichenrieder, O., & Izaurralde, E. Structure of the PAN3 pseudokinase reveals the basis for interactions with the PAN2 deadenylase and the GW182 proteins. *Molecular cell* **51**(3):360–373 (2013).

Chu, C.-y. & Rana, T. M. Translation repression in human cells by microRNA-induced gene silencing requires RCK/p54. *PLoS biology* **4**(7):e210 (2006).

Clement, S. L., Scheckel, C., Stoecklin, G., & Lykke-Andersen, J. Phosphorylation of tristetraprolin by MK2 impairs AU-rich element mRNA decay by preventing deadenylase recruitment. *Molecular and cellular biology* **31**(2):256–266 (2011).

Coburn, G. A. & Mackie, G. A. Degradation of mRNA in Escherichia coli: an old problem with some new twists. *Progress in nucleic acid research and molecular biology* **62**:55–108 (1998).

Collart, M. A. & Panasenko, O. O. The Ccr4–not complex. *Gene* **492**(1):42–53 (2012).

Collart, M. A., Panasenko, O. O., & Nikolaev, S. I. The Not3/5 subunit of the Ccr4-Not complex: a central regulator of gene expression that integrates signals between the cytoplasm and the nucleus in eukaryotic cells. *Cellular signalling* **25**(4):743–751 (2013).

Collart, M. A. & Struhl, K. NOT1 (CDC39), NOT2 (CDC36), NOT3, and NOT4 encode a global-negative regulator of transcription that differentially affects TATA-element utilization. *Genes & development* **8**(5):525–537 (1994).

Coller, J. M., Tucker, M., Sheth, U., Valencia-Sanchez, M. A., & Parker, R. The DEAD box helicase, Dhh1p, functions in mRNA decapping and interacts with both the decapping and deadenylase complexes. *Rna* **7**(12):1717–1727 (2001).

Copeland, P. R. & Wormington, M. The mechanism and regulation of deadenylation: identification and characterization of Xenopus PARN. *Rna* **7**(6):875–886 (2001).

Cowling, V. H. Regulation of mRNA cap methylation. *Biochemical Journal* **425**(2):295–302 (2010).

Darnell, J., Wall, R., & Tushinski, R. An adenylic acid-rich sequence in messenger RNA of HeLa cells and its possible relationship to reiterated sites in DNA. *Proceedings of the National Academy of Sciences* **68**(6):1321–1325 (1971).

Daugeron, M.-C., Mauxion, F., & Séraphin, B. The yeast POP2 gene encodes a nuclease involved in mRNA deadenylation. *Nucleic acids research* **29**(12):2448–2455 (2001).

Decker, C. J. & Parker, R. A turnover pathway for both stable and unstable mRNAs in yeast: evidence for a requirement for deadenylation. *Genes & development* **7**(8):1632–1643 (1993).

Denis, C. L. Identification of new genes involved in the regulation of yeast alcohol dehydrogenase II. *Genetics* **108**(4):833–844 (1984).

Denis, C. L. & Malvar, T. The CCR4 gene from Saccharomyces cerevisiae is required for both nonfermentative and spt-mediated gene expression. *Genetics* **124**(2):283–291 (1990).

Dimitrova, L. N., Kuroha, K., Tatematsu, T., & Inada, T. Nascent peptide-dependent translation arrest leads to Not4p-mediated protein degradation by the proteasome. *Journal of Biological Chemistry* **284**(16):10343–10352 (2009).

D'Imprima, E., Floris, D., Joppe, M., Sánchez, R., Grininger, M., & Kühlbrandt, W. Protein denaturation at the air-water interface and how to prevent it. *Elife* **8**:e42747 (2019).

Dominski, Z. & Marzluff, W. F. Formation of the 3 end of histone mRNA. *Gene* **239**(1):1–14 (1999).

Draper, M. P., Salvadore, C., & Denis, C. L. Identification of a mouse protein whose homolog in Saccharomyces cerevisiae is a component of the CCR4 transcriptional regulatory complex. *Molecular and cellular biology* **15**(7):3487–3495 (1995).

Dreyfus, M. & Régnier, P. The poly (A) tail of mRNAs: bodyguard in eukaryotes, scavenger in bacteria. *Cell* **111**(5):611–613 (2002).

Du, H., Zhao, Y., He, J., Zhang, Y., Xi, H., Liu, M., Ma, J., & Wu, L. YTHDF2 destabilizes m6A-containing RNA through direct recruitment of the CCR4–NOT deadenylase complex. *Nature communications* **7**(1):1–11 (2016).

Dubochet, J. & McDowall, A. Vitrification of pure water for electron microscopy. *Journal of Microscopy* **124**(3):3–4 (1981).

Eaton, J. D., Francis, L., Davidson, L., & West, S. A unified allosteric/torpedo mechanism for transcriptional termination on human protein-coding genes. *Genes & development* **34**(1-2):132–145 (2020).

Eckmann, C. R., Rammelt, C., & Wahle, E. Control of poly (A) tail length. *Wiley Interdisciplinary Reviews: RNA* **2**(3):348–361 (2011).

Edmonds, M., Vaughan, M. H., & Nakazato, H. Polyadenylic acid sequences in the heterogeneous nuclear RNA and rapidly-labeled polyribosomal RNA of HeLa cells: possible evidence for a precursor relationship. *Proceedings of the National Academy of Sciences* **68**(6):1336–1340 (1971).

Eichhorn, S. W., Subtelny, A. O., Kronja, I., Kwasnieski, J. C., Orr-Weaver, T. L., & Bartel, D. P. mRNA poly (A)-tail changes specified by deadenylation broadly reshape translation in Drosophila oocytes and early embryos. *Elife* **5**:e16955 (2016).

Eisen, T. J., Eichhorn, S. W., Subtelny, A. O., Lin, K. S., McGeary, S. E., Gupta, S., & Bartel, D. P. The dynamics of cytoplasmic mRNA metabolism. *Molecular cell* **77**(4):786–799 (2020).

Enwerem, I. I., Elrod, N. D., Chang, C.-T., Lin, A., Ji, P., Bohn, J. A., Levdansky, Y., Wagner, E. J., Valkov, E., & Goldstrohm, A. C. Human Pumilio proteins directly bind the CCR4-NOT deadenylase complex to regulate the transcriptome. *Rna* **27**(4):445–464 (2021).

Erben, E., Chakraborty, C., & Clayton, C. The CAF1-NOT complex of trypanosomes. *Frontiers in genetics* **4**:299 (2014).

Fabian, M. R., Cieplak, M. K., Frank, F., Morita, M., Green, J., Srikumar, T., Nagar, B., Yamamoto, T., Raught, B., Duchaine, T. F. *et al.* miRNA-mediated deadenylation is orchestrated by GW182 through two conserved motifs that interact with CCR4–NOT. *Nature structural & molecular biology* **18**(11):1211–1217 (2011).

Fabian, M. R., Frank, F., Rouya, C., Siddiqui, N., Lai, W. S., Karetnikov, A., Blackshear, P. J., Nagar, B., & Sonenberg, N. Structural basis for the recruitment of the human CCR4–NOT deadenylase complex by tristetraprolin. *Nature structural & molecular biology* **20**(6):735–739 (2013).

Fabian, M. R. & Sonenberg, N. The mechanics of miRNA-mediated gene silencing: a look under the hood of miRISC. *Nature structural & molecular biology* **19**(6):586–593 (2012).

Ford, L. P., Bagga, P. S., & Wilusz, J. The poly (A) tail inhibits the assembly of a 3'-to-5'exonuclease in an in vitro RNA stability system. *Molecular and cellular biology* **17**(1):398–406 (1997).

Fu, R., Olsen, M. T., Webb, K., Bennett, E. J., & Lykke-Andersen, J. Recruitment of the 4EHP-GYF2 cap-binding complex to tetraproline motifs of tristetraprolin promotes repression and degradation of mRNAs with AU-rich elements. *Rna* **22**(3):373–382 (2016).

Fuke, H. & Ohno, M. Role of poly (A) tail as an identity element for mRNA nuclear export. *Nucleic acids research* **36**(3):1037–1049 (2008).

Garces, R. G., Gillon, W., & Pai, E. F. Atomic model of human Rcd-1 reveals an armadillo-like-repeat protein with in vitro nucleic acid binding properties. *Protein science* **16**(2):176–188 (2007).

Garneau, N. L., Wilusz, J., & Wilusz, C. J. The highways and byways of mRNA decay. *Nature reviews Molecular cell biology* **8**(2):113–126 (2007).

Geisberg, J. V., Moqtaderi, Z., Fan, X., Ozsolak, F., & Struhl, K. Global analysis of mRNA isoform half-lives reveals stabilizing and destabilizing elements in yeast. *Cell* **156**(4):812–824 (2014).

Geisler, S. & Coller, J. XRN1: a Major 5 to 3 exoribonuclease in eukaryotic cells. *The Enzymes* **31**:97–114 (2012).

Gibson, D. G., Young, L., Chuang, R.-Y., Venter, J. C., Hutchison, C. A., & Smith, H. O. Enzymatic assembly of DNA molecules up to several hundred kilobases. *Nature methods* **6**(5):343–345 (2009).

Glaeser, R. M., Nogales, E., & Chiu, W. *Single-particle Cryo-EM of biological macromolecules* (IOP Publishing, 2021).

Gordon, D. E., Watson, A., Roguev, A., Zheng, S., Jang, G. M., Kane, J., Xu, J., Guo, J. Z., Stevenson, E., Swaney, D. L. *et al.* A quantitative genetic interaction map of HIV infection. *Molecular cell* **78**(2):197–209 (2020).

Görlach, M., Burd, C. G., & Dreyfuss, G. The mRNA poly (A)-binding protein: localization, abundance, and RNA-binding specificity. *Experimental cell research* **211**(2):400–407 (1994).

Gruber, A. J. & Zavolan, M. Alternative cleavage and polyadenylation in health and disease. *Nature Reviews Genetics* **20**(10):599–614 (2019).

Grudzien-Nogalska, E. & Kiledjian, M. New insights into decapping enzymes and selective mRNA decay. *Wiley Interdisciplinary Reviews: RNA* **8**(1):e1379 (2017).

Hanson, G. & Coller, J. Codon optimality, bias and usage in translation and mRNA decay. *Nature reviews Molecular cell biology* **19**(1):20–30 (2018).

Hata, H., Mitsui, H., Liu, H., Bai, Y., Denis, C. L., Shimizu, Y., & Sakai, A. Dhh1p, a putative RNA helicase, associates with the general transcription factors Pop2p and Ccr4p from Saccharomyces cerevisiae. *Genetics* **148**(2):571–579 (1998).

He, F., Celik, A., Wu, C., & Jacobson, A. General decapping activators target different subsets of inefficiently translated mRNAs. *Elife* **7**:e34409 (2018).

Herrick, D., Parker, R., & Jacobson, A. Identification and comparison of stable and unstable mRNAs in Saccharomyces cerevisiae. *Molecular and cellular biology* **10**(5):2269–2284 (1990).

Horiuchi, M., Takeuchi, K., Noda, N., Muroya, N., Suzuki, T., Nakamura, T., Kawamura-Tsuzuku, J., Takahasi, K., Yamamoto, T., & Inagaki, F. Structural basis for the antiproliferative activity of the Tob-hCaf1 complex. *Journal of biological chemistry* **284**(19):13244–13255 (2009).

Houseley, J. & Tollervey, D. The many pathways of RNA degradation. *Cell* **136**(4):763–776 (2009).

Huntzinger, E. & Izaurralde, E. Gene silencing by microRNAs: contributions of translational repression and mRNA decay. *Nature Reviews Genetics* **12**(2):99–110 (2011).

Huntzinger, E., Kashima, I., Fauser, M., Saulière, J., & Izaurralde, E. SMG6 is the catalytic endonuclease that cleaves mRNAs containing nonsense codons in metazoan. *Rna* **14**(12):2609–2617 (2008).

Imataka, H., Gradi, A., & Sonenberg, N. A newly identified N-terminal amino acid sequence of human eIF4G binds poly (A)-binding protein and functions in poly (A)-dependent translation. *The EMBO journal* **17**(24):7480–7489 (1998).

Inglis, A. J., Guna, A., Merchan, A. G., Pal, A., Esantsi, T. K., Keys, H. R., Frenkel, E. M., Oania, R., Weissman, J. S., & Voorhees, R. M. Coupled protein quality control during nonsense mediated mRNA decay. *bioRxiv* (2021).

Johnson, B. A., Stehn, J. R., Yaffe, M. B., & Blackwell, T. K. Cytoplasmic localization of tristetraprolin involves 14-3-3-dependent and-independent mechanisms. *Journal of Biological Chemistry* **277**(20):18029–18036 (2002).

Jonas, S., Christie, M., Peter, D., Bhandari, D., Loh, B., Huntzinger, E., Weichenrieder, O., & Izaurralde, E. An asymmetric PAN3 dimer recruits a single PAN2 exonuclease to mediate mRNA deadenylation and decay. *Nature structural & molecular biology* **21**(7):599–608 (2014).

Jonas, S. & Izaurralde, E. Towards a molecular understanding of microRNA-mediated gene silencing. *Nature reviews genetics* **16**(7):421–433 (2015).

Jones, C. I., Zabolotskaya, M. V., & Newbury, S. F. The 5→ 3 exoribonuclease XRN1/Pacman and its functions in cellular processes and development. *Wiley Interdisciplinary Reviews: RNA* **3**(4):455–468 (2012).

Jumper, J., Evans, R., Pritzel, A., Green, T., Figurnov, M., Ronneberger, O., Tunyasuvunakool, K., Bates, R., Žídek, A., Potapenko, A. *et al.* Highly accurate protein structure prediction with AlphaFold. *Nature* **596**(7873):583–589 (2021).

Kahvejian, A., Svitkin, Y. V., Sukarieh, R., M'Boutchou, M.-N., & Sonenberg, N. Mammalian poly (A)-binding protein is a eukaryotic translation initiation factor, which acts via multiple mechanisms. *Genes & development* **19**(1):104–113 (2005).

Kajjo, S., Sharma, S., Chen, S., Brothers, W. R., Cott, M., Hasaj, B., Jovanovic, P., Larsson, O., & Fabian, M. R. PABP prevents the untimely decay of select mRNA populations in human cells. *The EMBO Journal* **41**(6):e108650 (2022).

Kapp, L. D. & Lorsch, J. R. The molecular mechanics of eukaryotic translation. *Annual review of biochemistry* **73**(1):657–704 (2004).

Kastner, B., Fischer, N., Golas, M. M., Sander, B., Dube, P., Boehringer, D., Hartmuth, K., Deckert, J., Hauer, F., Wolf, E. *et al.* GraFix: sample preparation for single-particle electron cryomicroscopy. *Nature methods* **5**(1):53–55 (2008).

Keller, R. W., Kühn, U., Aragón, M., Bornikova, L., Wahle, E., & Bear, D. G. The nuclear poly (A) binding protein, PABP2, forms an oligomeric particle covering the length of the poly (A) tail. *Journal of molecular biology* **297**(3):569–583 (2000).

Keskeny, C., Raisch, T., Sgromo, A., Igreja, C., Bhandari, D., Weichenrieder, O., & Izaurralde, E. A conserved CAF40-binding motif in metazoan NOT4 mediates association with the CCR4–NOT complex. *Genes & development* **33**(3-4):236–252 (2019).

Kessler, S. H. & Sachs, A. B. RNA recognition motif 2 of yeast Pab1p is required for its functional interaction with eukaryotic translation initiation factor 4G. *Molecular and cellular biology* **18**(1):51–57 (1998).

Kim, Y. K. & Maquat, L. E. UPFront and center in RNA decay: UPF1 in nonsense-mediated mRNA decay and beyond. *Rna* **25**(4):407–422 (2019).

Klykov, O., Steigenberger, B., Pektaş, S., Fasci, D., Heck, A. J., & Scheltema, R. A. Efficient and robust proteome-wide approaches for cross-linking mass spectrometry. *Nature protocols* **13**(12):2964–2990 (2018).

Körner, C. G. & Wahle, E. Poly (A) tail shortening by a mammalian poly (A)-specific 3-exoribonuclease. *Journal of Biological Chemistry* **272**(16):10448–10456 (1997).

Kosinski, J., von Appen, A., Ori, A., Karius, K., Müller, C. W., & Beck, M. Xlink Analyzer: software for analysis and visualization of cross-linking data in the context of three-dimensional structures. *Journal of structural biology* **189**(3):177–183 (2015).

Kühn, U., Buschmann, J., & Wahle, E. The nuclear poly (A) binding protein of mammals, but not of fission yeast, participates in mRNA polyadenylation. *RNA* **23**(4):473–482 (2017).

Kulak, N. A., Geyer, P. E., & Mann, M. Loss-less nano-fractionator for high sensitivity, high coverage proteomics. *Molecular & Cellular Proteomics* **16**(4):694–705 (2017).

Kurosaki, T., Popp, M. W., & Maquat, L. E. Quality and quantity control of gene expression by nonsense-mediated mRNA decay. *Nature reviews Molecular cell biology* **20**(7):406–420 (2019).

Lai, W. S., Carballo, E., Thorn, J. M., Kennington, E. A., & Blackshear, P. J. Interactions of CCCH zinc finger proteins with mRNA: binding of tristetraprolin-related zinc finger proteins to Au-rich elements and destabilization of mRNA. *Journal of Biological Chemistry* **275**(23):17827–17837 (2000).

Lau, N.-C., Kolkman, A., van Schaik, F. M., Mulder, K. W., Pijnappel, W. P., Heck, A. J., & Timmers, H. T. M. Human Ccr4–Not complexes contain variable deadenylase subunits. *Biochemical Journal* **422**(3):443–453 (2009).

Lee, R. C., Feinbaum, R. L., & Ambros, V. The C. elegans heterochronic gene lin-4 encodes small RNAs with antisense complementarity to lin-14. *cell* **75**(5):843–854 (1993).

Lee, S. Y., Mendecki, J., & Brawerman, G. A polynucleotide segment rich in adenylic acid in the rapidly-labeled polyribosomal RNA component of mouse sarcoma 180 ascites cells. *Proceedings of the National Academy of Sciences* **68**(6):1331–1335 (1971).

Legnini, I., Alles, J., Karaiskos, N., Ayoub, S., & Rajewsky, N. FLAM-seq: full-length mRNA sequencing reveals principles of poly (A) tail length control. *Nature methods* **16**(9):879–886 (2019).

Leppek, K., Schott, J., Reitter, S., Poetz, F., Hammond, M. C., & Stoecklin, G. Roquin promotes constitutive mRNA decay via a conserved class of stem-loop recognition motifs. *Cell* **153**(4):869–881 (2013).

Lim, J., Ha, M., Chang, H., Kwon, S. C., Simanshu, D. K., Patel, D. J., & Kim, V. N. Uridylation by TUT4 and TUT7 marks mRNA for degradation. *Cell* **159**(6):1365–1376 (2014).

Lim, J., Kim, D., Lee, Y.-s., Ha, M., Lee, M., Yeo, J., Chang, H., Song, J., Ahn, K., & Kim, V. N. Mixed tailing by TENT4A and TENT4B shields mRNA from rapid deadenylation. *Science* **361**(6403):701–704 (2018).

Lim, J., Lee, M., Son, A., Chang, H., & Kim, V. N. mTAIL-seq reveals dynamic poly (A) tail regulation in oocyte-to-embryo development. *Genes & development* **30**(14):1671–1682 (2016).

Lima, S. A., Chipman, L. B., Nicholson, A. L., Chen, Y.-H., Yee, B. A., Yeo, G. W., Coller, J., & Pasquinelli, A. E. Short poly (A) tails are a conserved feature of highly expressed genes. *Nature structural & molecular biology* **24**(12):1057–1063 (2017).

Liu, H.-Y., Badarinarayana, V., Audino, D. C., Rappsilber, J., Mann, M., & Denis, C. L. The NOT proteins are part of the CCR4 transcriptional complex and affect gene expression both positively and negatively. *The EMBO journal* **17**(4):1096–1106 (1998).

López de Silanes, I., Paz Quesada, M., & Esteller, M. Aberrant regulation of messenger RNA 3-untranslated region in human cancer. *Analytical Cellular Pathology* **29**(1):1–17 (2007).

Lykke-Andersen, J. & Wagner, E. Recruitment and activation of mRNA decay enzymes by two ARE-mediated decay activation domains in the proteins TTP and BRF-1. *Genes & development* **19**(3):351–361 (2005).

Maillet, L. & Collart, M. A. Interaction between Not1p, a component of the Ccr4-not complex, a global regulator of transcription, and Dhh1p, a putative RNA helicase. *Journal of Biological Chemistry* **277**(4):2835–2842 (2002).

Makino, D. L., Halbach, F., & Conti, E. The RNA exosome and proteasome: common principles of degradation control. *Nature reviews Molecular cell biology* **14**(10):654–660 (2013).

Mastronarde, D. N. SerialEM: a program for automated tilt series acquisition on Tecnai microscopes using prediction of specimen position. *Microscopy and Microanalysis* **9**(S02):1182–1183 (2003).

Mathys, H., Basquin, J., Ozgur, S., Czarnocki-Cieciura, M., Bonneau, F., Aartse, A., Dziembowski, A., Nowotny, M., Conti, E., & Filipowicz, W. Structural and biochemical insights to the role of the CCR4-NOT complex and DDX6 ATPase in microRNA repression. *Molecular cell* **54**(5):751–765 (2014).

Mauger, D. M., Cabral, B. J., Presnyak, V., Su, S. V., Reid, D. W., Goodman, B., Link, K., Khatwani, N., Reynders, J., Moore, M. J. *et al.* mRNA structure regulates protein expression through changes in functional half-life. *Proceedings of the National Academy of Sciences* **116**(48):24075–24083 (2019).

Mauxion, F., Chen, C.-Y. A., Séraphin, B., & Shyu, A.-B. BTG/TOB factors impact deadenylases. *Trends in biochemical sciences* **34**(12):640–647 (2009).

Mauxion, F., Faux, C., & Séraphin, B. The BTG2 protein is a general activator of mRNA deadenylation. *The EMBO journal* **27**(7):1039–1048 (2008).

Mauxion, F., Prève, B., & Séraphin, B. C2ORF29/CNOT11 and CNOT10 form a new module of the CCR4-NOT complex. *RNA biology* **10**(2):267–276 (2013).

McLaughlin, C. S., Warner, J. R., Edmonds, M., Nakazato, H., & Vaughan, M. H. Polyadenylic acid sequences in yeast messenger ribonucleic acid. *Journal of Biological Chemistry* **248**(4):1466–1471 (1973).

Melo, E. O., Dhalia, R., de Sa, C. M., Standart, N., & de Melo Neto, O. P. Identification of a C-terminal poly (A)-binding protein (PABP)-PABP interaction domain: role in cooperative binding to poly (A) and efficient cap distal translational repression. *Journal of Biological Chemistry* **278**(47):46357–46368 (2003).

Merkley, E. D., Rysavy, S., Kahraman, A., Hafen, R. P., Daggett, V., & Adkins, J. N. Distance restraints from crosslinking mass spectrometry: mining a molecular dynamics simulation database to evaluate lysine–lysine distances. *Protein science* **23**(6):747–759 (2014).

Mersman, D. P., Du, H.-N., Fingerman, I. M., South, P. F., & Briggs, S. D. Polyubiquitination of the demethylase Jhd2 controls histone methylation and gene expression. *Genes & development* **23**(8):951–962 (2009).

Meyer, S., Temme, C., & Wahle, E. Messenger RNA turnover in eukaryotes: pathways and enzymes. *Critical reviews in biochemistry and molecular biology* **39**(4):197–216 (2004).

Miller, J. E. & Reese, J. C. Ccr4-Not complex: the control freak of eukaryotic cells. *Critical reviews in biochemistry and molecular biology* **47**(4):315–333 (2012).

Miller, J. H. Experiments in molecular genetics (1972).

Mitchell, P., Petfalski, E., Shevchenko, A., Mann, M., & Tollervey, D. The exosome: a conserved eukaryotic RNA processing complex containing multiple 3→ 5 exoribonucleases. *Cell* **91**(4):457–466 (1997).

Mitchell, S. F., Walker, S. E., Algire, M. A., Park, E.-H., Hinnebusch, A. G., & Lorsch, J. R. The 5-7-methylguanosine cap on eukaryotic mRNAs serves both to stimulate canonical translation initiation and to block an alternative pathway. *Molecular cell* **39**(6):950–962 (2010).

Morgan, M., Much, C., DiGiacomo, M., Azzi, C., Ivanova, I., Vitsios, D. M., Pistolic, J., Collier, P., Moreira, P. N., Benes, V. *et al.* mRNA 3 uridylation and poly (A) tail length sculpt the mammalian maternal transcriptome. *Nature* **548**(7667):347–351 (2017).

Muhlrad, D. & Parker, R. The yeast EDC1 mRNA undergoes deadenylation-independent decapping stimulated by Not2p, Not4p, and Not5p. *The EMBO journal* **24**(5):1033–1045 (2005).

Mulder, K. W., Inagaki, A., Cameroni, E., Mousson, F., Winkler, G. S., De Virgilio, C., Collart, M. A., & Timmers, H. T. M. Modulation of Ubc4p/Ubc5p-mediated stress responses by the RING-finger-dependent ubiquitin-protein ligase Not4p in Saccharomyces cerevisiae. *Genetics* **176**(1):181–192 (2007).

Nasertorabi, F., Batisse, C., Diepholz, M., Suck, D., & Böttcher, B. Insights into the structure of the CCR4-NOT complex by electron microscopy. *FEBS letters* **585**(14):2182–2186 (2011).

Naydenova, K. & Russo, C. J. Measuring the effects of particle orientation to improve the efficiency of electron cryomicroscopy. *Nature communications* **8**(1):1–5 (2017).

Neuhold, J., Radakovics, K., Lehner, A., Weissmann, F., Garcia, M. Q., Romero, M. C., Berrow, N. S., & Stolt-Bergner, P. GoldenBac: a simple, highly efficient, and widely applicable system for construction of multi-gene expression vectors for use with the baculovirus expression vector system. *BMC biotechnology* **20**:1–15 (2020).

Noble, A. J., Dandey, V. P., Wei, H., Brasch, J., Chase, J., Acharya, P., Tan, Y. Z., Zhang, Z., Kim, L. Y., Scapin, G. *et al.* Routine single particle CryoEM sample and grid characterization by tomography. *Elife* **7**:e34257 (2018).

Oberholzer, U. & Collart, M. Characterization of NOT5 that encodes a new component of the Not protein complex. *Gene* **207**(1):61–69 (1998).

Orban, T. I. & Izaurralde, E. Decay of mRNAs targeted by RISC requires XRN1, the Ski complex, and the exosome. *Rna* **11**(4):459–469 (2005).

Ozgur, S., Basquin, J., Kamenska, A., Filipowicz, W., Standart, N., & Conti, E. Structure of a human 4E-T/DDX6/CNOT1 complex reveals the different interplay of DDX6-binding proteins with the CCR4-NOT complex. *Cell reports* **13**(4):703–711 (2015a).

Ozgur, S., Buchwald, G., Falk, S., Chakrabarti, S., Prabu, J. R., & Conti, E. The conformational plasticity of eukaryotic RNA-dependent ATP ases. *The FEBS journal* **282**(5):850–863 (2015b).

Ozgur, S., Chekulaeva, M., & Stoecklin, G. Human Pat1b connects deadenylation with mRNA decapping and controls the assembly of processing bodies. *Molecular and cellular biology* **30**(17):4308–4323 (2010).

Palovcak, E., Wang, F., Zheng, S. Q., Yu, Z., Li, S., Betegon, M., Bulkley, D., Agard, D. A., & Cheng, Y. A simple and robust procedure for preparing graphene-oxide cryo-EM grids. *Journal of structural biology* **204**(1):80–84 (2018).

Panasenko, O., Landrieux, E., Feuermann, M., Finka, A., Paquet, N., & Collart, M. A. The yeast Ccr4-Not complex controls ubiquitination of the nascent-associated polypeptide (NAC-EGD) complex. *Journal of Biological Chemistry* **281**(42):31389–31398 (2006).

Panasenko, O. O. & Collart, M. A. Presence of Not5 and ubiquitinated Rps7A in polysome fractions depends upon the Not4 E3 ligase. *Molecular microbiology* **83**(3):640–653 (2012).

Park, J.-E., Yi, H., Kim, Y., Chang, H., & Kim, V. N. Regulation of poly (A) tail and translation during the somatic cell cycle. *Molecular cell* **62**(3):462–471 (2016).

Parker, R. & Sheth, U. P bodies and the control of mRNA translation and degradation. *Molecular cell* **25**(5):635–646 (2007).

Passmore, L. A. & Coller, J. Roles of mRNA poly (A) tails in regulation of eukaryotic gene expression. *Nature Reviews Molecular Cell Biology* pages 1–14 (2021).

Petit, A.-P., Wohlbold, L., Bawankar, P., Huntzinger, E., Schmidt, S., Izaurralde, E., & Weichenrieder, O. The structural basis for the interaction between the CAF1 nuclease and the NOT1 scaffold of the human CCR4–NOT deadenylase complex. *Nucleic acids research* **40**(21):11058–11072 (2012).

Pettersen, E. F., Goddard, T. D., Huang, C. C., Couch, G. S., Greenblatt, D. M., Meng, E. C., & Ferrin, T. E. UCSF Chimera—a visualization system for exploratory research and analysis. *Journal of computational chemistry* **25**(13):1605–1612 (2004).

Piqué, M., López, J. M., Foissac, S., Guigó, R., & Méndez, R. A combinatorial code for CPE-mediated translational control. *Cell* **132**(3):434–448 (2008).

Poetz, F., Corbo, J., Levdansky, Y., Spiegelhalter, A., Lindner, D., Magg, V., Lebedeva, S., Schweiggert, J., Schott, J., Valkov, E. *et al.* RNF219 attenuates global mRNA decay through inhibition of CCR4-NOT complex-mediated deadenylation. *Nature Communications* **12**(1):1–19 (2021).

Presnyak, V., Alhusaini, N., Chen, Y.-H., Martin, S., Morris, N., Kline, N., Olson, S., Weinberg, D., Baker, K. E., Graveley, B. R. *et al.* Codon optimality is a major determinant of mRNA stability. *Cell* **160**(6):1111–1124 (2015).

Punjani, A., Rubinstein, J. L., Fleet, D. J., & Brubaker, M. A. cryoSPARC: algorithms for rapid unsupervised cryo-EM structure determination. *Nature methods* **14**(3):290–296 (2017).

Radhakrishnan, A., Chen, Y.-H., Martin, S., Alhusaini, N., Green, R., & Coller, J. The DEAD-box protein Dhh1p couples mRNA decay and translation by monitoring codon optimality. *Cell* **167**(1):122–132 (2016).

Radhakrishnan, A. & Green, R. Connections underlying translation and mRNA stability. *Journal of molecular biology* **428**(18):3558–3564 (2016).

Raisch, T., Chang, C.-T., Levdansky, Y., Muthukumar, S., Raunser, S., & Valkov, E. Reconstitution of recombinant human CCR4-NOT reveals molecular insights into regulated deadenylation. *Nature communications* **10**(1):1–14 (2019).

Reddy, R., Ro-Choi, T. S., Henning, D., & Busch, H. Primary sequence of U-1 nuclear ribonucleic acid of Novikoff hepatoma ascites cells. *Journal of Biological Chemistry* **249**(20):6486–6494 (1974).

Richter, J. D. Cytoplasmic polyadenylation in development and beyond. *Microbiology and molecular biology reviews* **63**(2):446–456 (1999).

Rissland, O. S. & Norbury, C. J. Decapping is preceded by 3 uridylation in a novel pathway of bulk mRNA turnover. *Nature structural & molecular biology* **16**(6):616–623 (2009).

Rosenthal, P. B. & Henderson, R. Optimal determination of particle orientation, absolute hand, and contrast loss in single-particle electron cryomicroscopy. *Journal of molecular biology* **333**(4):721–745 (2003).

Rouya, C., Siddiqui, N., Morita, M., Duchaine, T. F., Fabian, M. R., & Sonenberg, N. Human DDX6 effects miRNA-mediated gene silencing via direct binding to CNOT1. *Rna* **20**(9):1398–1409 (2014).

Sachs, A. B., Davis, R., & Kornberg, R. A single domain of yeast poly (A)-binding protein is necessary and sufficient for RNA binding and cell viability. *Molecular and cellular biology* **7**(9):3268–3276 (1987).

Sachs, A. B. & Davis, R. W. The poly (A) binding protein is required for poly (A) shortening and 60S ribosomal subunit-dependent translation initiation. *Cell* **58**(5):857–867 (1989).

Sakai, A., Chibazakura, T., Shimizu, Y., & Hishinuma, F. Molecular analysis of POP2 gene, a gene required for glucose-derepression of gene expression in Saccharomyces cerevisiae. *Nucleic Acids Research* **20**(23):6227–6233 (1992).

Sambrook, J. & Russell, D. Molecular cloning: a laboratory manual. *New York: Cold Spring Harbor* (2001).

Sandler, H., Kreth, J., Timmers, H. T. M., & Stoecklin, G. Not1 mediates recruitment of the deadenylase Caf1 to mRNAs targeted for degradation by tristetraprolin. *Nucleic acids research* **39**(10):4373–4386 (2011).

Sanduja, S., Blanco, F. F., Young, L. E., Kaza, V., & Dixon, D. A. The role of tristetraprolin in cancer and inflammation. *Frontiers in bioscience: a journal and virtual library* **17**:174 (2012).

Sari, D., Gupta, K., Raj, D. B. T. G., Aubert, A., Drncová, P., Garzoni, F., Fitzgerald, D., & Berger, I. The MultiBac baculovirus/insect cell expression vector system for producing complex protein biologics. *Advanced Technologies for Protein Complex Production and Characterization* pages 199–215 (2016).

Schäfer, I. B., Rode, M., Bonneau, F., Schüssler, S., & Conti, E. The structure of the Pan2–Pan3 core complex reveals cross-talk between deadenylase and pseudokinase. *Nature structural & molecular biology* **21**(7):591–598 (2014).

Schäfer, I. B., Yamashita, M., Schuller, J. M., Schüssler, S., Reichelt, P., Strauss, M., & Conti, E. Molecular basis for poly (A) RNP architecture and recognition by the Pan2-Pan3 deadenylase. *Cell* **177**(6):1619–1631 (2019).

Scheltema, R. A., Hauschild, J.-P., Lange, O., Hornburg, D., Denisov, E., Damoc, E., Kuehn, A., Makarov, A., & Mann, M. The Q Exactive HF, a Benchtop mass spectrometer with a pre-filter, high-performance quadrupole and an ultra-high-field Orbitrap analyzer. *Molecular & Cellular Proteomics* **13**(12):3698–3708 (2014).

Schindelin, J., Arganda-Carreras, I., Frise, E., Kaynig, V., Longair, M., Pietzsch, T., Preibisch, S., Rueden, C., Saalfeld, S., Schmid, B. *et al.* Fiji: an open-source platform for biological-image analysis. *Nature methods* **9**(7):676–682 (2012).

Schirle, N. T. & MacRae, I. J. The crystal structure of human Argonaute2. *Science* **336**(6084):1037–1040 (2012).

Schoenberg, D. R. & Maquat, L. E. Regulation of cytoplasmic mRNA decay. *Nature Reviews Genetics* **13**(4):246–259 (2012).

Schrödinger, LLC. The PyMOL Molecular Graphics System, Version 1.8 (2015).

Schwartz, D. C. & Parker, R. Mutations in translation initiation factors lead to increased rates of deadenylation and decapping of mRNAs in Saccharomyces cerevisiae. *Molecular and cellular biology* **19**(8):5247–5256 (1999).

Sgromo, A., Raisch, T., Backhaus, C., Keskeny, C., Alva, V., Weichenrieder, O., & Izaurralde, E. Drosophila Bag-of-marbles directly interacts with the CAF40 subunit of the CCR4–NOT complex to elicit repression of mRNA targets. *Rna* **24**(3):381–395 (2018).

Sgromo, A., Raisch, T., Bawankar, P., Bhandari, D., Chen, Y., Kuzuoğlu-Öztürk, D., Weichenrieder, O., & Izaurralde, E. A CAF40-binding motif facilitates recruitment of the CCR4-NOT complex to mRNAs targeted by Drosophila Roquin. *Nature communications* **8**(1):1–16 (2017).

Sharif, H., Ozgur, S., Sharma, K., Basquin, C., Urlaub, H., & Conti, E. Structural analysis of the yeast Dhh1–Pat1 complex reveals how Dhh1 engages Pat1, Edc3 and RNA in mutually exclusive interactions. *Nucleic acids research* **41**(17):8377–8390 (2013).

Sharma, S., Poetz, F., Bruer, M., Ly-Hartig, T. B. N., Schott, J., Séraphin, B., & Stoecklin, G. Acetylation-dependent control of global poly (A) RNA degradation by CBP/p300 and HDAC1/2. *Molecular cell* **63**(6):927–938 (2016).

Shatkin, A. Capping of eucaryotic mRNAs. *Cell* **9**(4):645–653 (1976).

Sheiness, D. & Darnell, J. E. Polyadenylic acid segment in mRNA becomes shorter with age. *Nature New Biology* **241**(113):265–268 (1973).

Sheth, U. & Parker, R. Decapping and decay of messenger RNA occur in cytoplasmic processing bodies. *Science* **300**(5620):805–808 (2003).

Shi, Y. & Manley, J. L. The end of the message: multiple protein–RNA interactions define the mRNA polyadenylation site. *Genes & development* **29**(9):889–897 (2015).

Shyu, A.-B., Wilkinson, M. F., & Van Hoof, A. Messenger RNA regulation: to translate or to degrade. *The EMBO journal* **27**(3):471–481 (2008).

Simón, E. & Séraphin, B. A specific role for the C-terminal region of the Poly (A)-binding protein in mRNA decay. *Nucleic acids research* **35**(18):6017–6028 (2007).

Siwaszek, A., Ukleja, M., & Dziembowski, A. Proteins involved in the degradation of cytoplasmic mRNA in the major eukaryotic model systems. *RNA biology* **11**(9):1122–1136 (2014).

Smith, R. W., Blee, T. K., & Gray, N. K. Poly (A)-binding proteins are required for diverse biological processes in metazoans. *Biochemical Society Transactions* **42**(4):1229–1237 (2014).

Sonn-Segev, A., Belacic, K., Bodrug, T., Young, G., VanderLinden, R. T., Schulman, B. A., Schimpf, J., Friedrich, T., Dip, P. V., Schwartz, T. U. *et al.* Quantifying the heterogeneity of macromolecular machines by mass photometry. *Nature communications* **11**(1):1–10 (2020).

Stowell, J. A., Webster, M. W., Kögel, A., Wolf, J., Shelley, K. L., & Passmore, L. A. Reconstitution of targeted deadenylation by the Ccr4-Not complex and the YTH domain protein Mmi1. *Cell reports* **17**(8):1978–1989 (2016).

Stupfler, B., Birck, C., Séraphin, B., & Mauxion, F. BTG2 bridges PABPC1 RNA-binding domains and CAF1 deadenylase to control cell proliferation. *Nature communications* **7**(1):1–11 (2016).

Subtelny, A. O., Eichhorn, S. W., Chen, G. R., Sive, H., & Bartel, D. P. Poly (A)-tail profiling reveals an embryonic switch in translational control. *Nature* **508**(7494):66–71 (2014).

Suzuki, A., Igarashi, K., Aisaki, K.-i., Kanno, J., & Saga, Y. NANOS2 interacts with the CCR4-NOT deadenylation complex and leads to suppression of specific RNAs. *Proceedings of the National Academy of Sciences* **107**(8):3594–3599 (2010).

Tang, G., Peng, L., Baldwin, P. R., Mann, D. S., Jiang, W., Rees, I., & Ludtke, S. J. EMAN2: an extensible image processing suite for electron microscopy. *Journal of structural biology* **157**(1):38–46 (2007).

Tang, T. T., Stowell, J. A., Hill, C. H., & Passmore, L. A. The intrinsic structure of poly (A) RNA determines the specificity of Pan2 and Caf1 deadenylases. *Nature structural & molecular biology* **26**(6):433–442 (2019).

Tarun, S. & Sachs, A. B. A common function for mRNA 5'and 3'ends in translation initiation in yeast. *Genes & development* **9**(23):2997–3007 (1995).

Taylor, K. A. & Glaeser, R. M. Electron diffraction of frozen, hydrated protein crystals. *Science* **186**(4168):1036–1037 (1974).

Taylor, K. A. & Glaeser, R. M. Retrospective on the early development of cryoelectron microscopy of macromolecules and a prospective on opportunities for the future. *Journal of structural biology* **163**(3):214–223 (2008).

Temme, C., Zhang, L., Kremmer, E., Ihling, C., Chartier, A., Sinz, A., Simonelig, M., & Wahle, E. Subunits of the Drosophila CCR4-NOT complex and their roles in mRNA deadenylation. *Rna* **16**(7):1356–1370 (2010).

Tharun, S., He, W., Mayes, A. E., Lennertz, P., Beggs, J. D., & Parker, R. Yeast Sm-like proteins function in mRNA decapping and decay. *Nature* **404**(6777):515–518 (2000).

Tritschler, F., Braun, J. E., Eulalio, A., Truffault, V., Izaurralde, E., & Weichenrieder, O. Structural basis for the mutually exclusive anchoring of P body components EDC3 and Tral to the DEAD box protein DDX6/Me31B. *Molecular cell* **33**(5):661–668 (2009).

Tucker, M., Valencia-Sanchez, M. A., Staples, R. R., Chen, J., Denis, C. L., & Parker, R. The transcription factor associated Ccr4 and Caf1 proteins are components of the major cytoplasmic mRNA deadenylase in Saccharomyces cerevisiae. *Cell* **104**(3):377–386 (2001).

Uchida, N., Hoshino, S.-i., & Katada, T. Identification of a human cytoplasmic poly (A) nuclease complex stimulated by poly (A)-binding protein. *Journal of Biological Chemistry* **279**(2):1383–1391 (2004).

Ukleja, M., Cuellar, J., Siwaszek, A., Kasprzak, J. M., Czarnocki-Cieciura, M., Bujnicki, J. M., Dziembowski, A., & Valpuesta, J. M. The architecture of the Schizosaccharomyces pombe CCR4-NOT complex. *Nature communications* **7**(1):1–11 (2016).

Wahle, E. A novel poly (A)-binding protein acts as a specificity factor in the second phase of messenger RNA polyadenylation. *Cell* **66**(4):759–768 (1991).

Wahle, E. & Rüegsegger, U. 3-End processing of pre-mRNA in eukaryotes. *FEMS microbiology reviews* **23**(3):277–295 (1999).

Wang, H., Morita, M., Yang, X., Suzuki, T., Yang, W., Wang, J., Ito, K., Wang, Q., Zhao, C., Bartlam, M. *et al.* Crystal structure of the human CNOT6L nuclease domain reveals strict poly (A) substrate specificity. *The EMBO journal* **29**(15):2566–2576 (2010).

Webster, M. W., Chen, Y.-H., Stowell, J. A., Alhusaini, N., Sweet, T., Graveley, B. R., Coller, J., & Passmore, L. A. mRNA deadenylation is coupled to translation rates by the differential activities of Ccr4-Not nucleases. *Molecular cell* **70**(6):1089–1100 (2018).

Webster, M. W., Stowell, J. A., & Passmore, L. A. RNA-binding proteins distinguish between similar sequence motifs to promote targeted deadenylation by Ccr4-Not. *elife* **8**:e40670 (2019).

Webster, M. W., Stowell, J. A., Tang, T. T., & Passmore, L. A. Analysis of mRNA deadenylation by multi-protein complexes. *Methods* **126**:95–104 (2017).

Weill, L., Belloc, E., Bava, F.-A., & Méndez, R. Translational control by changes in poly (A) tail length: recycling mRNAs. *Nature structural & molecular biology* **19**(6):577–585 (2012).

Weissmann, F. & Peters, J.-M. Expressing multi-subunit complexes using biGBac. In *Protein Complex Assembly*, pages 329–343 (Springer, 2018).

Weissmann, F., Petzold, G., VanderLinden, R., Brown, N. G., Lampert, F., Westermann, S., Stark, H., Schulman, B. A., Peters, J.-M. *et al.* biGBac enables rapid gene assembly for the expression of large multisubunit protein complexes. *Proceedings of the National Academy of Sciences* **113**(19):E2564–E2569 (2016).

Winkler, G. S. The mammalian anti-proliferative BTG/Tob protein family. *Journal of cellular physiology* **222**(1):66–72 (2010).

Wolin, S. L. & Maquat, L. E. Cellular RNA surveillance in health and disease. *Science* **366**(6467):822–827 (2019).

Wu, Q., Medina, S. G., Kushawah, G., DeVore, M. L., Castellano, L. A., Hand, J. M., Wright, M., & Bazzini, A. A. Translation affects mRNA stability in a codon-dependent manner in human cells. *elife* **8**:e45396 (2019).

Xiang, K. & Bartel, D. P. The molecular basis of coupling between poly (A)-tail length and translational efficiency. *Elife* **10**:e66493 (2021).

Xiang, K., Tong, L., & Manley, J. L. Delineating the structural blueprint of the pre-mRNA 3-end processing machinery. *Molecular and cellular biology* **34**(11):1894–1910 (2014).

Xie, J., Kozlov, G., & Gehring, K. The "tale" of poly (A) binding protein: the MLLE domain and PAM2-containing proteins. *Biochimica et Biophysica Acta (BBA)-Gene Regulatory Mechanisms* **1839**(11):1062–1068 (2014).

Yamashita, A., Chang, T.-C., Yamashita, Y., Zhu, W., Zhong, Z., Chen, C.-Y. A., & Shyu, A.-B. Concerted action of poly (A) nucleases and decapping enzyme in mammalian mRNA turnover. *Nature structural & molecular biology* **12**(12):1054–1063 (2005).

Yi, H., Park, J., Ha, M., Lim, J., Chang, H., & Kim, V. N. PABP cooperates with the CCR4-NOT complex to promote mRNA deadenylation and block precocious decay. *Molecular cell* **70**(6):1081–1088 (2018).

Young, G., Hundt, N., Cole, D., Fineberg, A., Andrecka, J., Tyler, A., Olerinyova, A., Ansari, A., Marklund, E. G., Collier, M. P. *et al.* Quantitative mass imaging of single biological macromolecules. *Science* **360**(6387):423–427 (2018).

Yu, C.-H., Dang, Y., Zhou, Z., Wu, C., Zhao, F., Sachs, M. S., & Liu, Y. Codon usage influences the local rate of translation elongation to regulate co-translational protein folding. *Molecular cell* **59**(5):744–754 (2015).

Zhang, K. Gctf: Real-time CTF determination and correction. *Journal of structural biology* **193**(1):1–12 (2016).

Zhang, X., Virtanen, A., & Kleiman, F. E. To polyadenylate or to deadenylate: that is the question. *Cell cycle* **9**(22):4437–4449 (2010).

Zheng, S. Q., Palovcak, E., Armache, J.-P., Verba, K. A., Cheng, Y., & Agard, D. A. MotionCor2: anisotropic correction of beam-induced motion for improved cryo-electron microscopy. *Nature methods* **14**(4):331–332 (2017).

Zivanov, J., Nakane, T., & Scheres, S. H. Estimation of high-order aberrations and anisotropic magnification from cryo-EM data sets in RELION-3.1. *IUCrJ* **7**(2):253–267 (2020).

Abbreviations

Å	Ångstrom (10^{-10} m)
µg	microgram
µL	microliter
µm	micrometer
µM	micromolar
β-OG	n-octyl-β-D-glucoside
2D	two-dimensional
3C	human rhinovirus protease
3D	three-dimensional
ADH2	glucose-repressible alcohol dehydrogenase
AEBSF	4-(2-aminoethyl)benzenesulfonyl fluoride hydrochloride
AGO	argonaute
APRO	antiproliferative
APS	Ammonium persulfate
ARE	adenosine-uridine rich element
ARE-BP	ARE-binding protein
ARM	Armadillo
AWI	air-water interface
Bam	Bag-of-marbles
BME	β -mercaptoethanol
BS3	bis(sulfosuccinimidyl)suberate
BTG2	B-cell translocation genes
CAA	chloroacetamide
C. elegans	*Caenorhabditis elegans*
Caf1	Ccr4-associated factor 1
CBM	CAF40-binding motif
Ccr4-Not	carbon catabolite repression 4 - negative on TATA-less
CFI	Cleavage factor I

CFII	Cleavage factor II
CHAPSO	3-([3-Cholamidopropyl]dimethylammonio)-2-hydroxy-1-propanesulfonate
CIM	CNOT1-interacting motif
CMC	critical micelle concentration
CN9BD	CNOT9 binding domain
CPSF	Cleavage and polyadenylation specificity factor
cryo-ET	cryo-electron tomography
CstF	Cleavage stimulation factor
CTD	C-terminal domain
CTF	contrast transfer function
CV	column volumes
DCP2	decapping mRNA 2
DCPS	decapping enzyme, scavenger
DNA	deoxy ribonucleic acid
D. melanogaster	*Drosophila melanogaster*
DTT	dithiothreitol
EDC	enhancer of decapping
EDTA	ethylenediaminetetraacetic acid
EEP	exonuclease-endonuclease-phosphatase
EJC	exon junction complex
EM	electron microscopy
EMSA	electrophoretic mobility shift assay
eRF3	eukaryotic release factor 3
E.coli	*Escherichia coli*
EtOH	ethanol
exon	extragenic region
FDR	false discovery rate
FLAM-seq	full-length poly(A) and mRNA sequencing
GA	Glutaraldehyde
GEC	gene expression cassette
GGNBP2	gametogenetin binding protein 2
GIF	post-column energy filter
GraFix	gradient fixation
GST	Glutathione-S-Transferase
h	hour(s)
HCl	hydrochloric acid
HEAT	Huntingtin, elongation factor 3, protein phosphatase 2A, yeast kinase TOR1

Hi5	HighFive
IMAC	immobilized metal affinity chromatography
ISG	interferon stimulated genes
KCl	Potassium chloride
keV	kilo electron volt
KH	K homology
KOAc	potassium acetate
LB-medium	Lysogenic broth medium
LIC	ligation-independent cloning
LMNG	Lauryl Maltose Neopentyl Glycol
LRR	Leucin rich repeats
m^7G	7-methylguanylate
MBP	Maltose-binding protein
$MgCl_2$	Magnesium dichloride
$MgSO_4$	Magnesium sulfate
MIF4G	middle domain of eukaryotic initiation factor G
min	minute(s)
miRISC	miRNA-induced silencing complex
miRNA	microRNA
mL	milli litre
MLLE domain	mademoiselle domain
MOPS	3-Morpholinopropanesulfonic acid
MP	mass photometry
MRE	miRNA response elements
mRNA	messenger RNA
MS	mass spectrometry
MTR4	mRNA transport regulator
MW	molecular weight
NaCl	Sodium chloride
NaOH	sodium hydroxide
NEB	New england biolabs
NGD	No-go decay
NMD	nonsense-mediated decay
NP-40	nonyl phenoxypolyethoxylethanol
NSD	non-stop decay
nt	nucleotide
O/N	overnight

P-bodies	processing bodies
PABPC	cytoplasmic poly(A) binding protein
PABPN	nuclear poly(A) binding protein
Paip2	PABP-interacting protein 2
PAL-seq	poly(A) tail length profiling by sequencing
PAM2	PABP-interacting motif 2
PAN	poly(A)-specific nuclease
PAP	poly(A) polymerase
PARN	poly(A)-specific ribonuclease
PAS	poly(A) signal
PBS	Phosphate buffered saline
PCR	polymerase chain reaction
PIC	EDTA-free cOmplete Protease Inhibitor Cocktail
PIWI	P-element induced wimpy testis
polH	polyhedrin promoter
poly(A)	poly adenosine
PRE	Pumilio-response element
pre-mRNA	precursor-mRNA
PTC	premature stop codon
RBP	RNA-binding protein
RNA	ribonucleic acid
RNF219	RING finger protein 219
RNP	ribonucleo protein particle
RRM	RNA-recognition motif
RT	room temperature
s	second(s)
S. cerevisiae	*Saccharomyces cerevisiae*
S. pombe	*Schizosaccharomyces pombe*
SDS-PAGE	sodium dodecyl sulfate polyacrylamide gel electrophoresis
SEC	size-exclusion chromatography
SENP2	SUMO/ Sentrin specific peptidase 2
siRNA	silencing RNA
SLiM	short linear motif
SNR	signal-to-noise ratio
SOC-medium	super optimal broth with catabolite repression - medium
SUMO	Small Ubiquitin-like Modifier
T_m	melting temperature

TB-medium	terrific broth medium
TBE	Tris-borate-EDTA
TCEP	tris(2-carboxyethyl)phosphine
TEMED	Tetramethylethylenediamine
TEV-protease	tobacco etch virus-protease
TFA	trifluoroacetic acid
TNRC6	trinucleotide repeat containing adaptor 6
TPR	tetratricopeptide repeat
TRAMP	TRF-AIR-MTR4
Tris-HCl	tris(hydroxymethyl)aminomethane
Trisborate	TBE
tRNA	transfer RNA
TRP	tryptophan
TRX	thioredoxin
TTP	Tristetraprolin
TUTase	terminal urdidylyl transferase
XL-MS	cross-linking mass spectrometry
XRN1	5'-3' exoribonuclease 1
YTHDF2	YTH domain-containing family protein 2
Z-tag	based on staphylococcus Protein A, binds to Fc fragment of AB

Acknowledgement

First of all, I would like to express my sincere gratitude to my PhD supervisor, Prof. Elena Conti, for allowing me to work on this project. Elena supported me with her expertise, enthusiasm and motivation throughout my PhD project.
Furthermore, I would like to thank my unofficial direct supervisors Dr. Jérôme Basquin and Dr. Ingmar Schäfer for their support, many helpful suggestions, and their patience over the years.
I would also like to thank my TAC members Prof. Karl-Peter Hopfner, Dr. Naoko Mizuno, and Dr. Mike Strauss for their informative and helpful comments and encouragement. Special thanks to the MPIB Biochemistry Core Facility, in particular Dr. Barbara Steigenberger for XL-MS analyses, Dr. Stephan Uebel for initial help with the mass photometer, and Dr. Sabine Suppmann and Judith Scholz for large-scale expression in insect cells and help with the C-tag peptide.
A big thank you goes to the fantastic cryo-EM facility at MPIB, Dr. Daniel Bollschweiler, Dr. Tillmann Schäfer and Dr. Mike Strauss for their constant help and advice with cryo-EM and data collections. A big thank you goes to Dr. Rajan Prabu and Dr. Christian Benda for maintaining the computer environment and for their constant support in working through problems. I would also like to thank all current and former members of the Conti department for their great scientific support and the pleasant laboratory atmosphere. In particular, I would like to thank Fabien Bonneau for constant, valuable input and help with XL-MS data, Petra and Tatjana for their help in cloning difficult constructs, Steffen Schüssler, Marc Baumgärtner and Judith Ebert for their support in protein purifications, Ariane Fischer for expression assays, Elfriede Eppinger, Lisa Stegmann and Marc Baumgärtner for teaching me how to work with insect cells and for maintaining our insect cell facility. Thanks also to Walter Erhardt and Ivan Gandara for general IT technical support and to Uli Goldschmitt and Petra Lee for administrative help. A big thank you to Peter Reichelt, who kept the Aekta systems running perfectly and was always available when something went wrong. He also organized so many, great barbecues and beer tast-

ings. I was also very happy to be part of the graduate program GRK1721. The atmosphere was always very friendly, we had great retreats and great workshop opportunities. A big thank you also goes to all the postdocs and PhD students in the Conti department (2nd and 3rd floors), both past and present, for the nice atmosphere, their input and suggestions during the group meetings and general help in the lab and EM bunker. In particular, I would like to thank Sevim for her input on my project, Iuliia for constant good mood and discussions on insect cell stuff, Basti for his input and cursing in Italian ;), Christian for the many conversations about scientific topics or anything else during every lunch break ;) and Ingmar for constantly listing to me, help with EM-related things and for proofreading my thesis. Next, I would like to thank my fellow PhD students from the Conti lab: Alex, Mahesh, Marcela, Sofia, Achim, Lukas, Felix, Ksenia, Julian, Michi, Brone, Liang and Zhen, as well as the PhD students from the Junior Groups, Nira, Chris, Shun, Steffi, Dirk and Giulia. It was a great atmosphere in the lab but also outside with PhD dinners, get-togethers, Oktoberfest visits, and skiing trips. I would especially like to thank Mahesh for the many ice cream breaks and our insect cell chats ;), Felix for his interest and many ideas for my project, Lukas as fellow GRK1721 student and proud new organizer of the PhD dinners, Alex, Dirk and Achim for rare but fun Skat nights at Café Gans or Schelling Salon, and of course Steffi, Dirk and Giulia for many evenings at Café Gans, Substanz or playing board games. I am so glad that you all will stay in Munich, at least for the next years ;). Outside the lab, I would like to thank my friends (Hanne, Saskia, Kathi, Chrissy, Meike, Tina, Aga, Gundi, Kathrin) for their constant support and nice balance to work. I would especially like to thank my quasi-roommate Kathrin for her friendship and evenings with Aperol on her balcony. A huge thank you goes to my boyfriend Steffen, who has really supported me a lot in every way (especially during the Covid19 pandemic!) over the last three years. I couldn't have made it here without you.
And finally, the biggest thanks goes to my Dad, who always believes in me and without his unconditional support and encouragement, I would not have made it to this point. I would like to dedicate this work to my Mum, who would certainly have been very worried, but would also have been very proud of a completed PhD.